Measurements of the total transverse energy in pp collisions and a new technique for model independent missing transverse energy searches with ATLAS

Peter Alexander Wijeratne
University College London

Submitted to University College London in fulfilment
of the requirements for the award of the
degree of **Doctor of Philosophy**

June 13, 2013

Declaration

I, Peter Alexander Wijeratne, confirm that the work presented in this thesis is my own. Where information has been derived from other sources, I confirm that this has been indicated in the thesis.

Peter Alexander Wijeratne

Abstract

This work studies proton-proton collision data recorded by the ATLAS detector at the LHC from 2010 to 2012. The bulk of the work concerns measurements of the sum of the transverse energy of particles as a function of their pseudorapidity, η, at a centre-of-mass energy $\sqrt{s} = 7$ TeV. These measurements are performed using the entire acceptance of the ATLAS detector, $0 < |\eta| < 4.8$, and are split into two classes of event: one requiring the presence of low transverse momentum particles and the other requiring particles with a significant transverse momentum. In the latter case measurements are made in the region transverse in ϕ to the hard scatter. As such, both measurements are sensitive to non-perturbative QCD processes. Comparisons are made with the predictions from various Monte Carlo event generators, which generally underestimate the quantity of transverse energy at high η. This discrepancy is found to be dependent on the choice of Parton Distribution Function.

A new technique for performing model independent missing transverse energy searches is presented. The ratio of the branching fractions between $Z \rightarrow \nu\bar{\nu}$ and $Z \rightarrow \mu^+\mu^-$ processes is used, with deviation from the Standard Model prediction inferred as an indication of new physics. Preliminary Monte Carlo results are shown by way of proof-of-principle.

In addition, technical measurements of the muon reconstruction efficiency of the ATLAS inner detector trigger algorithms are presented. An established technique is used to obtain unbiased results, and the performance of the algorithms discussed.

Acknowledgements

I'd like to thank my supervisor Emily Nurse, who has patiently provided the help and guidance necessary to lead me through the weird world of experimental particle physics. During my year and a half attachment at CERN I also worked closely with Robindra Prabhu on the transverse energy flow measurement, which would never have reached its final state if not for their tireless efforts. I'm indebted to Robindra, with whom I worked in person, for all his hard work and for generally being an awesome dude.

Throughout my three year attachment to the inner detector trigger group, endless good-natured support and advice was given by its convenor, Jiri Masik. I'd also like to thank Mark Sutton, who provided useful and frequently enlightening feedback. I'm also grateful to Alessandro Cerri, former head of the ATLAS online trigger operations, for his support and for having the faith to put me on the other end of the on-call phone. Though I don't doubt he lost some sleep over it.

In a collective sense I thank everybody who made and makes the LHC what it is. I was a bairn when it was on the drawing board, so I count myself privileged to have been part of something that has had so much life put into it.

I thank my Mum and brother for loving and supporting me, and for making our family the warm place that it is. Laurence, I trust you approve of the second chapter quote. Dad, while he was with us, gave me so much — you stay with me every day. And I never forget your mantra from my early years: "think about it logically". It's a pity I can't apply that to everything in life, eh? Thanks also to all my friends, who make up so much of my life.

Finally, I thank Sara, who has loved and supported me throughout all of this and everything else. You make me happy every single day.

For Dad

Contents

List of Figures

List of Tables

Chapter 1

Introduction

"In the dreaming man's dream, the dreamed man awoke."
— Jorges Luis Borges

Theories last as long as experimental evidence allows them to. In this respect, the Standard Model of particle physics has emerged as one of the most enduring theories in modern science. Inspired by developments in quantum mechanics, it has motivated the technological advances necessary to study Nature at its most fundamental scale.

The rise of the Standard Model has been accompanied by a flowering international community. As its scope has increased over the past half-century from explaining quantised electromagnetic interactions to the origin of matter itself, the number of people involved in its development has burgeoned. This has culminated in the ATLAS (A Toroidal Lhc ApparatuS) experiment, based at the Large Hadron Collider (LHC) at the European Organisation for Nuclear Research (CERN). With over 3000 physicists from 38 different countries, it represents the largest ever collaboration of scientific researchers. The LHC itself, which is designed to accelerate and collide hadronic particles at energies equivalent to those ten trillion-trillionths of a second after the Big Bang, is an unprecedented feat of engineering.

The primary aim of the ATLAS experiment, and this work, is to test the Standard Model's description of physics at these energies. This work is divided into five parts: the first two provide the theoretical (Chapter 2) and practical (Chapter 3) background relevant for the remaining three sections, which detail measurements of Standard Model physics (Chapter 4), a new technique for measuring physics processes not described by the Standard Model (Chapter 5), and a measurement of how efficiently the ATLAS detector reconstructs particles from Standard Model processes (Chapter 6).

In Chapter 2, the origins and scope of the Standard Model are discussed. The components most relevant to this work are examined in detail and techniques for measuring them are presented. In addition, one of the outstanding unsolved issues in the Standard Model is considered, and a popular theory for its resolution is described.

The design and operation of the LHC and the ATLAS detector is discussed in Chapter 3. Key features of the ATLAS detector pertinent to the following measurements are highlighted, and a detailed description of the reconstruction software analysed in Chapter 6 is given.

The world's first fully inclusive measurement of the sum of the transverse energy in pp collisions, for two types of Standard Model physics processes, is presented in Chapter 4. The motivation is discussed and the analysis process detailed. The final results are compared with a number of different physics models, and an assessment of their descriptions is given.

A new technique for making measurements of processes beyond the Standard Model is presented in Chapter 5. The advantages of the method over current methods are given, and the theoretical justification provided. Preliminary results are shown, and a discussion of the necessary steps to complete the analysis is given.

Chapter 6 describes the first unbiased measurement of the ATLAS inner detector's tracking software reconstruction efficiency. The technique used to perform the measurement is presented, and the analysis process detailed. Comparisons are made between different software implementations and conclusions drawn as to the performance at large.

Finally, Chapter 7 summarises the conclusions from the preceding studies and discusses their relevance to the development of the Standard Model.

Chapter 2

Theory

"The sum of the square roots of any two sides of an isosceles triangle is equal to the square root of the remaining side!"
— Homer Simpson

2.1 The Standard Model

At its heart, the Standard Model of particle physics is a theory of interacting fields. Its origins lie in the successful fusion of electromagnetism, quantum mechanics and special relativity, elegantly expressed by the Dirac equation. Upon quantising the resulting gauge theory — in effect, allowing it to be measured — a new basis for understanding elementary particles and their interactions was born, called quantum field theory (QFT). This basis was used to create the theory of quantum electrodynamics (QED), which defines the electromagnetic interaction between photons and charged particles, and which has since become the best tested theory in the history of science[1].

A guiding component in the development of the Standard Model is the principal of symmetries. The root of this idea is Noether's theorem, which states that if the action of a physical system has a continuous symmetry, then a physical property is conserved. Therefore in QFT, the Lagrangian describing a given system's dynamics

---

[1] The gyromagnetic ratio of the electron has been measured to agree with theory to within ten parts in a billion.

is constructed such that it is invariant under some symmetry transformation groups. To provide a description of sub-atomic particles, their interactions, and observed conservation laws the Standard Model is constrained in terms of such groups. It can be roughly separated into two non-Abelian[2] gauge theories: the $SU(2)\times U(1)$ gauge theory describing electromagnetic and weak interactions, and the $SU(3)$ gauge theory describing the strong interaction. These descriptions are constrained by a number of free parameters — for example, the fermion masses, mixing angles, complex phases, and coupling constants — which are determined by experiment. It is a testament to the strength of the theory that accurate measurements of these parameters over the past few decades have not lessened its descriptive power; for example, the Standard Model predicted the existence of the top quark, found at the Tevatron at Fermilab [1], and recent measurements of its mass [2–4] are in agreement with Standard Model predictions.

Combining these theories produces the $SU(3)\times SU(2)\times U(1)$ Standard Model (SM) of particle physics, which encapsulates a complete description of three of the four fundamental forces[3] . Its Lagrangian conserves properties such as the classical electric charge, and also quantum numbers such as isospin. It is the aim of this work to experimentally test various components of the SM, and to help improve its description of physics not derivable from first principles.

2.2 Particles

There are two types of particles in Nature, defined by whether they have half-integer or integer spins: fermions and bosons, respectively. A direct consequence of the observed conservation of charge, parity and time as a combined quantity (CPT) is that every particle must have an anti-particle, with the same spin state but opposite charge and helicity. Furthermore, CPT conservation dictates that these particles have the same mass and lifetime as their counterparts. Hence we have the basis of a

---

[2] Unlike $U(1)$ (a 1-dimensional, Abelian gauge theory with simple phase transformations), $SU(N)$ theories depend on several $(N^2 - 1)$ variables and do not necessarily commute, meaning that the result of two consecutive transformations may depend on the order in which they are applied.

[3] Along with the separate theory of general relativity, which describes the gravitational force, the SM bestows a simple, beautiful law: that all observed interactions in Nature are a product of local symmetries.

family of fermions (Tables 2.1 and 2.2 for quarks and leptons, respectively), whose existence has been verified or inferred by experiment.

Governing the interactions of these particles are the vector bosons (Table 2.3), which arise from their respective gauge theories: photons (QED), W and Z bosons (electroweak) and gluons (strong). The gravitational force is not constrained by the Standard Model, and its unification with the other three forces remains an outstanding issue in modern physics.

Quark	Symbol	EM charge (e)	Spin ($h/2\pi$)	Mass (GeV)
up	u	2/3	1/2	0.003
down	d	-1/3	1/2	0.006
strange	s	-1/3	1/2	0.1
charm	c	2/3	1/2	1.3
bottom	b	-1/3	1/2	4.2
top	t	2/3	1/2	173

Table 2.1: The Standard Model quark family, paired by generation.

Lepton	Symbol	EM charge (e)	Spin ($h/2\pi$)	Mass (GeV)
electron	e	-1	1/2	0.0005
electron neutrino	ν_e	0	1/2	$< 2 \times 10^{-9}$
muon	μ	-1	1/2	0.1
muon neutrino	ν_μ	0	1/2	$< 2 \times 10^{-9}$
tau	τ	-1	1/2	1.8
tau neutrino	ν_τ	0	1/2	$< 2 \times 10^{-9}$

Table 2.2: The Standard Model lepton family, paired by generation.

2.3 Quantum Chromodynamics

The theory of Quantum Chromodynamics (QCD) provides the basis for our understanding of the strong interaction, one of the four fundamental forces in Nature. It is

Boson	Symbol	EM charge (e)	Spin ($h/2\pi$)	Mass (GeV)
gluon	g	0	1	0
photon	γ	0	1	0
W	$W^{\pm}$	± 1	1	80.399 ± 0.025
Z	Z^0	0	1	91.1876 ± 0.0021

Table 2.3: The Standard Model force carriers.

this interaction, mediated by gluons, that binds quarks together to form the family of particles called hadrons, of which the most common example is the proton.

Mathematically it is expressed as a non-Abelian gauge theory, with a corresponding gauge-invariant Lagrangian given by:

$$\mathcal{L}_{QCD} = -\frac{1}{4} F_a^{\mu\nu} F_{\mu\nu a} + \sum_{f=1}^{n_f} \bar{q}_f (i\gamma^\mu D_\mu - m_f) q_f \tag{2.1}$$

where the covariant derivative is defined by

$$D_\mu q_f = \delta_\mu q_f + i g_s A_{\mu a} \frac{1}{2} \lambda_a q_f \tag{2.2}$$

In Equation (2.1), $F_a^{\mu\nu}$ and $F_{\mu\nu a}$ represent the gauge invariant gluon field strength tensors in the adjoint representation of $SU(3)$, and q_f describes the quark field in the fundamental representation of $SU(3)$. The sum over f is for the different quark flavours: up, down, charm, strange, top and bottom, each with different masses, m_f. The γ^μ matrices provide the link between the spinor and vector representations of the Lorentz group, and the covariant derivative ensures that the Lagrangian itself is invariant. Equation (2.2) expands on the covariant derivative itself: δ_μ is a standard Dirac delta function; g_s is essentially the strong coupling constant, α_s ($\alpha_s = g_s^2/4\pi$); $A_{\mu a}$ are the spin-1 gluon fields; and λ_a are the hermitian, traceless Gelman matrices.

Examining (for example) the field strength tensor $F_a^{\mu\nu}$ explicitly:

$$F_a^{\mu\nu} = [\partial^\mu A_a^\nu - \partial^\nu A_a^\mu - g f_{abc} A_b^\mu A_c^\nu] \tag{2.3}$$

Here the indices a, b, c run over the eight colour degrees of freedom of the gluon field, and f_{abc} are the structure constants of $SU(3)$. Notably, it is the non-Abelian third term which allows for triplet and quartic gluon self-interactions, which ultimately lead to asymptotic freedom (discussed in more detail in Section 2.3.2).

The $SU(3)$ gauge theory itself describes the physics of quarks interacting via the exchange of massless gluons, and contains two types of symmetry: colour, which is a local gauge symmetry, and flavour, which is global[4]. As such quarks carry a colour charge, r, b, g (anti-quarks $\bar{r}, \bar{b}, \bar{g}$) and their interactions are invariant under transformations in colour space.

While QCD shares similarities with QED, which also describes the interaction of fermions with massless vector bosons (photons), it features two important differences: gluons' colour charge means they can self-interact, whilst photons are charge-neutral and hence can not; and quarks and gluons are never observed as free particles, but instead combine to form colour-neutral hadrons. These features give rise to two idiosyncrasies in QCD: colour confinement and asymptotic freedom.

2.3.1 Colour confinement

An interesting property of the interaction between quarks and gluons is that its strength does not diminish as the distance between them increases. Though not explicitly predicted by QCD, it can be explained in terms of gluon self-interactions and the fact that the interaction strength depends on the number of quarks.

When energy is supplied to a $q\bar{q}$ system, causing the quarks to separate, virtual gluons can interact along the "tube" connecting them, effectively flattening it as the distance increases. Since the area of this tube will stay roughly constant, and the number of field lines exactly constant, the energy of the system increases with

---

[4] The SM considers two types of symmetries: local and global. Loosely speaking a local symmetry is dependent on spacetime, whereas a global symmetry is not. Therefore global symmetries can be thought of as a subset of fixed-parameter local symmetries; in effect, they are a bi-product of local symmetries.

separation. An analogy to this is the stretching of an elastic band; when the QCD tube snaps, however, another $q\overline{q}$ pair is formed and the original pair return to a ground state.

2.3.2 Asymptotic freedom

Another peculiar feature of QCD is the so-called "running" of its coupling strength $\alpha_S(\mu^2)$ with the energy scale μ^2 of the process; specifically, it decreases as μ^2 increases:

$$\alpha_S(\mu^2) \approx \frac{4\pi}{(11 - \frac{2}{3}N_f)ln(\mu^2/\lambda^2_{QCD})} \tag{2.4}$$

Here N_f is the number of quarks, λ_{QCD} represents the energy limit of QCD as a theory, and the term in 4π is a bi-product of the integration over all space.

The running of the coupling constant is due to gluons carrying colour charge. Like the EM field in QED, the gluon field strength can be decreased, or "screened", by virtual particle-anti-particle pairs (in QED e^+e^-, in QCD $q\overline{q}$) which cause the vacuum to become polarised. However the fact that gluons are themselves also charged results in a competing opposite effect that enhances the field at long distances. Hence at low energies (long distances) the strong force is strong, while at high energies this latter effect is negligible, and the gluon field strength decreases.

As a consequence of Equation (2.4), $\alpha_S(\mu^2)$ is very large if $\mu^2 \approx \lambda^2_{QCD}$; at a value of approximately[5] $\lambda^2_{QCD} \approx 0.3$ GeV. This presents a problem in terms of quantum mechanical calculations, which rely on perturbation theory to describe real quantum systems. The main idea of perturbation theory is to start with the simplest known system and add a perturbing Hamiltonian to represent a weak disturbance, allowing for the calculation of more complex states. This is a standard technique, necessary because it is very difficult to find exact solutions for even moderately complex quantum systems. Though perturbation theory does not provide exact solutions, for small values of the expansion parameter, say, α, they can lead to results

---

[5] Throughout this work, the convention $\hbar = c = 1$ is adopted.

well reproduced by experiment. With respect to QCD, this expansion parameter is equivalent to α_S.

As such, "soft" processes of the order $\lambda^2_{QCD} \approx 0.3$ GeV can not be calculated from first principles. Theoretically, the most well established approach is lattice QCD, which uses a discrete number of space-time points to restrict the analytically unsolvable path integrals to a series of involved numerical calculations. Experimentally the primary handle is obtained via parton distribution functions (PDFs), which are extracted from measurements of non-perturbative states. These PDFs define the probability of finding a parton of longitudinal momentum fraction x at momentum transfer Q^2; in essence, they govern the number of interactions and the spread of particle energies per collision. Further discussion of the types of processes described by PDFs is given in Section 2.4.2.

In the energy regime $\mu^2 \gg \lambda^2_{QCD}$ the coupling strength becomes essentially negligible, and perturbation theory can be used. The highest energy transfer between two partons in a hadronic interaction is termed the "hard scatter", which defines the top-level, or "hard", process. Precise calculations using perturbative QCD are usually only performed to three orders[6]: leading (LO), next-to-leading (NLO) and next-to-next-to-leading (NNLO) orders. All orders above LO are treated by renormalisation, which is discussed in the following section.

2.3.3 Infrared and ultraviolet divergences

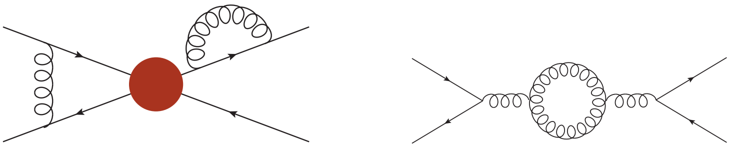

(a) Left of the interaction vertex: soft Coulomb gluon exchange. To the right: a hard collinear gluon.

(b) A simple gluon loop.

Figure 2.1: Feynman diagrams displaying (a) IR and (b) UV divergences, respectively.

There are two types of divergences possible in the QCD (and indeed QED) cross-section: infrared (IR) and ultraviolet (UV). IR divergences are possible because

---

[6] The number of vertices in a given process' Feynman diagram dictates its order.

gluons have zero mass and are essentially impossible to resolve at low energies. They come in two types: soft and collinear exchange (see Figure 2.1a). As shown in Figure 2.1a, soft exchange (mediated by what are termed “Coulomb” gluons) occurs between the incoming quarks. The term collinear is used due to the emitted gluons having transverse momentum $k_T \rightarrow 0$; as such, they propagate parallel to the parton. Both types are usually controlled by dimensional regulation, which reduces the range of the loop integral by some factor then takes the limit as this factor tends to infinity.

UV divergences arise from virtual corrections due to loop diagrams (see Figure 2.1b). They are partly controlled by applying a non-physical cut-off λ_0, above which QCD can no longer make predictions. A renormalisation scale μ_R is also introduced, chosen to be similar to the scale of observed physics. These terms are convoluted, allowing for the UV divergences to be subtracted into bare parameters, leaving finite predictions. This process is know as renormalisation, and is necessary for any field theory containing propagators that can form virtual loops to be practicable.

2.3.4 Factorisation in QCD

The strong force renders a smooth calculation of the cross-section from zero to infinite energies impossible. Theoretically the process of $q\overline{q}$ splitting described in Section 2.3.1 can continue until no further energy is delivered to the system and all $q\overline{q}$ pairs are in their ground state. This adds a serious complication to the calculation of strong processes from first principles, since IR divergences appear as a given gluon's momentum tends to zero.

Therefore, in order for QCD to be a theory that can make predictions, it is necessary for the two regimes defined in Section 2.3.2 to be determined separately. This technique is called factorisation, and was first successfully applied to Deep Inelastic Scattering (DIS) processes[7]. It is worth noting that factorisation only works exactly for processes with 0 or 1 incoming quarks or gluons; for hadron collider experiments it is applied more approximately, mainly due to contributions from multiple parton interactions.

---

[7] DIS typically involves the interaction of a photon or lepton with a hadron, allowing the hadron's structure to be studied.

In terms of the hadron's structure function, $F(x)$, factorisation is expressed as:

$$F(x) = \sum_f \int_x^1 (d\xi/\xi) \overbrace{H_f(x/\xi)}^{Hard\ scatter} \overbrace{\phi_{f/N}(\xi)}^{PDFs} \tag{2.5}$$

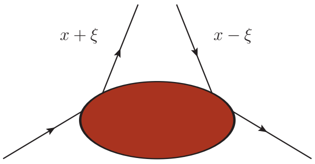

Figure 2.2: Basic outline of DIS, where an incoming quark interacts with an incoming particle, transferring momentum ξ.

Here the sum is over all partons, f, in the interacting hadron N, and x and ξ are the longitudinal momentum fractions carried by the interacting parton (see Figure 2.2). The important feature of this equation is that a Parton Distribution Function (PDF), $\phi_{f/N}(\xi)$, has been factorised out of the perturbative 'hard kernel', $H_f(x/\xi)$. This is performed in a manner similar to the resummation method discussed in Section 2.3.3 — a 'factorisation scale', μ_F, is chosen and all terms up to this point are absorbed into the PDF. As such there is, once again, an implicit scale dependence; its value is usually set such that the result of a given computation varies little for different values of μ_F. This is often the same as the renormalisation scale, to the effect that $\mu_F^2 = \mu_R^2 = Q^2$.

2.3.5 Hadronisation

As a consequence of colour confinement (Section 2.3.1), the energetic $q\bar{q}$ pairs produced in a hadron-hadron collision will continue to reproduce more pairs until a stable ground state is reached. This process results in the formation of many hadronic final states and is appropriately called hadronisation (Figure 2.3).

Hadronisation is the reason why quarks can not be observed directly[8]; instead, their presence is inferred at the detector level by the collimated shower of hadrons

---

[8] The exception here is the top quark, which decays too quickly to hadronise. However, its short lifetime also ensures it does not reach the detector.

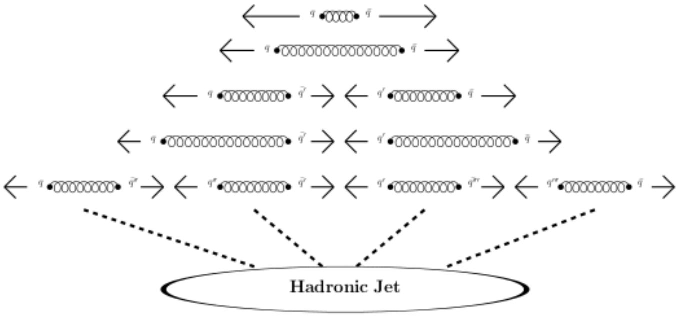

Figure 2.3: An illustration of hadronisation, the process whereby a $q\overline{q}$ splits into subsequent pairs until no more energy is available.

they produce. This shower has an implicit non-perturbative component, and as such matching hadrons to quarks exactly is a tenuous notion. Instead, particle showers are enveloped by what are known as 'jets', which provide the means to measure the parent particle. Jets are one of the main tools in observable QCD, and are discussed — along with others — in the following section.

2.4 QCD in practice

Experimentally there are a number of techniques to measure both perturbative and non-perturbative QCD. Those most pertinent to the analyses presented in this work are discussed here.

2.4.1 Jet algorithms

As outlined in Section 2.3.5, jets form the bridge between a parton and the measured shower of hadrons it begat (see Figure 2.4). In practice they are constructed by jet algorithms, which utilise information provided by the detector — such as the energy deposited in a given part of the calorimeter — to reduce the mess of hadronic activity to a single object. Since the main aim is to compare theory with experiment, the same jet algorithm must be applicable at the parton, hadron and detector level. As such there are certain common requirements that a jet algorithm must meet; for consistency, they are discussed at the parton level.

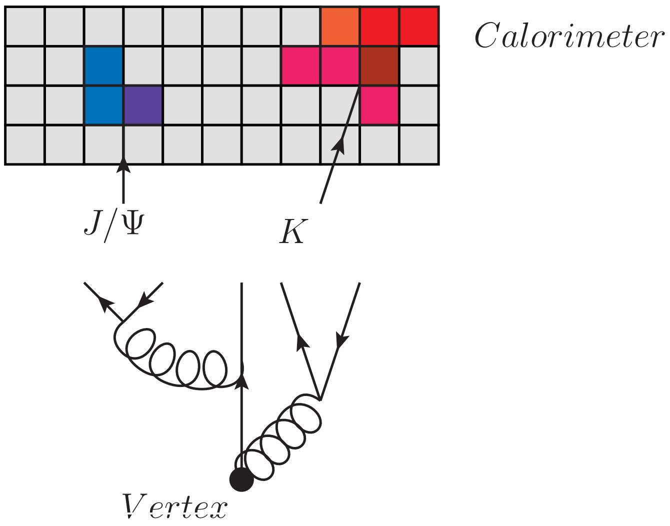

Figure 2.4: An illustration of hadronic jet detection: from the interaction point, quarks and gluons hadronise, producing particles that leave energy deposits in the calorimeter cells.

Practically speaking, a jet algorithm needs to decide which particles to include in a given jet, and how to combine them. The combination is normally performed by summing the 4-momenta of the jet's constituents, yielding the jet 4-momentum. Crucially, in terms of theory-experiment comparison, this quantity is invariant under longitudinal boosts.

The question of which particles to include in the jet is more involved. The simplest approach is to construct a cone of radius R around a particle, such that its axis maximises the energy contained by the cone, and include all other particles within its radius. Though conceptually clear, this approach renders the result dependent on the choice of seed particle; for example, if two cones overlap, a particle may be assigned to the wrong parent. Furthermore, this dependency causes most cone algorithms[9] to handle emissions with vanishingly small momenta incorrectly, leading to incomplete cancellations of real and virtual contributions and hence IR divergences. These flaws can cause significant discrepancies between theory and experiment.

An alternative tactic is to use a cluster algorithm which, as its name suggests, collects particles into clusters. The exact mechanics of the procedure vary between algorithms, with the basic idea being to take two particles and combine them into

---

[9] The exception here is the SISCone algorithm [5], which treats IR divergences correctly. However, the same is not true for collinear radiation.

a single jet, provided they satisfy certain conditions. In the case of the anti-k_T algorithm [6], particles are combined by minimising the distance, d_{ij} between them:

$$d_{ij} = k_T^{2p} \frac{\Delta_{ij}^2}{R^2} \tag{2.6}$$

And the condition for two particles combining to form a single jet is:

$$k_T^{2p} = 2min(E_i^2, E_j^2)(1 - cos\theta_{ij}) < y_{cut}s \tag{2.7}$$

Here, in Equation (2.6), $\Delta_{ij}^2 = (y_i - y_j)^2 + (\phi_i - \phi_j)^2$, where $y_i = \frac{1}{2} ln \frac{E_i + p_{i,z}}{E_i - p_{i,z}}$ is termed the rapidity and p_i and ϕ_i are the momentum and azimuth of particle i, respectively; and R is the radius of the jet, which is analogous to the cone algorithm radius parameter. In Equation (2.7), E_i and θ_i are the energy and polar angle of particle i; y_{cut} is the chosen cut-off, and s is the usual centre-of-mass energy squared. Hence if either $E_i \to 0$ (soft) or $\theta_{12} \to 0$ (collinear), $k_T \to 0$ and the particles are merged. The procedure begins with the hardest particle and iterates until no particle or cluster of particles satisfies Equation (2.7), producing distinct, collimated jets. Furthermore, this technique ensures that a finite measurement is obtainable by requiring that both soft and collinear emissions are treated in the same manner as virtual contributions.

2.4.2 PDFs

Another aim of observational QCD is to provide input data for PDFs. These data constrain certain model decisions used to build the PDF — for example, the relative fraction of gluons at a given longitudinal momentum will dictate the number of particles produced in a given phase space, which can be tested against multiplicity measurements in data. This is conducted for various initial conditions, such as hadronic type and centre-of-mass energy. As such, differences between PDF sets are largely due to the data used in tuning. This work focuses on two such sets: the MSTW [7] and CTEQ [8] parametrisations.

2.4.3 The underlying event

Due to their composite nature, when two hadrons collide it is possible that additional parton-parton interactions accompany the hard scatter. Such processes are termed multiple parton interactions (MPI), first observed in high p_T events[10] from hadron collisions at the ISR at CERN [9]. The probability of MPI occurring scales with centre-of-mass energy; it is therefore a sizeable effect at modern hadron-hadron colliders.

Further interactions are possible due to colour reconnection — a term used for strong interactions between parton systems of different origin — and beam-beam remnants. Collectively all these effects are labelled as the underlying event (UE), which essentially includes every final state particle apart from the hard scatter.

2.4.4 Diffraction

Strictly speaking there are two classes of events if a collision occurs: elastic and inelastic. The former comprises $\sim 25\%$ of the interaction cross-section, and consists of identical initial and final states with no new particles produced, making them largely uninteresting.

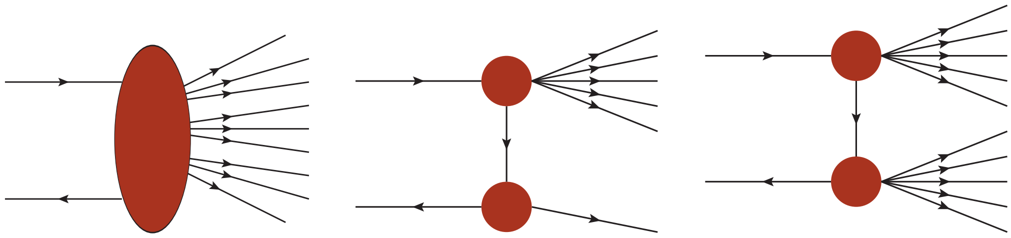

(a) Non-diffractive **(b)** Single-diffractive **(c)** Double-diffractive

Figure 2.5: Diagrammatic examples of (a) non- (b) single- and (c) double-diffractive processes, respectively.

The inelastic cross section can be further subdivided into three[11] categories of events, depending on the degree of hadron dissociation: non-, single- and double-

---

[10] In particle (and nuclear) physics, an "event" is a blanket term for an interaction.

[11] Technically a fourth category exists, termed central diffraction. However its contribution to the cross-section is very small ($< 1\%$) and is more relevant to studies featuring very large rapidity gaps, such as in reference [10].

diffractive (Figure 2.5). The different processes are a result of the varying probabilities with which the two protons interact — in the non-diffractive case, the hadrons collide “head-on”, resulting in their complete dissociation. In diffractive events, the hadrons do not collide directly but instead interact as they cross via colour-singlet exchange. In the single-diffractive case, this causes one of the hadrons to dissociate while the other remains complete. In the double-diffractive case, both hadrons dissociate.

Non-diffractive events constitute the bulk of the total interaction cross-section ($\sim 55\%$), with single- ($\sim 12\%$) and double- ($\sim 8\%$) making up the remainder (along with the elastic contribution). Since diffractive events involve colour-singlet exchange, which suppresses additional interactions in the phase space between the hadrons, a typical signature is large gaps in particle production at central rapidity, known as rapidity gaps.

2.5 Electroweak boson production

As the main body of this work is motivated by the study of QCD interactions, only a brief overview of the electroweak processes relevant to later chapters is given.

The electroweak force describing weak interactions, such as nuclear $\beta^{\pm}$ and mesonic decays, is mediated by the W and Z bosons. These bosons couple to *weak charge*, which is analogous to the strong and electromagnetic charges carried by gluons and photons, but which is possessed by all quarks and leptons, including neutrinos. Due to their non-zero masses (Table 2.3) and correspondingly short lifetimes the range of the weak force is much less than the other three fundamental forces.

Typical Feynman diagrams for W and Z production via proton-proton (pp) interactions are given in Figure 2.6.

Here the leptonic decay channels are shown, but equivalent diagrams also exist for $q\bar{q}^{'} \to q\bar{q}^{'}$ processes. In both figures, the anti-quark represents a “sea” quark, which originates from virtual $q\bar{q}$ pairs in the proton structure. In Figure 2.6b the γ^{*} represents contributions from virtual photons.

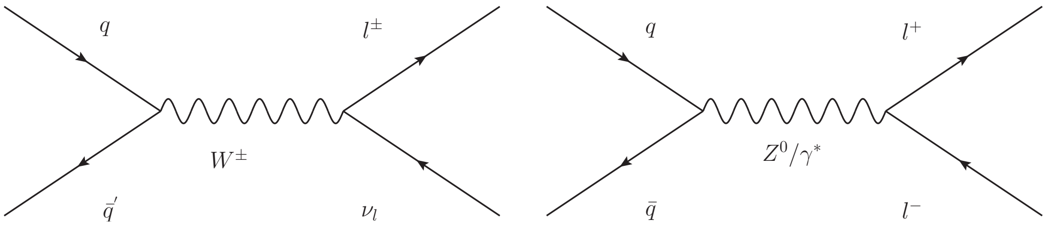

(a) W boson production **(b)** Z boson production

Figure 2.6: Feynman diagrams displaying (a) $W^{\pm}$ and (b) Z^0 production, respectively.

The quantum field theory for electroweak interactions defines the amplitude for these processes as $\mathcal{A} \propto \frac{1}{p_{W,Z}^2 - M_{W,Z}^2}$, where $p_{W,Z}$ and $M_{W,Z}$ are equal to the W and Z boson momentum and mass, respectively. As such at very low energies ($p_{W,Z}^2 \ll M_{W,Z}^2$) the W and Z bosons decay so quickly that their propagation is reduced to extremely short-ranged "pointlike" interactions. At the electroweak energy scale ($\mathcal{O}(100$ GeV$)$), however, the bosons' momentum and mass are of the same order, resulting in the weak force having a strength comparable to the electromagnetic interaction. It is here that their unification becomes appropriate: hence the $SU(2)\times U(1)$ component of the Standard Model.

2.6 Interactions beyond the Standard Model

While the SM provides an excellent description of electroweak and strong interactions, there are several outstanding observations left unexplained. As mentioned previously, one of these concerns gravity, which is observed to be much weaker than the other three fundamental forces, becoming strong only around the Planck scale ($\mathcal{O}(10^{19}$ GeV$)$). Known as the hierarchy problem, several theoretical extensions of the SM — such as supersymmetry (SUSY) — attempt to provide a reason for the massive discrepancy between the Planck and electroweak scales, and to address the issue of possible quantum corrections of the order of the Planck scale to electroweak masses.

In SUSY, the lightest supersymmetric particle is electrically neutral and typically stable. Provided its mass lies within a specific range, these properties also make it an attractive candidate for what is known as "dark" matter. The presence of dark matter can be inferred from the observed discrepancy between the rotation velocity permitted, according to gravitational theory, by the visible (baryonic) matter in large astronomical objects and the actual measured velocity. To ensure that these dark matter particles survived the high densities — and hence high probabilities of mutual annihilation — after the big bang, it is reasoned that dark matter interacts only weakly with itself and visible matter. This is also true of many new particle candidates proposed to extend the SM, and as such the search for these weakly interacting particles is highly motivated.

The primary avenue for performing dark matter searches is via the direct detection of dark matter particles. This requires high precision detectors which, in order to minimise the presence of other particles (such as cosmic ray muons), are often located deep underground. Assuming that dark matter interacts not just with itself but also with SM particles, there are two further possibilities for observation. These searches either involve the decay of a dark matter candidate to a SM particle, observable by astrophysics detectors, or the decay of a SM particle to a dark matter candidate, mediated by the interaction of SM particles in a collider experiment (Figure 2.7).

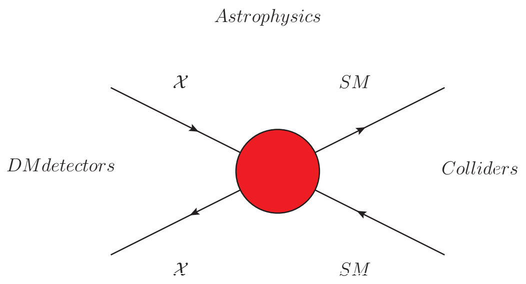

Figure 2.7: Diagrammatic example of the production of dark matter (DM) particles ($\mathcal{X}$) in relation to Standard Model particles (SM). The approach best suited to the detection of each interaction type is indicated: dark matter detectors for direct searches ($\mathcal{X} \to \mathcal{X}$); astrophysics detectors for indirect searches ($\mathcal{X} \to SM$); and SM particle collisions for collider searches ($SM \to \mathcal{X}$).

Since dark matter interacts only minimally with visible baryonic matter, its presence in collider experiments must be inferred from an apparent violation of the conservation of energy — if a dark matter particle is present, the energies of the incoming SM particles will not equal that of its observed decay products. This absent component in the total energy of the final state is known as the *missing energy*, $\not{E}$, calculated via the absolute value of the vector sum over all observed final state particles. In hadron collider experiments, where the energies of the incoming partons are unknown but their initial transverse component is zero, it is instructive to express the missing energy in terms of its longitudinally invariant transverse component, $\not{E}_T$.

2.7 Monte Carlo generators

Monte Carlo generators (MC) provide a computational implementation of theoretical models, allowing them to be tested against real data. In particle physics, an MC is a program designed to calculate the cross-section of a certain physics process in a defined kinematic region. To reflect the probabilistic nature of real particle interactions, the code uses a random number generator to integrate the cross-section randomly over phase space; hence Monte Carlo, a city renowned for its games of chance.

The generated event begins with the primary particle scatter; in the case of pp collisions, parton scattering (see Figure 2.8). Initial and final state gluon radiation — known as bremsstrahlung — is then added, creating parton showers which form colourless hadrons. Their decays are then simulated, and the final step is to mediate all the remaining interactions between decay products. The generator stops computing when all particles have decayed to a stable final state, defined as being those with a proper lifetime greater than 3×10^{-11}s. Particles now exist at the *hadron level*.

To allow for direct comparison with real data, the particles at hadron level are propagated through a detector simulation. The most ubiquitous program used to do this is GEANT4 [11], which provides a model of the ATLAS detector, and accounts for effects such as particle ionisation in the trackers, energy deposition in the calorimeters, intermediate decays and interactions with non-detecting material. Particles now exist at the *detector level*.

There are a variety of MCs available, each defining a certain *model*. Each model provides a differing physical description, utilising, for example, different matrix elements[12], PDFs, hadronisation, description of MPI, parton showering and colour reconnection models. Comparing their outputs with real data is therefore an instructive test of model choices. Furthermore, these data are used to optimise

---

[12] In particle physics, the S-matrix defines the scattering amplitude of two incoming particles into a set of outgoing particles.

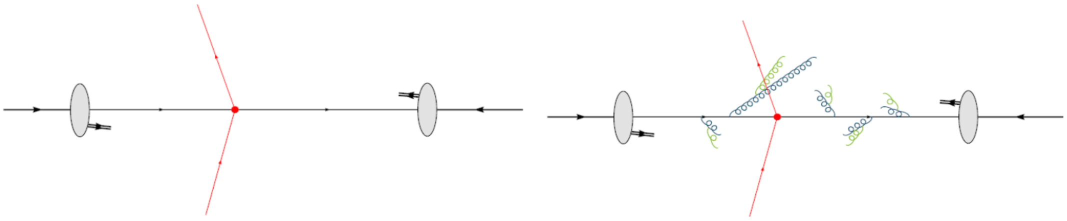

(a) Hard scatter **(b)** ISR and FSR

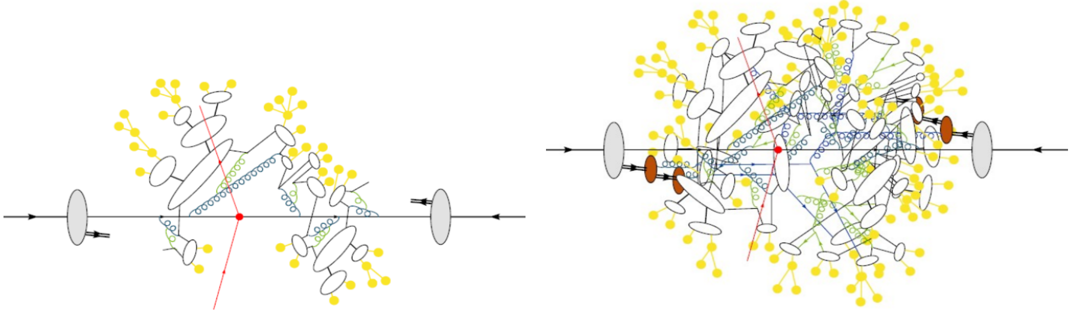

(c) Hadronisation **(d)** Final states

Figure 2.8: The main stages of Monte Carlo simulation: (a) the hard scatter; (b) initial and final state radiation; (c) hadronisation, and the subsequent hadronic decays; and (d) finalise all remaining interactions. Everything but the red lines constitute the underlying event.

an array of model parameters: this process is termed *tuning*, and the resulting description denotes a particular MC's *tune*.

Those MCs pertinent to this work are described in more detail below.

2.7.1 Pythia

The `Pythia 6` [12] and `Pythia 8` [13] brace of MCs are general purpose generators that use the Lund string hadronisation model [14]. `Pythia 8` is the more advanced of the two, utilising a p_T ordered parton shower by default; `Pythia 6` provides this in its more recent versions, but older versions employ a virtuality-ordered parton shower. Both models simulate $2 \rightarrow 2$ non-diffractive processes and MPI according to lowest order perturbative QCD; divergences in the cross-section as $p_T \rightarrow 0$ are regulated by phenomenological models and, when the p_T ordering is utilised, MPI and parton showers are interleaved in a single common sequence of decreasing p_T values. Again, `Pythia 8` features a more complete implementation, with the interleaving performed between initial and final state parton showers and the MPI;

for `Pythia 6`, the final state is not included. In both models diffraction is treated explicitly, with the inelastic cross-section split into the components described in Section 2.4.4 and the diffractive processes governed by pomeron exchange [15], using (by default) the Schuler and Sjostrand [16] parametrisation of the pomeron flux. However, the products of diffractive dissociations are treated differently between generators. `Pythia 6` uses a blanket approach, treating all such dissociations with the Lund string model, resulting in a final state with particles of limited p_T. `Pythia 8` only does this for low mass[13] diffractive systems; in high mass systems, diffractive parton distributions from H1 [17] are used to best simulate diffractive states from hard partonic interactions, with the full canon of MPI and interleaving also being employed. This results in a final state with significantly more high-p_T particles.

2.7.2 Herwig++

Herwig++ (`H++`) is another general purpose generator, built with different components: instead of p_T ordering, it uses an angular-ordered parton shower; and instead of the Lund string model, it uses the cluster hadronisation model [18]. It employs an MPI model similar to the `Pythia` brace, with tunable parameters for regularising the behaviour at very low momentum transfer; it does not, however, include interleaving with the parton showers. Another important difference is that inclusive hadron-hadron collisions are simulated by applying the MPI model to events with no hard scattering, rendering it possible to generate an event with zero $2 \rightarrow 2$ partonic scatters. These events only display activity from beam remnants, and feature large central rapidity gaps; as such, they look similar to double-diffractive dissociation. This is useful because of another prominent difference between `H++` and the `Pythia` brace: it does not contain an explicit model for diffraction.

2.7.3 EPOS

`EPOS` is a different class of event generator, used primarily to simulate heavy ion[14] and cosmic shower interactions. However, it can also simulate proton-proton interactions,

---

[13] Here, mass refers to the invariant mass of the particles produced by the dissociated proton, ranging from light mesons such as the π^0 to systems with hundreds of GeV.

[14] Typically lead ions, though others of similar atomic mass are also considered.

making it an interesting test of the more tailored models mentioned previously. Unlike those models, it utilises an implementation of a parton based Gribov-Regge [19] theory which is an effective, QCD-inspired field theory describing hard and soft scattering simultaneously; as such, cross-sections do not rely on the standard PDFs. A hydrodynamic evolution of the initial state is calculated for the proton-proton scattering process at high parton densities, using the same treatment as for heavy ion interactions. This work considers the `EPOS` LHC tune, which represents a parameterised approximation of the hydrodynamic evolution derived from early LHC data.

2.7.4 ALPGEN

The `ALPGEN` [20] generator is designed for the study of multiparton hard processes in hadronic collisions. Events are generated at the parton level, providing full information on their colour and flavour structure, allowing for the evolution of the partons into fully hadronised final states. Furthermore, these final states can contain up to six partons. This makes it an important tool for predictions in high energy hadronic environments, where final states with several well separated hard jets can occur frequently.

Chapter 3

The ATLAS detector at the LHC

"The effect of a tool-driven revolution is to discover new things that have to be explained."
— Freeman Dyson

The Large Hadron Collider (LHC) at CERN is the world's highest energy hadron collider, with a peak design centre-of-mass energy $\sqrt{s} = 14$ TeV. Housed in a 27 km subterranean ring straddling the French-Swiss border, it supplies particle collisions to the four main particle detectors located in caverns around the ring: namely ATLAS and CMS, which are general purpose detectors; LHCb, which focuses on B-meson physics; and ALICE, which is designed to make measurements of high multiplicity final states. A brief overview of the method by which particles are made to collide within the detectors follows; though it deals specifically with protons, the same general technique is applied to larger nuclear masses.

3.1 The LHC

First, a linear accelerator (Linac II) liberates protons from hydrogen atoms by the application of an electric field. Upon exiting the accelerator the 50 MeV protons enter a booster (Proton Synchrotron Booster), which circulates, accelerates and squeezes protons into bunches, allowing approximately 100 times more protons to enter the next stage than would be possible from Linac II alone. Now at an energy of 1.4 GeV, the proton bunches are directed to a synchrotron (Super Proton Synchrotron), which uses dipole magnets and radio frequency cavities to bend and accelerate them to an energy of 450 GeV. Finally, the proton bunches enter the two adjacent parallel LHC rings in opposite directions, where an electromagnetic field adds energy with each rotation. When the bunches reach the designated energy, focusing quadrupole magnets cause the two beams to cross in the centres of each of the four LHC experiments. The incredibly large electromagnetic fields ($\mathcal{O}(1\ \mathrm{T})$) necessary to bend and accelerate the protons are obtained by super-cooling the magnets with liquid helium to a temperature of approximately 1.9 K, causing them to act as superconductors.

3.2 The ATLAS detector

The ATLAS detector at the LHC [21] is a multipurpose detector constructed to detect and distinguish a broad range of physics signatures (Figure 3.1). Its current incarnation was first proposed in 1994 [22], with the first data from pp collisions at $\sqrt{s} = 900$ GeV collected in November 2009.

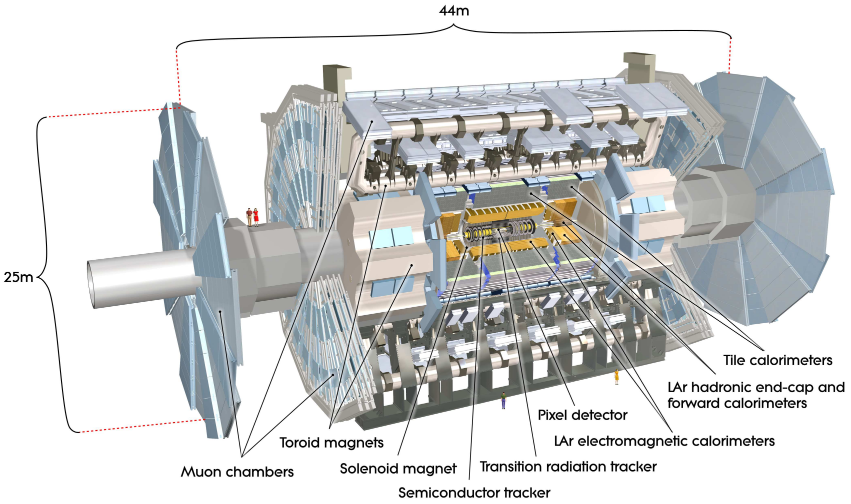

Figure 3.1: A schematic of the ATLAS detector at the LHC. Image taken from [21].

In the right-handed ATLAS Cartesian co-ordinate system, the positive $z-$axis is directed along the beam direction, the positive $y-$axis points perpendicularly upwards from the beam direction, and the positive $x-$axis points to the centre of the LHC ring. The polar angle θ between a particle and the beam axis is measured in the $y - z$ (longitudinal) plane. In this work, θ is expressed in terms of the particle pseudorapidity, η, defined as $\eta = -ln(tan(\theta/2))$. The pseudorapidity can also be expressed as $\eta = \frac{1}{2}ln(\frac{|p| + p_z}{|p| - p_z})$, such that it is approximately equal to the rapidity (Section 2.4.1) in the limit of highly relativistic particles. The azimuthal angle ϕ between a particle of radius r and the $x-$axis is measured in the $x - y$ (azimuthal) plane.

The ATLAS detector is comprised of separate sub-systems, each designed to measure specific types of particle interactions. Working from the interaction point out, it contains:

- the inner detector, covering $|\eta| < 2.5$, which performs high precision measurements of charged particle tracks
- the electromagnetic and hadronic calorimeters, covering $|\eta| < 4.9$, which measure electromagnetic and hadronic energy deposits
- the muon spectrometer, covering $|\eta| < 2.7$, the primary aim of which is to identify high energy muons

Together these systems enable the ATLAS detector to cover almost the whole solid angle around the interaction point; specifically, it is nominally forward-backward symmetric with respect to the interaction point, with complete coverage[1] in the azimuthal plane and a pseudorapidity coverage of $0 < |\eta| < 4.9$ in the longitudinal plane.

3.2.1 Inner detector

The inner detector (ID) covers a pseudorapidity range $0 < |\eta| < 2.5$ and is designed to reconstruct charged particle tracks and interaction vertices. It is immersed in a 2 T solenoidal magnetic field, which causes charged particle trajectories to bend, allowing their momentum to be accurately determined from the curvature of their

---

[1] In practice the coverage is not entirely complete, due to the detector services — such as read-out systems and pipes supplying coolant gas — occupying space in between detector components.

path through the detecting medium. The transverse momentum (p_T) resolutions[2] are shown in Table 3.1.

Detector	Design resolution	η coverage	
		Measurement	Trigger
Tracking	$\frac{\sigma_{p_T}}{p_T} = 0.05\%\ p_T \oplus 1\%$	± 2.5	
EM calorimetry			
Barrel and end-caps	$\frac{\sigma_E}{E} = 10\% \sqrt{E} \oplus 0.7\%$	± 3.2	± 3.2
Forward calorimeter	$\frac{\sigma_E}{E} = 100\% \sqrt{E} \oplus 3.5\%$	$3.1 < \lvert\eta\rvert < 4.9$	$3.1 < \lvert\eta\rvert < 4.9$
Hadronic calorimetry			
Barrel and end-caps	$\frac{\sigma_E}{E} = 50\% \sqrt{E} \oplus 3\%$	± 3.2	± 3.2
Forward calorimeter	$\frac{\sigma_E}{E} = 100\% \sqrt{E} \oplus 10\%$	$3.1 < \lvert\eta\rvert < 4.9$	$3.1 < \lvert\eta\rvert < 4.9$
Muon spectrometer	$\frac{\sigma_{p_T}}{p_T} = 10\%$ at $p_T = 1$ TeV	± 2.7	± 2.4

Table 3.1: Design resolutions of the ATLAS sub-detectors.

The ID is comprised of three main sub-systems; starting from the interaction point and moving out, they are:

- the pixel detector, covering $|\eta| < 2.5$
- the semiconductor tracker (SCT), covering $|\eta| < 2.5$
- the transition radiation tracker (TRT), covering $|\eta| < 2.0$

Each sub-system is further divided into barrel and end-cap components, with the detecting material aligned parallel and perpendicular to the beamline, respectively (Figure 3.2). While the three sub-systems provide almost hermetic coverage in the azimuthal plane, there is a region between the SCT and TRT barrel and end-caps ($1.0 < |\eta| < 1.2$) with a gap between detecting material — this is termed the *crack* region. Particles traversing this region may suffer from reduced spatial resolution due to the lack of tracking information, and may not even reach the end-cap detectors.

The pixel detector is the most finely segmented of the ID sub-systems, containing approximately 80 million readout channels. It is comprised of layers of doped silicon

---

[2] The resolution is a measure of how accurately a detector can resolve its measurement quantity. For example, a finely segmented detector will have a better (smaller) resolution than a more coarse equivalent.

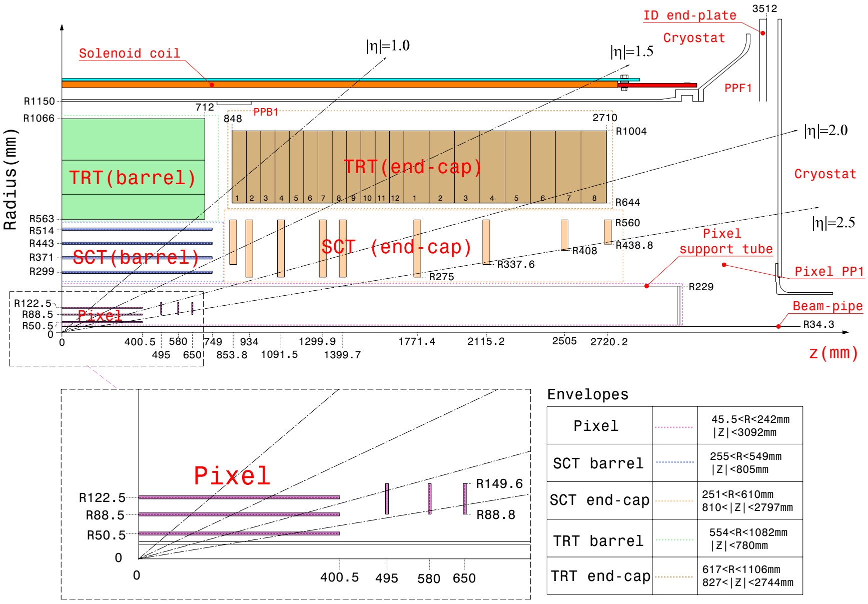

Figure 3.2: Longitudinal schematic of a quarter of the ATLAS inner detector. Image taken from [21].

pixel sensors, segmented in $R-\phi$ and z, with a minimum size in $R-\phi\times z$ of $50\times 400\ \mu m^2$. The accuracy in the barrel is 10 μm ($R-\phi$) and 115 μm (z), and 10 μm ($R-\phi$) and 115 μm (R) in the disks, providing a high granularity position resolution around the interaction point. Typically, a particle will traverse three pixel layers before reaching the SCT.

The SCT is comprised of layers of doped silicon pixel strips arranged in pairs. The accuracy in the barrel is 17 μm ($R-\phi$) and 580 μm (z), and 17 μm ($R-\phi$) and 580 μm (R) in the disks, reflecting the less fine granularity of the SCT compared to the pixel detector. If a particle crosses two strips, a single *space point*, denoting its position in $R-\phi$ and z, is formed. A particle leaving the SCT will have crossed at least eight strips, defining four space points, helping to facilitate accurate track reconstruction.

The TRT is comprised of 4 mm diameter "straw" drift tubes containing a Xe-CO_2-O_2 gas mix. This enhances the ID's ability to identify electrons via measurements of photons from transition radiation. Unlike the two preceding detectors, it only provides $R-\phi$ information, with each straw delivering an intrinsic accuracy of 130 μm. Due to its large surface area, a particle exiting the TRT will typically result in a track with a large number of hits (approximately 36). As such, despite having a worse spatial resolution than the pixel and SCT detectors, when combining their precision with its high statistical information a robust track pattern recognition is achieved.

By design, the active materials in the ID sub-systems respond only to charged particles — doped silicon requires a charge to upset the p-n balance and drift tubes require a charge to ionise the contained gas. As such, the ID is not sensitive to neutral particles.

3.2.2 Minimum bias trigger scintillators

The minimum bias trigger scintillators (MBTS) are mounted in front of the calorimeter end-caps ($|z| = 3560$ mm) on both sides of the interaction point, covering a pseudorapidity range $2.1 < |\eta| < 3.8$. The MBTS feature an eight-fold azimuthal symmetry, and provide a trigger signal as part of its output; when used in low-luminosity LHC operations, this information can be used to enforce very basic requirements on event selection.

3.2.3 Calorimetry

The ATLAS calorimeters (Figure 3.3) cover the entire acceptance ($|\eta| < 4.9$) and are designed to provide complimentary measurements of various particle types and physics signatures. Moving from the interaction point out, the main sub-detectors are:

- the electromagnetic (EM) calorimeter, covering $|\eta| < 3.2$
- the hadronic calorimeter, covering $|\eta| < 3.2$
- the forward calorimeter (FCAL), covering $< 3.1\ |\eta| < 4.9$

Similarly to the ID, the EM and hadronic calorimeters are further divided into barrel and end-cap components; each component's fiducial region and energy measurement resolution are given in Table 3.1. Aside from having a large acceptance and a fine resolution — requirements for any general-purpose detector system — the calorimeters must also occupy a large volume, and feature dense materials. This is necessary to ensure particles interact and deposit energy in the active (detecting) material.

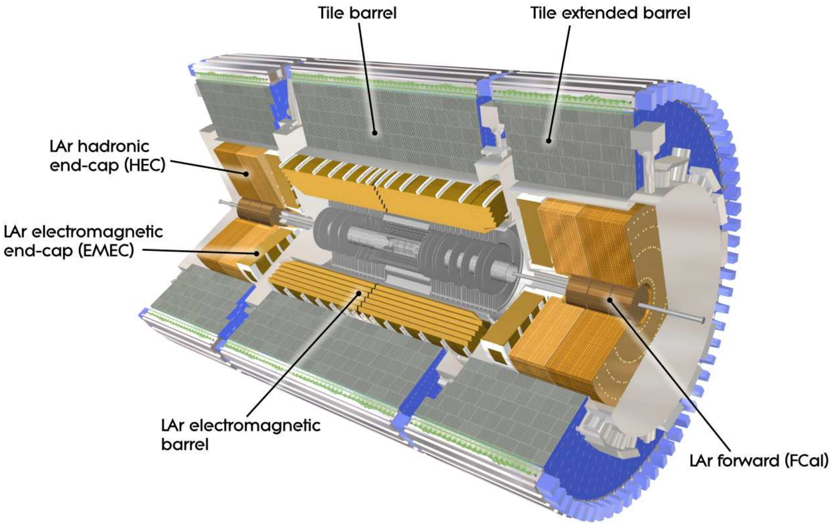

Figure 3.3: Cut-away view of the ATLAS calorimeter systems. Image taken from [21].

The EM calorimeter is finely segmented in the region surrounding the inner detector, making it ideally suited for identifying electrons and photons. Its electrodes are arranged in an accordion shaped geometry, providing complete azimuthal coverage. Lead absorber plates, covering the whole acceptance, ensure that there are sufficient radiation lengths[3] to mitigate EM particle interaction. To expedite energy-loss corrections due to material upstream of the calorimeter (such as the ID), a presampler — consisting of an active LAr layer — is installed in the region $|\eta| < 1.8$.

The hadronic calorimeter is constructed in two parts, defined by their technologies: the tile and LAr hadronic end-cap calorimeters. Each component is segmented into three layers, providing the sufficient interaction lengths, λ_l (analogous to radiation lengths) to mitigate hadronic particle interaction. The tile calorimeter, comprised of steel absorbers and active scintillating tiles, is located directly outside the EM calorimeter barrel. The LAr hadronic end-cap calorimeters are positioned immediately behind the EM end-cap calorimeters, and consist of interleaved copper plates and active LAr gaps. Their coverage ($1.5 < |\eta| < 3.2$) is such that they overlap slightly

---

[3] A single radiation length (X_0) is defined as the mean path length a radiating particle (such as an electron) traverses in material before its energy is reduced by a factor $1/e$.

with both the tile and forward calorimeters, reducing the drop in material density in the transition regions.

3.2.4 Forward calorimeters

The ATLAS forward calorimeters (FCal) cover an η range $3.1 < |\eta| < 4.9$ and have to withstand what is arguably the harshest radiation environment in ATLAS (see Table 1.5 in [21]); located 5 m from the interaction point, they are subject to a high particle flux compared to the central calorimeters. Moving from the interaction point out, they are comprised of one EM module and two hadronic modules, with the former recessed approximately 1.2 m with respect to the EM calorimeter front face to reduce its exposure to excessive radiation. As such, the FCal must substitute a large volume for increased density — in the EM (hadronic) modules, copper (tungsten) is used to construct metal matrices of concentric rods and tubes parallel to the beam axis, with active LAr filling the gaps between the rods and tubes.

The FCal plays an important role in searches for particles beyond the Standard Model, especially those involving final states with large missing transverse energy.

3.2.5 Muon spectrometer

A three component (one barrel and two end-cap) toroidal magnet system defines the overall geometry of the muon spectrometer, and hence the ATLAS detector as a whole. It features an eight-fold azimuthal symmetry (Figure 3.4), with the barrel toroid providing 1.5 to 5.5 Tm of bending power in the pseudorapidity range $0 < |\eta| < 1.4$, and the end-cap toroids delivering approximately 1 to 7.5 Tm in the region $1.6 < |\eta| < 2.7$; in the transition region where the two magnet systems overlap, this bending power is reduced. Combined with the large volume and low density of the structure, the muon spectrometer enables high resolution tracking whilst minimising the probability of multiple-scattering.

Located variously between the barrel and end-cap components, its main subsystems are:

- Monitored drift tubes (MDT), for precision tracking, covering $|\eta| < 2.7$

- Cathode strip chambers (CSC), for precision tracking, covering $2.0 < |\eta| < 2.7$
- Resistive plate chambers (RPC), for triggering, covering $|\eta| < 1.05$
- Thin gap chambers (TGC), for triggering, covering $1.05 < |\eta| < 2.4$

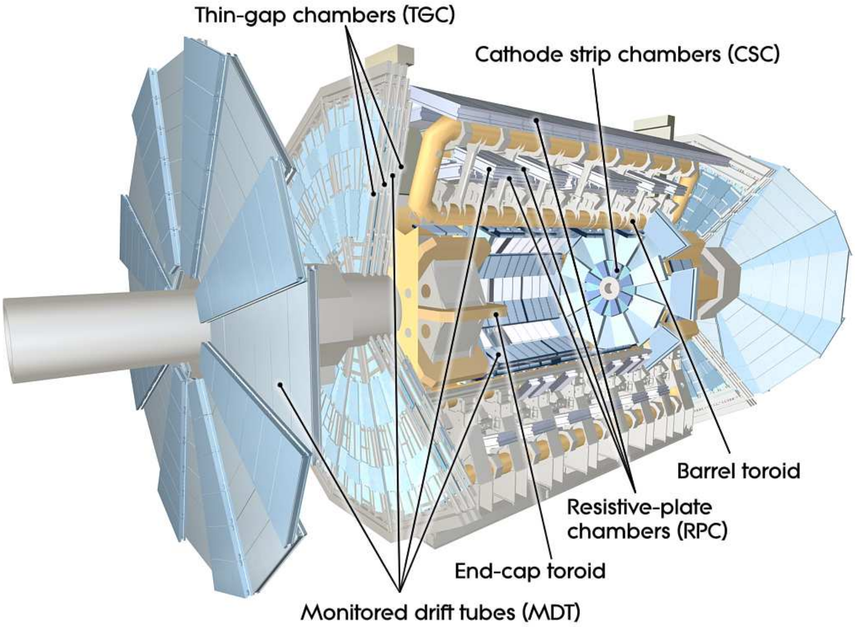

Figure 3.4: Cut-away view of the ATLAS muon spectrometer. Image taken from [21].

Similar to the ID, in the barrel component the tracking chambers are aligned parallel to the beam axis, and in end-cap regions they are arranged perpendicularly. The MDT performs precision measurements over most of the muon spectrometer $\eta-$range, while at large pseudorapidities the CSC — comprised of multi-wire proportional chambers with cathodes segmented into strips — facilitates high granularity tracking to meet the requirements of high rates and backgrounds. The RPC (barrel) and TGC (end-caps) constitute the muon spectrometer trigger system, covering a pseudorapidity range $|\eta| < 2.4$. Along with measuring muon co-ordinate information in the plane orthogonal to the tracking chambers, the trigger system also provides bunch-crossing identification and enables well-defined p_T thresholds.

3.3 The ATLAS trigger

The ATLAS trigger system is designed to reduce the rate of data taking by a factor of $2 \cdot 10^5$, with the aim of recording the few interesting events in every million to tape. Since the hardware designed to select these interesting events must make a decision with a latency of approximately 2μs, an efficient and robust trigger system is necessary. ATLAS tackles these criteria with a three level trigger system (Figure 3.5) that optimises between rapid selection and reliable identification.

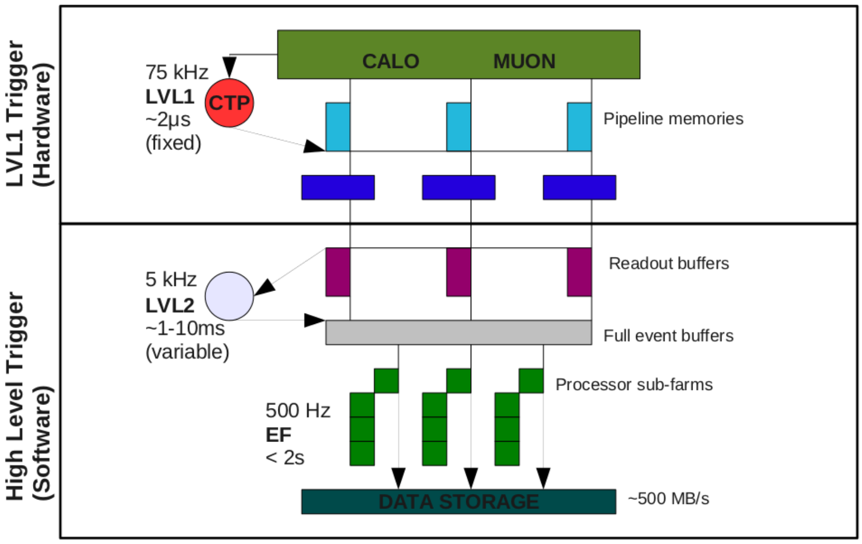

Figure 3.5: Block schematic of the ATLAS trigger system.

Starting from the smallest latency and increasing, they are:

- The level 1 trigger (LVL1), hardware-based with a fixed latency of 2μs. It takes readings at a rate determined by the Central Trigger Processor (CTP), which defines the ATLAS internal clock frequency (usually 40 MHz). As shown in Figure 3.5, the calorimeter and muon systems provide hardware-based triggering at this level. During its latency it must determine one or more slices from the detector's read-out that contain the most interesting fraction of a given event: termed a region of interest (RoI)[4], this information is passed to the next level via the readout drivers; if no RoI is found then the event is ignored.

---

[4] An RoI is a rectangular cone in the $\eta - \phi$ plane opened in the $z-$direction to allow for uncertainty in the primary vertex position.

- The level 2 trigger (LVL2), software-based with a latency of order 10ms. Taking the RoI passed through the readout buffers at LVL1, the LVL2 algorithms reconstruct the data from this slice of the detector only. Therefore at this stage events are selected on the basis of partial reconstruction: this allows for a high event selection efficiency while avoiding the huge bandwidth required to reconstruct complete events.
- The event filter trigger (EF), also software-based and with a latency of order 1s. Based on the events passed at LVL2, the EF algorithms, which are similar to their offline counterparts, run a full reconstruction in the RoI on the processor sub-farms, allowing for refined alignment and calibration; if an event passes the EF, it is written to tape.

The two software triggers comprise what is termed the high level trigger (HLT), which is responsible for running the object reconstruction algorithms. As detailed in Chapter 6, in order to prevent the loss of interesting physics signatures these algorithms must meet the requirements of the highest object reconstruction efficiency possible given the limited time within which they operate. Furthermore, it is essential that they operate within the designated latencies; not doing so can cause the computing farms to lag behind the detector's data output rate.

3.3.1 Inner detector trigger algorithms

Part of this work (Chapter 6) concerns measurements of the inner detector trigger algorithms' track reconstruction efficiency. As such, a detailed description of the relevant algorithms is given here.

The main difficulty with conducting fast and efficient tracking is the high occupancy per event due to additional proton-proton interactions that can accompany the hard-scatter. It is by exploiting the differences between pile-up and interesting physics interactions that the number of detector hits can be reduced before track reconstruction begins; namely, these differences are:

- they occur at different places along the beam line ($\sigma_z \approx 6$ cm)
- physics tracks from the leading-order process have, on average, higher p_T

The first two ID LVL2 algorithms described here, IDSCAN and SiTrack, utilise these distinctions in differing implementations. Both were employed during the 2010-2012 data taking period, with the IDSCAN algorithm used primarily for pattern recognition in the muon and electron trigger channels, and SiTrack used primarily in the tau and b-jet trigger channels. Furthermore, a new framework (L2STAR) was developed for 2012 data taking. It provides implementations of the 2012 equivalents of both IDSCAN and SiTrack, labelled Strategy A and Strategy B, respectively, and also features a new algorithm, labelled Strategy C.

The EF algorithm used in all data taking periods represents an implementation of the algorithms used in offline processing, which use a more precise description of the detector geometry. To be operational in the HLT, the EF algorithm is configured to run within the required latency.

3.3.2 IDSCAN

This algorithm performs pattern recognition in the ID using space points identified in the pixel and SCT detectors. It operates by first finding the position of the primary vertex, performed by populating a histogram with the $z-$intercept of all possible pairs of space points in fine $\phi-$slices in the RoI and identifying peaks in the resulting distribution (Figure 3.6a). Restricting the pairings to small $\phi-$slices reduces combinatorial background from low-p_T tracks, which bend more in the B-field, resulting in a small number of hits in several $\phi-$slices. Furthermore, more weight is naturally given to high-p_T particles, which leave a large number of hits in adjacent $\phi-$slices.

Due to the high occupancy of particles in the ID, there will always be an incoherent spray of space points in the RoI (Figure 3.6b,c). Given that space points from high-p_T tracks associated with the primary vertex will have similar (η, ϕ) co-ordinates, a 2D histogram containing each space point's (η, ϕ) is constructed (Figure 3.6d). After cuts are placed in terms of $r - \phi$, this histogram is used to identify groups with at least four space points in different detector layers.

Finally, these groups are used to construct a 2D histogram in $(1/p_T, \phi)$, filled for all possible combinations of triplet space points. Track candidates (Figure 3.6e,f) are required to have, again, at least four space points from different detector layers. The track p_T resolution is then improved by extending to the TRT.

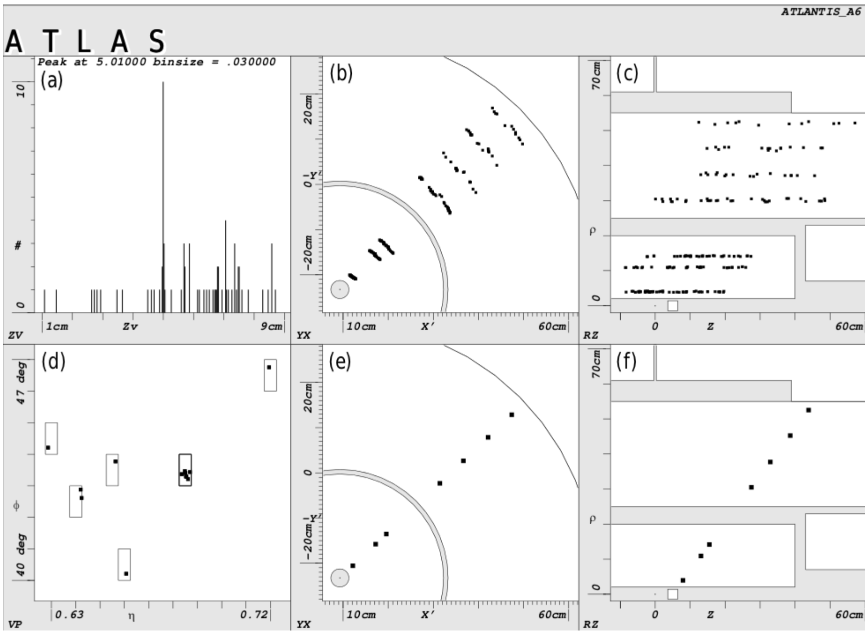

Figure 3.6: The IDSCAN pattern recognition process in graphical format, for a simulated electron RoI: (a) the $z-$intercept histogram, showing a clear peak at $\sim 5cm$; (b,c) all space points in the $x-y$ and $r-z$ planes of the RoI, before cuts; (d) the 2-D histogram in (η, ϕ), with all the hits from the electron collected in a single bin; (e,f) the reconstructed track, viewed in the $x-y$ and $r-z$ planes. Taken from [23].

3.3.3 SiTrack

Similar to IDSCAN, SiTrack uses space points registered in the pixel and SCT detectors. However, instead of first identifying the primary vertex, it begins by treating space points in terms of a predefined list of detector layers, termed *logical layers*. These layers represent various combinations of space point information from the detector layers; for example, a single logical layer may be comprised of several barrel and end-cap detector layers.

A track seed is formed by pairing space points from the two innermost logical layers. It is then extrapolated back to the beam-line, with a requirement placed on the transverse impact parameter to ensure the track provenance was the interaction vertex. Furthermore, a histogram of the longitudinal impact parameter is used to identify, by way of local maxima, the $z-$position of the interaction vertex.

Provided that the seed can be associated with any reconstructed vertex, it is extrapolated to the outer logical layers to form a triplet of space points. Fitting is then performed between the inner and outer space points in the longitudinal and transverse planes. Finally, all remaining triplets of space points are merged and the fitting performed again, yielding the final track parameters.

3.3.4 L2STAR

The L2STAR framework represents an effort to combine both the IDSCAN and SiTrack algorithms in a common coding structure, allowing their respective track pattern recognition techniques to be used in a modular format. This enables easy optimisation of the algorithms to specific physics signatures. In 2012 data taking, the separate implementations of IDSCAN and SiTrack were replaced with their L2STAR equivalents, labelled Strategy A and Strategy B, respectively. These algorithms employ the same code structure but with some optimisation of the ingredient parameters. For example, the IDSCAN $\phi-$slices were reduced in size and a tighter requirement was placed on the $z-$position of potential vertex candidates. These were adjusted to improve the pattern recognition performance in the high-pileup environment created by the LHC running with an instantaneous luminosity of the order of $1 \cdot 10^{34}\text{cm}^{-2}\text{s}^{-1}$. The effects of the adjusted parameters on the tracking performance are discussed in Chapter 6. Furthermore, a pilot algorithm employing offline software pattern recognition techniques similar to the EF software, labelled Strategy C, was also tested during 2012 running.

As a final note, it should be highlighted that there are numerous reconstruction algorithms using data from different detector components; the aforementioned represent just a few of the many physics-finding processes run by the ATLAS trigger.

Chapter 4

Measuring the transverse energy flow

"To stop the flow of music would be like the stopping of time itself,
incredible and inconceivable."
— Aaron Copland

The primary aim of the LHC experiments is to make measurements about and above the electroweak symmetry breaking scale ($\mathcal{O}(100\text{ GeV})$), with the ultimate aim of discovering new physical processes. Though these processes typically produce high energy signatures — distinguishing them from the myriad of soft interactions — they suffer from low cross-sections and as such require high instantaneous luminosities in order to occur. This in turn increases the number of additional interactions per bunch crossing, each of which contributes to the debris of non-perturbative QCD. In order to pick out the particles of interest, and ensure that their measured 4-vectors are not contaminated by spurious contributions from the underlying event (described in Section 2.4.3), it is important to model this non-perturbative contribution as accurately as possible.

Previous measurements of inclusive pp interactions [24–27] and the underlying event [28–33] have been made with ATLAS; however, all were restricted to the acceptance of the inner detector ($|\eta| < 2.5$), as they either used the tracking information directly — in the case of counting particle tracks — or implicitly — in the case of calibrating calorimeter information. The CMS collaboration also performed a measurement of inclusive pp events and the underlying event [34]; this, however, was restricted to the forward calorimeter ($3.15 < |\eta| < 4.9$) and solely measured the mean ΣE per event.

This measurement utilises the full acceptance of the ATLAS calorimeters ($|\eta| < 4.8$) and provides ΣE_T distributions as well as their means. This is performed with two distinct data sets, termed the "minimum bias"[1] and "di-jet" samples, yielding, respectively, a complete description of both "pile-up" — a jargon term for additional pp interactions accompanying the hard scatter — and the underlying event at the LHC general purpose detectors.

To demonstrate the necessity for a complete understanding of pile-up events, Figure 4.1 shows the maximum mean number of interactions per bunch crossing[2] versus month during the pp runs in 2010 to 2012, as recorded by the ATLAS detector. The number steadily increases across the years, which reflects the LHC achieving the injection of increasingly larger numbers of proton bunches, more protons per bunch and a smaller separation in time between the bunches [35].

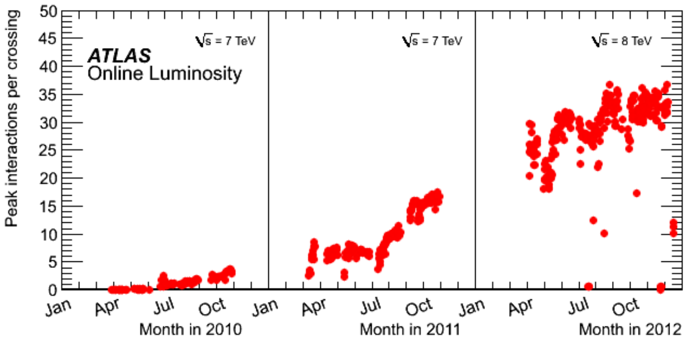

Figure 4.1: The maximum mean number of events per bunch crossing as a function of time during pp runs in 2010-2012, as recorded by ATLAS. Produced by the ATLAS luminosity measurement group, from work conducted in [35].

Furthermore, modelling of the relative central-to-forward[3] activity (a loose term referring to the number and energy of particles), and of the forward region itself, is currently not well constrained, making this analysis intrinsic to a complete picture of soft QCD at the LHC.

---

[1] The term "minimum bias" indicates that the sample is as inclusive as possible.

[2] This number varies according to a Poisson distribution, as the events occur with a known rate and are independent in time of each other.

[3] Here, central is defined as $0 < |\eta| < 3.2$ and forward as $3.2 < |\eta| < 4.8$.

4.1 Definition of hadron level variables

The data used in these analyses are unfolded back from the detector to the hadron level (the unfolding process is discussed extensively in Section 4.5). The hadron level variables are defined as follows: the ΣE_T per event is constructed from all stable[4] neutral particles with $|p| > 200$ MeV and all stable charged particles with $|p| > 500$ MeV. These cuts are chosen so as to best reflect the types of particles that deposit a significant fraction of their energy in the detecting medium; low energy particles can, for example, be forced into helices by the magnetic field before reaching the detector. A quantitative analysis supporting these values was performed by matching charged and neutral hadron level particles to their detector level counterparts, and hence measuring the energy fraction a given particle deposits in the calorimeter as a function of its momentum.

The ΣE_T distribution is constructed such that $\frac{1}{N_{\mathrm{evt}}}\frac{dN_{\mathrm{evt}}}{d\Sigma E_T}$ is a function of the ΣE_T, where N_{evt} is the total number of events in the sample. This is performed separately in adjacent regions of absolute pseudorapidity space, each of width 0.8, for $0 < |\eta| < 4.8$, totalling six regions, or $|\eta|$ "bins". From this variable the mean ΣE_T per unit $\eta - \phi$ in each $|\eta|$ bin is extracted. It is defined as $\frac{1}{N_{\mathrm{evt}}}\frac{d\Sigma E_T}{d\eta d\phi}$, and hereon called the E_T^{flow}. For the inclusive pp analysis, these variables are defined for the full $\phi-$space; the underlying event analysis, however, measures them in the region transverse in ϕ to the hard scatter — specifically, for $\frac{\pi}{3} < |\Delta\phi| < \frac{2\pi}{3}$, where $|\Delta\phi|$ is the angle between the leading jet and any other particle. This region has been shown [36] to be most sensitive to measurements of the underlying event, since it is away from the phase space occupied by the hard scatter.

4.2 Selection criteria

Most analyses in particle physics use *a priori* knowledge of the studied process to isolate the desired events, or *signal*, from the *background*, which is the collective term for every other type of event. In practice matters are not always so clear-cut: an irreducible background may also be present in the signal events, which obviously can not be eliminated by removing the event altogether. By design, the minimum

---

[4] As noted in Section 2.7, a stable truth particle has proper lifetime $\tau > 3 \times 10^{-11}$s.

bias measurement presented here is essentially free of this irreducible background, making it a truly inclusive measure of pile-up activity at the LHC. The di-jet measurement is more complicated, and has a correspondingly involved selection to minimise background events.

4.2.1 Hadron level minimum bias selection

In the minimum bias sample, rudimentary requirements are made to ensure a pp collision occurred. An event is required to have at least 2 charged particles with $p_T > 250$ MeV and $|\eta| < 2.5$; this is essentially a vertex cut, made to reflect the explicit vertex requirement made at the detector level. It is worth noting that the p_T cut is higher than in the detector case, which includes tracks down to $p_T = 150$ MeV. However, due to track and vertex inefficiencies, reconstructed events with at least two $p_T = 150$ MeV tracks will usually have more than two 150 MeV charged particles present when a vertex is required. As a result, reconstructed events with at least two $p_T = 150$ MeV tracks have the same E_T^{flow} as events with at least two $p_T = 250$ MeV charged particles. The cut at $p_T > 250$ MeV was chosen as it minimised the difference, in terms of the hadron level E_T^{flow} defined by MC models used in this analysis, between the hadron and reconstructed level event selections.

4.2.2 Hadron level di-jet selection

A di-jet event is formed when two partons recoil off each other and hadronise. Therefore, to select a di-jet event, at least 2 anti-k_T truth jets with $E_T^{jet} > 20$ GeV and $R = 0.4$ are required. Additionally, the leading and sub-leading jets in the event are required to be central ($|\eta| < 2.5$), well balanced ($\frac{E_T^{jet2}}{E_T^{jet1}} > 0.5$, where $E_T^{jet1(2)}$ is the E_T of the (sub)-leading jet) and back-to-back ($|\phi^{jet1} - \phi^{jet2}| > 2.5$ radians, where $\phi^{jet1(2)}$ is the ϕ of the (sub)-leading jet). These balancing cuts help to suppress events with more than two high energy jets, as the presence of additional jets could contaminate the phase space transverse to the two leading jets.

4.2.3 Reconstructed minimum bias selection

The main sources of background in the minimum bias sample are from empty events, where no collision occurs, and beam noise, which can occur if the beam halo interacts with the detector. To ensure a collision occurred, signal events are required to:

- Have passed selection by the `L1_MBTS_1` trigger
- Feature one primary vertex with 2 or more associated tracks with $p_T > 150$ MeV
- Contain no additional vertices with 5 or more associated tracks with $p_T > 150$ MeV.

The `L1_MBTS_1` trigger requires that at least 1 of the 32 scintillators on the minimum bias trigger scintillator disks ($2.09 < |\eta| < 3.84$) be above noise threshold — this helps to ensure that the event is not background. The second requirement furthers this aim, while the third helps protect against additional pp interactions; 5 associated tracks are required to avoid removing particle decays from secondary vertices, which typically have a small number of tracks and should not cause an event to be vetoed.

4.2.4 Reconstructed di-jet selection

To control the backgrounds mentioned in the previous section, exactly the same requirements are placed on potential di-jet events. Additional cuts on the jets are made to ensure a well balanced, back-to-back di-jet topology is selected. In full, signal events are required to:

- Have passed selection by the `L1_MBTS_1` trigger
- Feature one primary vertex with 2 or more associated tracks with $p_T > 150$ MeV
- Contain no additional vertices with 5 or more associated tracks with $p_T > 150$ MeV
- Contain at least 2 jets, with:
    (a) $E_T^{\text{jet}} > 20$ GeV
    (b) $|\eta^{\text{jet}}| < 2.5$

(c) $|\phi^{\text{jet1}} - \phi^{\text{jet2}}| > 2.5$ radians

(d) $\frac{E_T^{\text{jet2}}}{E_T^{\text{jet1}}} > 0.5$

Where jet1 and jet2 refer to the leading and sub-leading jet, respectively.

As with the hadron level di-jet selection, the cuts listed (b), (c) and (d) endeavour to ensure a back-to-back, well-balanced, central di-jet topology.

4.3 Data samples

This analysis uses data collected by ATLAS from $\sqrt{s} = 7$ TeV pp collisions during the first LHC runs of 2010. The minimum bias analysis uses an integrated luminosity[5] of 7.07 μb^{-1}, a subset of the 585 μb^{-1} used by the di-jet analysis. These data were collected during low instantaneous luminosity runs, and as such the level of pile-up present was very low (of order 0.01 peak number of pp interactions per bunch crossing). This is necessary to ensure that pile-up does not contaminate the measurement, which is designed to be a measurement of the effects of pile-up itself. Events in both datasets were checked against a Good Runs List (GRL), which requires that a given event was recorded during stable beams and without any major faults in the detector modules.

The MC models and tunes used to correct the data for detector effects, provide systematic checks in the correction process, and make final comparisons to data are described in detail in Section 2.7.

Table 4.1 displays event counts for the minimum bias samples, and Table 4.2 shows a more detailed equivalent for the di-jet samples.

4.3.1 Data analysis

The data produced by the ATLAS detector are written to raw (byte stream format) data files. These are passed through reconstruction software, which processes the raw data to produce objects — such as jets — to be used at the analysis level. The

---

[5] In particle physics, the luminosity is the number of particles per unit area per unit time, multiplied by the opacity of the target.

Data	MC (reco)			MC (truth)		
	ND	SD	DD	ND	SD	DD
388,040	636,731	239,558	261,304	637,934	242,397	264,194

Table 4.1: Number of data and `Pythia 6 AMBT1` MC events passing the minimum bias event selection. Here ND, SD and DD refer to non-diffractive, single-diffractive and double-diffractive processes, as described in Section 2.4.4. The MC samples are merged with each contribution weighted by their relative cross-section.

Selection cut	Data	`AMBT1` (ND)	`AMBT1` (jets)	`4C` (jets)	`H++` (jet)
Total	1.00155×10^8	19,989,200	1,500,750	106,100	474,890
Minimum bias	1,626,830	2,043,640	1,062,506	105,423	472,450
$E_T^{\text{jet1}} > 20$ GeV	173,739	224,717	566,434	58,066	272,795
$E_T^{\text{jet2}} > 20$ GeV	44,156	56,732	20,253	20,199	98,576
$\lvert\eta^{\text{jet1,2}}\rvert < 2.5$	28,413	36,522	13,111	12,553	63,957
$\Delta\phi^{jet1,2} < 2.5$	22,723	28,549	10,195	10,356	49,846
$\frac{E_T^{\text{jet2}}}{E_T^{\text{jet1}}} > 0.5$	21,894	27,530	9,843	9,946	48,261

Table 4.2: Number of reconstructed events passing the di-jet event selection. Here, `AMBT1` is a `Pythia 6` tune, `4C` is a `Pythia 8` tune, and ND refers to non-diffractive events. The `AMBT1` (jets) and `4C` (jets) labels represent samples with varying energies of jets required in the final state, merged according to cross-section. The `H++` (jet) label represents a single sample where events are required to have a final state jet.

final format adopts a simple $n \times m$ matrix structure, with each row representing an event and each column the physical objects associated with that event.

The analysis is performed by processing these data using a standalone `C++` framework. All graphs shown in the following chapter are made using `ROOT` [37], unless specified otherwise.

4.4 Topological clusters

At the reconstructed level, the ΣE_T per event is constructed from topological clusters, which represent a particular treatment of the energy deposited by traversing particles in the calorimeter cells. A scale factor is applied to all clusters to account for any mis-modelling of the detector energy response by the MC used in correcting for detector effects.

A description of the cluster algorithm, the cluster energy scale, the derivation of said scale factors, and the effects of energy deposits from sources other than particles — primarily electronic *noise* — are presented in the following sections.

4.4.1 Clustering algorithm

A topological cluster [38], or topoCluster, is a three dimensional collection of calorimeter cells constructed with the aim of associating energy deposits with particles. A topoCluster is seeded around a single calorimeter cell with $|E| > 4\sigma$, where σ is equal to a standard deviation from the mean energy of the calorimeter electronic noise, which typically ranges from approximately 10 MeV in the first layers of the EM barrel to $\mathcal{O}(100)$ MeV in the FCal [38]. The algorithm proceeds by including all cells adjacent to the seed with $|E| > 2\sigma$, and finishes when no cell adjacent to these contains enough energy to seed another topoCluster. A final check is made for multiple local signal maxima; if more than one is found, the topoCluster is split into a correspondingly smaller number of topoClusters.

Once a topoCluster is constructed, its 4-vector can be calculated. In this analysis, the topoCluster E is measured at the EM scale[6], calibrated using test-beam data [39–42]. A justification for using the EM scale is given in Section 4.4.4. The topoCluster η and ϕ values are calculated from an energy-weighted average of the constituent cell centres. Finally, topoClusters are technically defined as massless objects.

---

[6] In ATLAS, the EM scale represents the electromagnetic energy deposited in the calorimeter cells before corrections for effects such as the lower hadronic response.

4.4.2 Cluster scaling

The MC used in correcting the data for detector effects must simulate the calorimeters measurement of, or response to, low energy particles; if it does not, the correction will be inaccurate. A measurement of this response with the ATLAS calorimeters using $\pi^0 \rightarrow \gamma\gamma$ candidates has been conducted [43] — the π^0 peak is constructed and the data are compared to MC signal plus background templates. A scaling factor $(1+\alpha)$ is then applied to the MC signal template, and the optimal value of α derived by minimising the χ^2 between the signal and background templates and data. This is performed in η bins of the candidates photons, denoted in Table 4.3. The asymmetric nature of the scale factor suggests that the detector response in data differs to that provided by the MC; that is, in reality the detector is not perfectly symmetric. All MC topoClusters in both analyses are scaled according to this prescription before unfolding is performed.

	α	Uncertainty
$-4.8 < \eta < -4.2$	0.04	-0.023, +0.023
$-4.2 < \eta < -3.5$	-0.017	-0.032, +0.034
$-3.5 < \eta < -3.2$	0.01	-0.098, +0.11
$-3.2 < \eta < -2.8$	-0.027	-0.023, +0.025
$-2.8 < \eta < -2.37$	-0.089	-0.025, +0.029
$-2.37 < \eta < -1.52$	-0.022	-0.021, +0.02
$-1.52 < \eta < -1.37$	-0.073	-0.17, +0.18
$-1.37 < \eta < 0$	-0.017	-0.031, +0.025
$0 < \eta < 1.37$	-0.013	-0.031, +0.025
$1.37 < \eta < 1.52$	-0.013	-0.17, +0.18
$1.52 < \eta < 2.37$	-0.031	-0.021, +0.02
$2.37 < \eta < 2.8$	-0.107	-0.025, +0.029
$2.8 < \eta < 3.2$	-0.054	-0.023, +0.024
$3.2 < \eta < 3.5$	0.04	-0.092, +0.1
$3.5 < \eta < 4.2$	-0.042	-0.032, +0.034
$4.2 < \eta < 4.8$	0.01	-0.023, +0.023

Table 4.3: Best fitting α values obtained from the $\pi^0 \rightarrow \gamma\gamma$ fits and systematic uncertainties for each η region. α is defined in the text.

4.4.3 Acceptance

In a given $|\eta|$ bin topoClusters of all energies are included in the ΣE_T, for the whole geometric acceptance of the ATLAS detector except the region $1.3 < |\eta| < 1.32$. In this region topoClusters are found to deposit a larger fraction of their energy in the hadronic calorimeter than topoClusters in the rest of the detector (Figure 4.2a). Though not a problem in itself, corrections to the data are dependent on the MC and its detector description; if there is a difference in the topoCluster hadronic fraction between data and MC, the correction factor will be wrong. This is indeed the case, as shown in Figure 4.2b. Removing topoClusters with hadronic fraction > 0.4 in the region $1.3 < |\eta| < 1.32$ counters this problem, returning similar agreement between data and MC as in the regions bordering this space (Figure 4.2c). The choice of cut is somewhat ad-hoc, and was determined primarily to minimise the difference between data and MC.

4.4.4 Energy scale

As mentioned previously, the cluster energy is measured at the EM scale. A calibrated scale also exists, which employs corrections to account for the calorimeters' lower hadronic response. In a hadronic shower, there are contributions[7] from charged particle ionisation, neutrons from nuclear spallation and non-detectable energy (such as in nuclear binding and neutrinos). The resulting shower therefore has a lower measured energy, or response; corrections made to account for this, and for out-of-cluster and material energy losses, result in calibrated topoClusters. In ATLAS, this calibration is performed for positive energy topoClusters only. Negative energy topoClusters, which the clustering algorithm allows because the seed requirement is in terms of $|E|$, are primarily[8] a result of electronic noise, making corrections unnecessary.

A comparison between the two scale types in terms of the E_T^{flow} is shown in Figure 4.3. It is observed that the calibrated scale generally agrees better with the truth data than the EM-scale, since it accounts for the energy losses mentioned

---

[7] The exact fractions depend on the detecting material and parent hadron energy.

[8] Other background effects also contribute: out-of-time pile-up (additional vertices from previous bunch crossings), capacitive cross-talk (where a signal in one circuit or channel adversely affects another), and noise spikes.

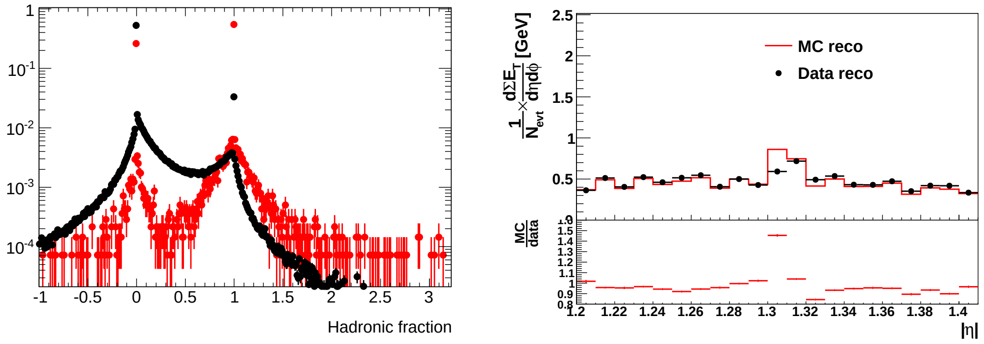

(a) Hadronic E-fraction

(b) E_T^{flow} before

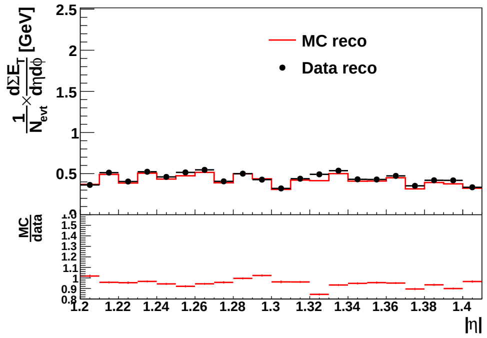

(c) E_T^{flow} after

Figure 4.2: (a) Hadronic energy fraction for topoClusters with $1.3 < |\eta| < 1.32$ (red) and the rest of the calorimeter (black). Figure (b) shows the E_T^{flow} in data and MC and their ratio. The same distribution is shown in (c) after rejecting topoClusters with a hadronic fraction > 0.4 in the region $1.3 < |\eta| < 1.32$.

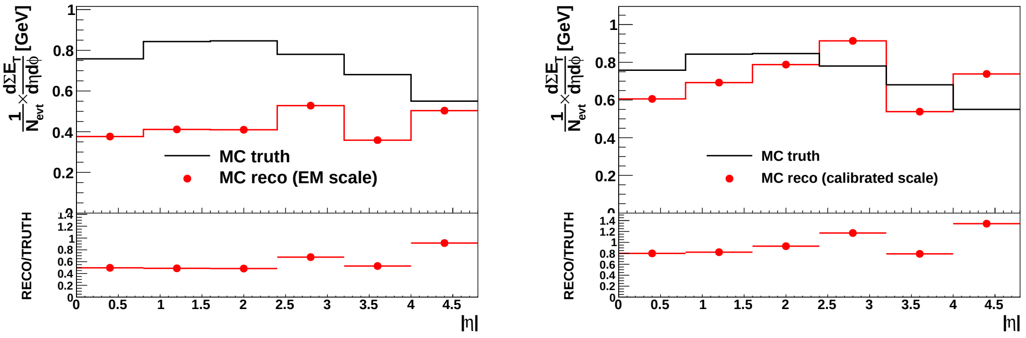

(a) EM E_T^{flow}

(b) Calibrated E_T^{flow}

Figure 4.3: MC reconstructed level E_T^{flow} at the EM (a) and calibrated (b) scales compared to the hadron level E_T^{flow}.

previously. However, in the regions $2.4 < |\eta| < 3.2$ and $4.0 < |\eta| < 4.8$ it performs a significant over-correction, to the effect that the agreement between reconstructed and truth data is worse than for the EM-scale. A similar relationship is observed when examining the ΣE_T distributions in each $|\eta|$ bin explicitly (Figure 4.4).

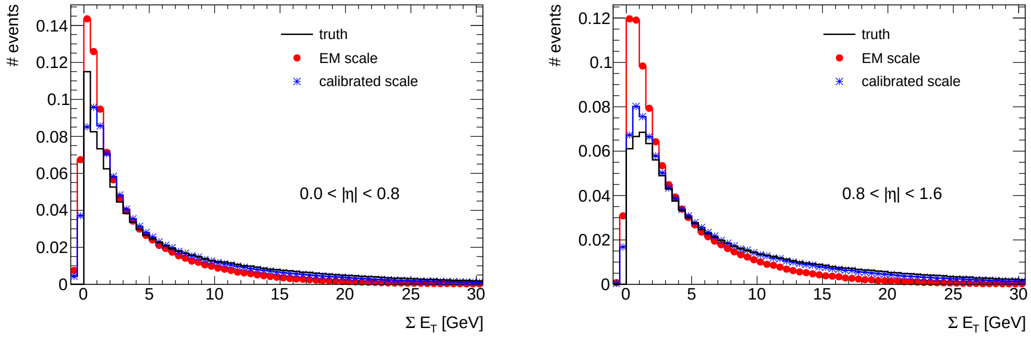

(a) $0.0 < |\eta| < 0.8$ **(b)** $0.8 < |\eta| < 1.6$

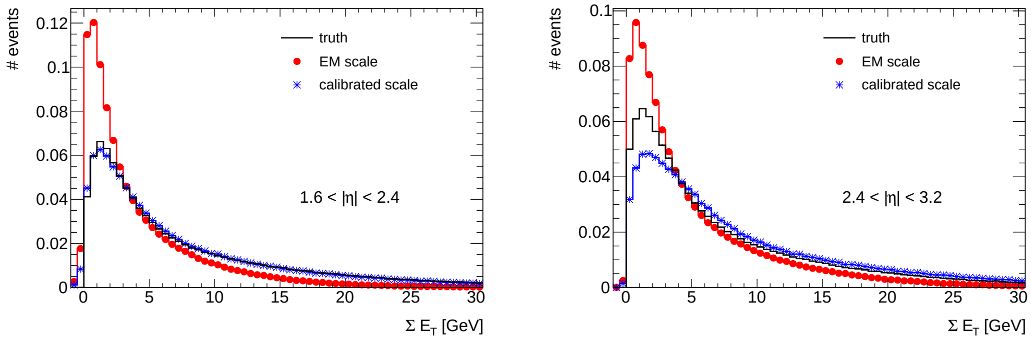

(c) $1.6 < |\eta| < 2.4$ **(d)** $2.4 < |\eta| < 3.2$

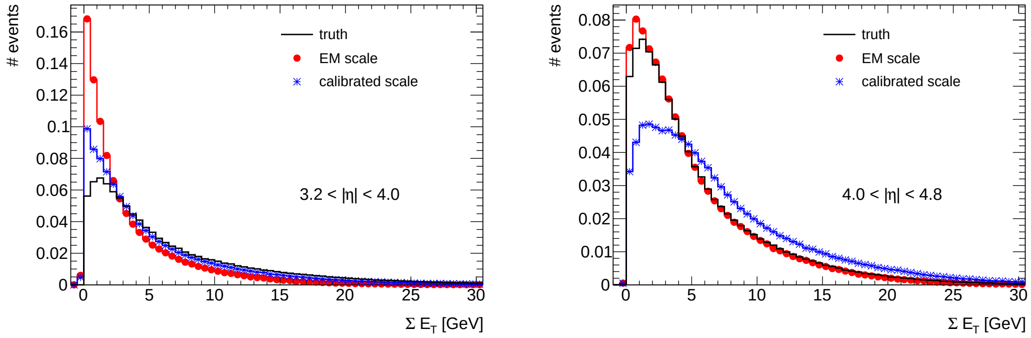

(e) $3.2 < |\eta| < 4.0$ **(f)** $4.0 < |\eta| < 4.8$

Figure 4.4: Truth level ΣE_T compared with EM and calibrated scale ΣE_T at the reconstructed level MC, in the following $|\eta|$ regions: (a) $0.0 < |\eta| < 0.8$, (b) $0.8 < |\eta| < 1.6$, (c) $1.6 < |\eta| < 2.4$, (d) $2.4 < |\eta| < 3.2$, (e) $3.2 < |\eta| < 4.0$ and (f) $4.0 < |\eta| < 4.8$.

To investigate this further, the individual topoCluster E_T distributions in each $|\eta|$ bin at the truth, EM scale and calibrated scale are shown in Figure 4.5. Again the calibration tends to increase the energy of the topoClusters, pulling the distribution closer to the truth. The double peaks observed in the first three $|\eta|$ bins at the truth level can be reasoned in terms of the momentum cuts applied, which have different values for charged and neutral particles ($p >$ 500 and 200 MeV respectively), and remove proportionally more central than forward particles (the latter, by definition, tend to have a higher average momentum). A similar double peaked structure is observed in some $|\eta|$ bins at the calibrated scale. This could be due to corrections designed for EM particles being applied to hadronic deposits (and vice-versa), possible because the correct identification of each type is problematic. Furthermore, since the calibration is not applied to negative energy clusters, an additional double peak centred at $E_T = 0$ is observed.

The observed over-calibration could arise if a single particle is accidentally reconstructed as two separate topoClusters; for example, if only the end of a particle shower reaches the calorimeter, it may be that not all the deposits are sufficiently above the noise threshold, causing gaps to form between the active cells. In this case the calibration algorithm would overestimate the necessary correction — lower energy clusters lose more of their energy before reaching the calorimeters, and as such require a larger correction than higher energy clusters.

While the calibrated scale is generally closer to the truth than the EM scale, the procedure itself has flaws. As discussed previously, this can cause problems when correcting for detector effects if the MC does not properly simulate the conditions present when collecting real data. Figures 4.6a and 4.6b show the E_T^{flow} in the inclusive pp and di-jet data respectively; here, the data are corrected for detector effects by unfolding the ΣE_T spectra in each $|\eta|$ bin (the correction method is described in depth in Section 4.5), with the yellow band indicating the energy scale systematic uncertainty (detailed in Section 4.6). The procedure is performed separately with topoClusters defined at the EM and calibrated scales; since the unfolding process accounts for detector effects and correlations, the two results should ideally be equal — this is indeed the case in the central region. However, in the two $|\eta|$ bins where the calibration significantly over-corrected (Figure 4.3), the results do not converge within systematic error. In particular, the most forward $|\eta|$ bin displays a disagreement at the level of 10%.

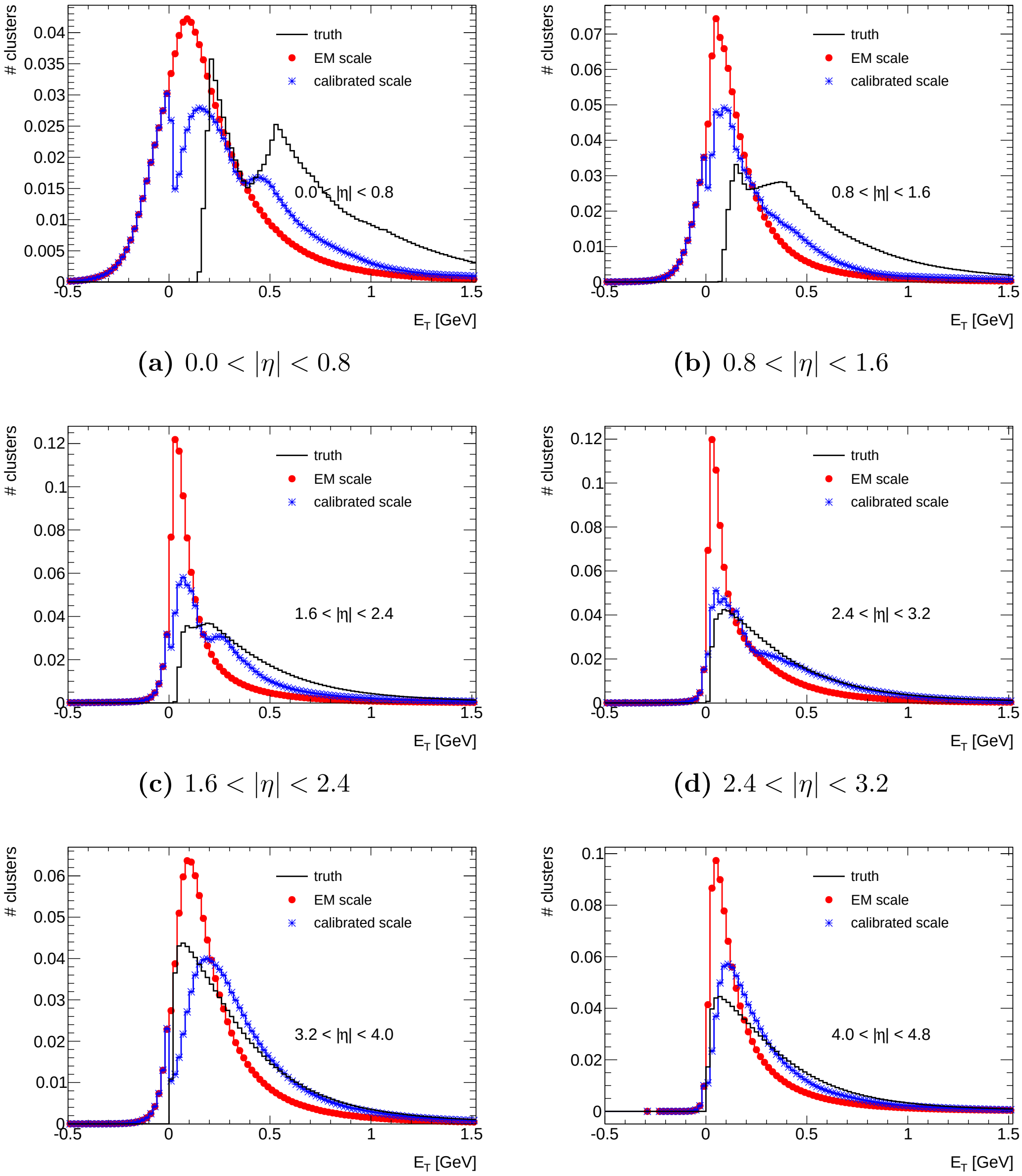

(a) $0.0 < |\eta| < 0.8$ **(b)** $0.8 < |\eta| < 1.6$

(c) $1.6 < |\eta| < 2.4$ **(d)** $2.4 < |\eta| < 3.2$

(e) $3.2 < |\eta| < 4.0$ **(f)** $4.0 < |\eta| < 4.8$

Figure 4.5: Truth level E_T compared with EM and calibrated scale E_T at the reconstructed level MC, in the following $|\eta|$ regions: (a) $0.0 < |\eta| < 0.8$, (b) $0.8 < |\eta| < 1.6$, (c) $1.6 < |\eta| < 2.4$, (d) $2.4 < |\eta| < 3.2$, (e) $3.2 < |\eta| < 4.0$ and (f) $4.0 < |\eta| < 4.8$.

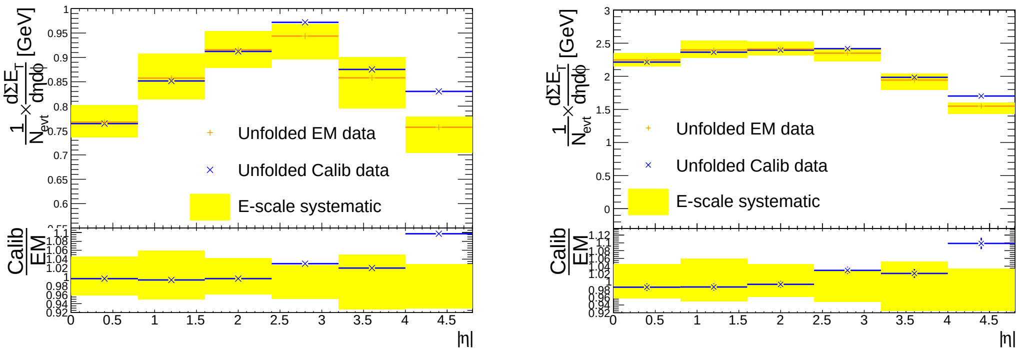

(a) Unfolded EM E_T^{flow} **(b)** Unfolded calibrated E_T^{flow}

Figure 4.6: The E_T^{flow} in data, after unfolding EM- and calibrated scale topoClusters separately, in (a) minimum bias and (b) di-jet data.

A study of the contribution from electronics noise asserted that the noise spectrum at the EM scale is symmetric about zero, whilst the positive energy calibration results in an asymmetric distribution about zero. As such the noise term cancels in the ΣE_T at the EM scale. For this reason, and the fact that the two scales agree after unfolding in all $|\eta|$ bins except the most forward, where the EM scale better reflects the truth distribution, the EM scale is chosen as the default for all analysis topoClusters.

4.5 Unfolding

The data collected by any detector will have been changed in some way by their measurement. Even in a perfectly understood detector it is necessary for particles to interact — and hence lose energy — with it to be measured. Therefore in order to make comparisons between data and physics models, the data need to be corrected back to their natural, or "true", state. This process is known as unfolding.

4.5.1 Bayes' theorem

There are a number of techniques available to perform unfolding [44–46]; this analysis utilises a method based on Bayes' theorem of conditional probability. Its most simple form can be derived quite easily, by way of treating two overlapping probability spaces, $P(H)$ and $P(O)$ ($P(\Omega) = 1$, integrating over all space). Given that an event occurred in O-space, the probability of it also occurring in H-space is given by the fractional contribution of the overlap to O-space:

$$P(H \mid O) = \frac{P(H \cap O)}{P(O)} \tag{4.1}$$

Taking the corresponding relation for an event occurring in H-space:

$$P(O \mid H) = \frac{P(O \cap H)}{P(H)} \tag{4.2}$$

But $P(H \cap O) = P(O \cap H)$, so:

$$P(H \mid O) = \frac{P(O \mid H)P(H)}{P(O)} \tag{4.3}$$

This is the simplest form of Bayes' theorem. By considering the whole space Ω as being a sum of subspaces H_i, Bayes' theorem can be expressed in terms of the total probability:

$$P(H \mid O) = \frac{P(O \mid H)P(H)}{\Sigma_i P(O \mid H_i)P(H_i)} \tag{4.4}$$

Interpreting Equation (4.4) in terms of experimental physics reveals Bayes' theorem as an important tool: for a given observation, it provides the means to determine the probability of a given hypothesis being true.

4.5.2 Applying Bayes' theorem

The application of an iterative Bayes' theorem to experimental particle physics was proposed by D'Agostini [47]. Since this analysis is interested in unfolding distributions — specifically, histograms — the method outlined here is constructed in terms of a given distribution's bins.

As described in Section 2.7, MC software provides the means to simulate physics processes, propagate particles through the detector, and reconstruct their final states. It is therefore an important tool in building a relationship between hypothesis and observation. In terms of matrix algebra, the relationship between each bin of hypothesis, or "truth", T_i^{MC}, and each bin of observation, or "reconstructed", R_j^{MC}, can be given by:

$$R_j^{MC} = \sum_i S_{ij} T_i^{MC} \tag{4.5}$$

Where S_{ij} is called the smearing matrix, which describes the mapping of truth to reconstructed elements. Naively, but mathematically sound, matrix inversion can be used to return the truth distribution of a variable as a function of the inverted smearing matrix:

$$T_i^{MC} = \sum_j S_{ij}^{-1} R_j^{MC} \tag{4.6}$$

However in practice this is not possible, due to the non-linear correspondence between the reconstructed and truth elements.

As such, a new technique must be found to recover the true distribution. A hint at a potential candidate can be found by realising that the denominator of Equation (4.4) is just a normalisation factor; hence, the equation can be restated as:

$$P(H \mid O) \propto P(O \mid H)P(H) \tag{4.7}$$

This looks similar to Equation (4.5), with the smearing matrix S_{ij} being equivalent to $P(O \mid H)$. It is therefore clear that Bayes' theorem can be used to recover the true distribution from data. Re-writing Equation (4.4) in terms of truth and reconstructed histograms:

$$P(T_i^{MC} \mid R_j^{MC}) = \frac{P(R_j^{MC} \mid T_i^{MC})P(T_i^{MC})}{\sum_i P(R_j^{MC} \mid T_i^{MC})P(T_i^{MC})} \tag{4.8}$$

Here $P(T_i^{MC} \mid R_j^{MC})$ is an element in what is called the unfolding matrix, $P(R_j^{MC} \mid T_i^{MC})$ is an element in the smearing matrix, S_{ij}, and $P(T_i^{MC})$ is an element in what is termed the "prior". The prior represents previous knowledge of a given measurement; in this case, an appropriate physics model. Applying this unfolding matrix to the data should remove detector effects and reveal the true distribution:

$$n(C_i^{data}) = \sum_j P(T_i^{MC} \mid R_j^{MC})n(R_j^{data}) \tag{4.9}$$

Where $n(R_j^{data})$ is the number of events in bin j of the measured data histogram, and $n(C_i^{data})$ the number in bin i of the corrected. This histogram represents the data corrected for detector effects, and can be compared directly to theory; it is termed the "posterior".

It is important to note the subtle difference between $P(T_i^{MC})$ from Equation (4.8) and $P(H)$ from Equation (4.4): if the former is constant with varying i then all bins are equally likely; if the latter is constant, all spectra are equally likely. Therefore, while a flat $P(H)$ distribution places no *a priori* emphasis on a particular spectrum, a flat $P(T_i^{MC})$ distribution is a major assumption that usually does not correspond to the distribution in data. As such, the choice of prior has a strong influence on the unfolding matrix, and hence the posterior. This is a feature that initially appears in conflict with the Bayesian philosophy of recovering an unbiased, true distribution.

To counter this, an iterative procedure is adopted whereby the posterior after a single application of the unfolding (the unfolded data distribution) is used as the prior in the next iteration, and so on. This is the heart of D'Agostini's method; how it is applied practically is discussed in more detail in the following section.

4.5.3 Unfolding procedure

The Bayesian unfolding is performed using the Imagiro package [48], which provides a C++ implementation of the method discussed in Section 4.5.1. As input it takes flat `ROOT` ntuples containing truth, reconstructed and real data events, with which it produces matrices and corrected results. Imagiro applies the unfolding procedure on a per event basis and therefore a per event variable is necessary: here, the topoCluster ΣE_T in bins of $|\eta|$ width 0.8 is used. The E_T^{flow} is then calculated by taking the mean of each ΣE_T distribution, dividing by the η bin width, the ϕ phase-space and a factor of 2 to account for each $|\eta|$ bin being filled with both positive and negative η clusters.

4.5.4 Reweighting the MC

Before performing the unfolding, the MC used in unfolding was reweighted to the data in an attempt to reduce the residual model dependence. Despite the iterative procedure, this is necessary as none of the models are constrained by data in the forward region, and hence have wildly varying descriptions. This is particularly important when it is necessary to treat events with MC information exclusively, as will be discussed in Section 4.5.6.

The reweighting is performed such that the reconstructed MC ΣE_T distributions match the data in each $|\eta|$ bin, as shown in Figures 4.7 and 4.8, for minimum bias and di-jet data respectively.

To perform the reweighting itself, the ratio of the data ΣE_T to the MC ΣE_T is fitted with a spline, which provides a smooth interpolation between bin centres. The spline is then used to weight the MC; due to low statistics in the ΣE_T tails, at high ΣE_T the ratio is set equal to the value of the last bin with relative statistical error $< 20\%$. The `Pythia 6 AMBT1` model was chosen as the nominal MC, as it represents a general purpose generator tuned to early ATLAS minimum bias data [49].

4.5.5 Smearing matrices

An example two-dimensional smearing matrix filled on an event-by-event basis with `Pythia 6 AMBT1` truth and reconstructed ΣE_T is shown in Figure 4.9. The off-diagonal elements are inferred as being a result of detector effects; if there was a $\rho = 1$ correlation, the measured value would correspond exactly to the truth. Generally, the truth value is larger than the reconstructed. This is expected, since there are various mechanisms by which particles can lose energy interacting with the detector before depositing the measured topoCluster. The highest bins on each axis represent special event types, and are described in Section 4.5.6.

The bin sizes in all unfolding matrices were chosen so as to ensure the smallest bias when calculating the mean of the ΣE_T in each $|\eta|$ bin, and hence the E_T^{flow}. For the matrix in Figure 4.9, 0.5 GeV wide bins were used for $\Sigma E_T < 50$ GeV, 1 GeV wide bins for $50 < \Sigma E_T < 120$ GeV and 10 GeV wide bins for $\Sigma E_T > 120$ GeV. The range is -6 GeV $< \Sigma E_T <$ 200 GeV, ensuring negative energy topoClusters are also included.

The affect on the unfolded E_T^{flow} due to the choice of bin width in the ΣE_T spectrum can be seen in Figure 4.10, which shows the MC truth E_T^{flow} obtained by taking the mean of the ΣE_T distribution in each $|\eta|$ bin. A special graph type (in

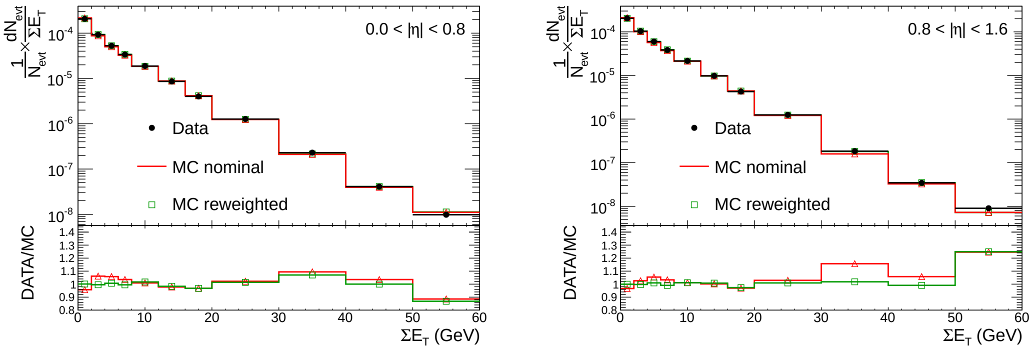

(a) $0.0 < |\eta| < 0.8$ **(b)** $0.8 < |\eta| < 1.6$

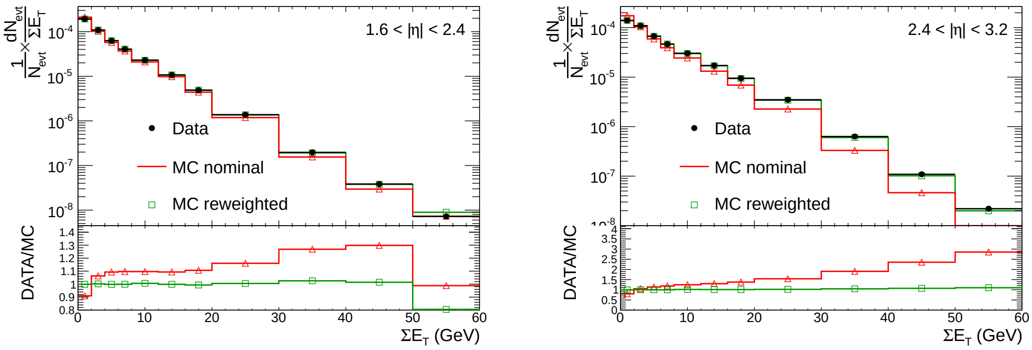

(c) $1.6 < |\eta| < 2.4$ **(d)** $2.4 < |\eta| < 3.2$

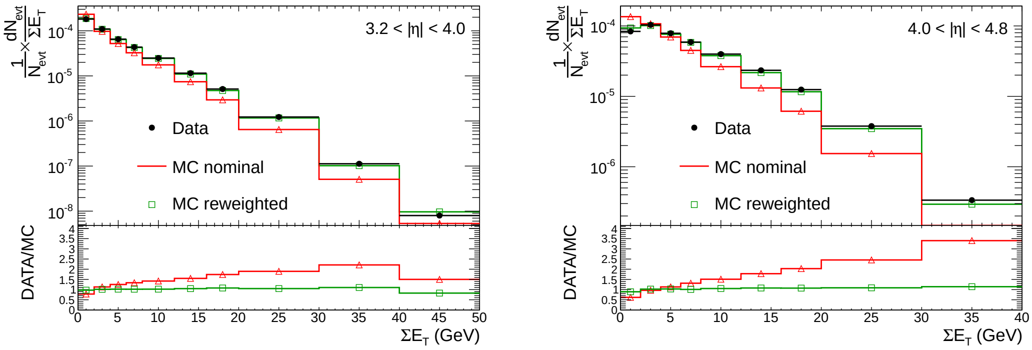

(e) $3.2 < |\eta| < 4.0$ **(f)** $4.0 < |\eta| < 4.8$

Figure 4.7: Minimum bias ΣE_T distributions comparing the data with reconstructed `Pythia 6 AMBT1` MC, before and after reweighting, in the following $|\eta|$ bins: (a) $0.0 < |\eta| < 0.8$; (b) $0.8 < |\eta| < 1.6$; (c) $1.6 < |\eta| < 2.4$; (d) $2.4 < |\eta| < 3.2$; (e) $3.2 < |\eta| < 4.0$; (f) $4.0 < |\eta| < 4.8$.

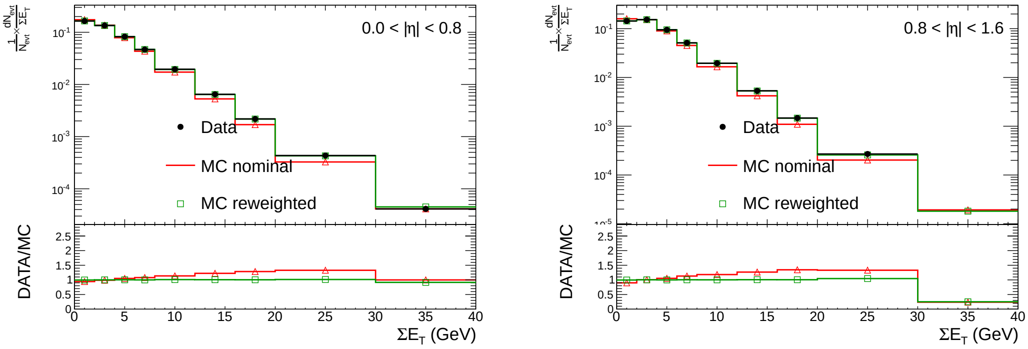

(a) $0.0 < |\eta| < 0.8$ **(b)** $0.8 < |\eta| < 1.6$

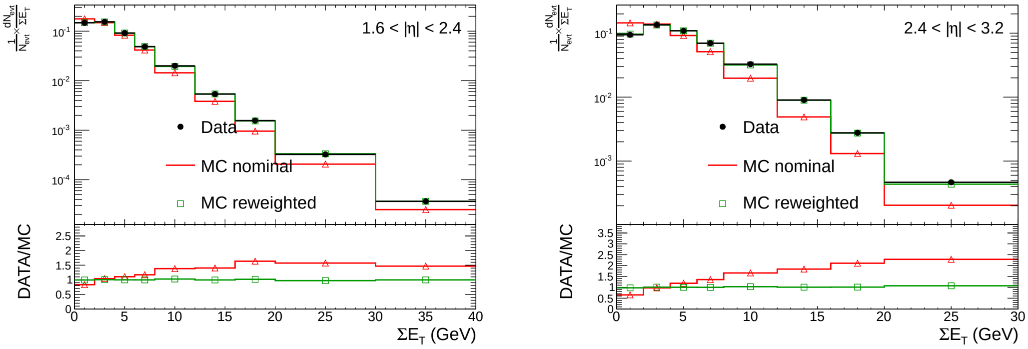

(c) $1.6 < |\eta| < 2.4$ **(d)** $2.4 < |\eta| < 3.2$

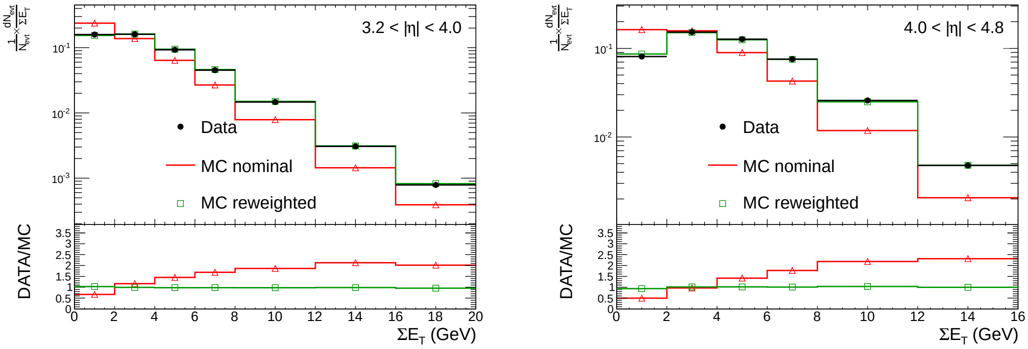

(e) $3.2 < |\eta| < 4.0$ **(f)** $4.0 < |\eta| < 4.8$

Figure 4.8: Di-jet ΣE_T distributions comparing the data with reconstructed `Pythia 6 AMBT1` MC, before and after reweighting, in the following $|\eta|$ bins: (a) $0.0 < |\eta| < 0.8$; (b) $0.8 < |\eta| < 1.6$; (c) $1.6 < |\eta| < 2.4$; (d) $2.4 < |\eta| < 3.2$; (e) $3.2 < |\eta| < 4.0$; (f) $4.0 < |\eta| < 4.8$.

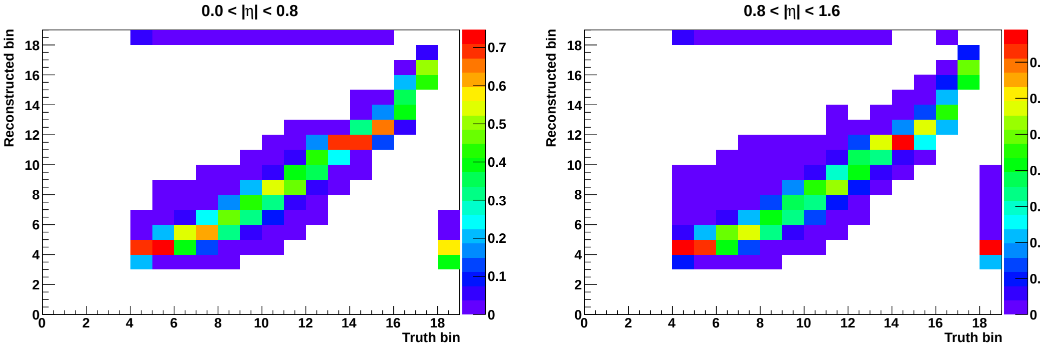

(a) $0.0 < |\eta| < 0.8$ **(b)** $0.8 < |\eta| < 1.6$

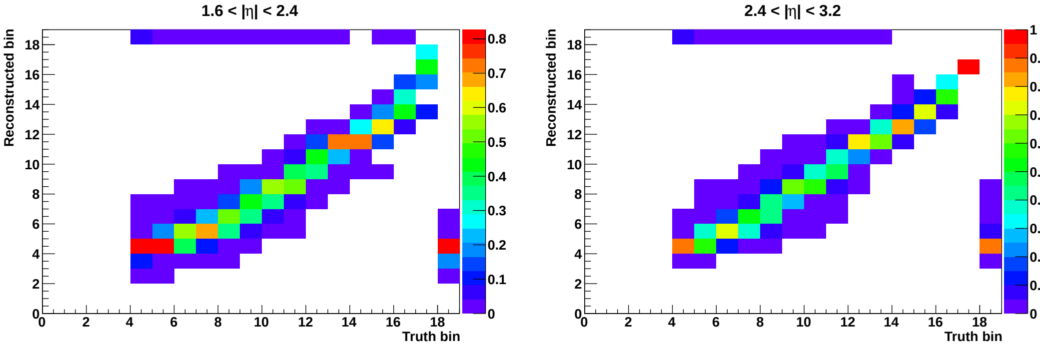

(c) $1.6 < |\eta| < 2.4$ **(d)** $2.4 < |\eta| < 3.2$

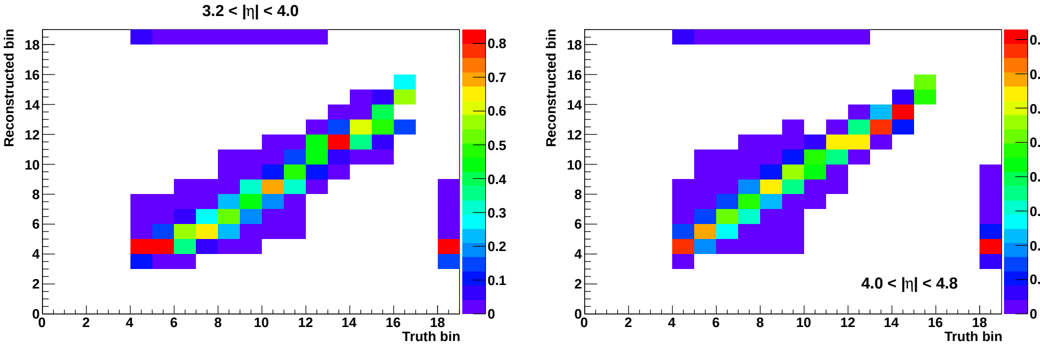

(e) $3.2 < |\eta| < 4.0$ **(f)** $4.0 < |\eta| < 4.8$

Figure 4.9: Minimum bias smearing matrices, after 2 iterations, in the following $|\eta|$ bins: (a) $0.0 < |\eta| < 0.8$; (b) $0.8 < |\eta| < 1.6$; (c) $1.6 < |\eta| < 2.4$; (d) $2.4 < |\eta| < 3.2$; (e) $3.2 < |\eta| < 4.0$; (f) $4.0 < |\eta| < 4.8$. Note that the axes correspond to the bin number of the unfolded distribution and not the units of the input variable. The highest bin (18) on the truth axis is filled for "fake" events, and the highest bin (18) on the reconstructed axis is filled for "missed" events. A description of these event types is given in Section 4.5.6. The magnitude in each bin, denoted by the rainbow bar, indicates the probability that a truth event in bin i is reconstructed in bin j.

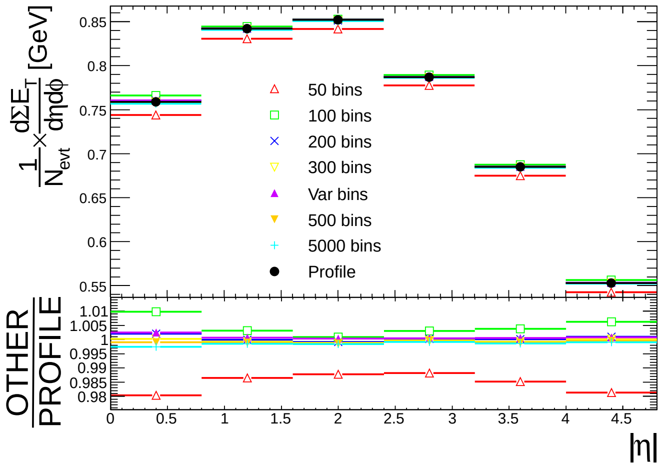

Figure 4.10: The E_T^{flow} formed from the mean of ΣE_T histograms with various numbers of bins compared to that obtained from a TProfile. The points labelled "Var bins" correspond to the variable bin widths used in the matrix. The other points correspond to various numbers of bins (with constant bin width) in the range -6 GeV to 200 GeV.

`ROOT` framework terminology, a TProfile [37]), displaying the mean E_T^{flow} and its error for each bin in $|\eta|$, is chosen as the benchmark because it calculates the "true" mean — it is extracted from an unbinned ΣE_T distribution and hence unbiased by the choice of binning. The maximum deviation from the TProfile is 2% when unfolding with 50 bins, and 1% with 100 bins. All other binning choices result in a deviation of $< 0.5\%$. The unfolded distribution is then rebinned to reduce both the effect of bin-to-bin migrations and statistical errors: 2 GeV wide bins for $0 < \Sigma E_T < 8$ GeV, 4 GeV wide bins for $8 < \Sigma E_T < 20$ GeV and 10 GeV wide bins for $20 < \Sigma E_T < 60$ GeV. The ΣE_T range in each distribution depends on the number of events in the tails.

The smearing matrix is applied to the uncorrected data according to Equation (4.9). This produces a posterior distribution, which is then used as the prior in the next iteration. As explained previously, this lessens the influence of the choice of model on the unfolding process. The number of iterations used was chosen by comparing unfolded distributions produced by various numbers of iterations, shown in Figures 4.11, 4.12 and 4.13. Two iterations were used, as the result converges with those obtained from differing numbers of iterations to within a fraction of a percent in E_T^{flow}, and a few percent in ΣE_T, whilst avoiding the inflation of statistical error with increasing numbers of iterations (this dependency is discussed in Section 4.5.9).

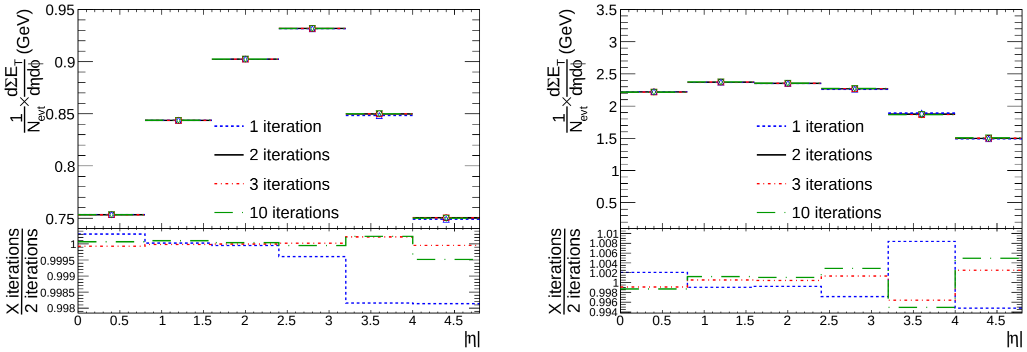

(a) Minimum bias **(b)** Di-jets

Figure 4.11: E_T^{flow} distributions comparing the data unfolded separately with 1, 2, 3 and 10 iterations; all examples use a reweighted `Pythia 6 AMBT1` unfolding matrix, for a) minimum bias, and b) di-jets.

4.5.6 Treatment of one-sided events

Due to the event selection criteria detailed in Section 4.2, there are four possible combinations of event: both reconstructed and truth pass; only truth passes ("missed"); only reconstructed passes ("fake"); and neither pass. The first case is fully accounted for in the smearing matrix, and the last is completely excluded from Equation (4.9). Though the missed and fake events are present in Figure 4.9 (bins 18 on the y and x axes, respectively), this is purely a feature of design on Imagiro's part; they do not feature explicitly in the smearing matrix S_{ij} used to unfold the data, and instead require separate appraisal.

If an event is selected at the truth level only, a correction is applied to each of the unfolded ΣE_T bins. The correction factor is the efficiency, ϵ_i, of a given ΣE_T truth bin, calculated from the distribution of missed events in truth:

$$\epsilon_i = \Sigma_{j=1}^{n_R} P(R_j|T_i) \tag{4.10}$$

Here n_R is the number of reconstructed events, and the efficiency is essentially the probability that an event in bin i of the prior distribution has a partner in any bin of the reconstructed distribution. This factor alters Equation (4.9) such that:

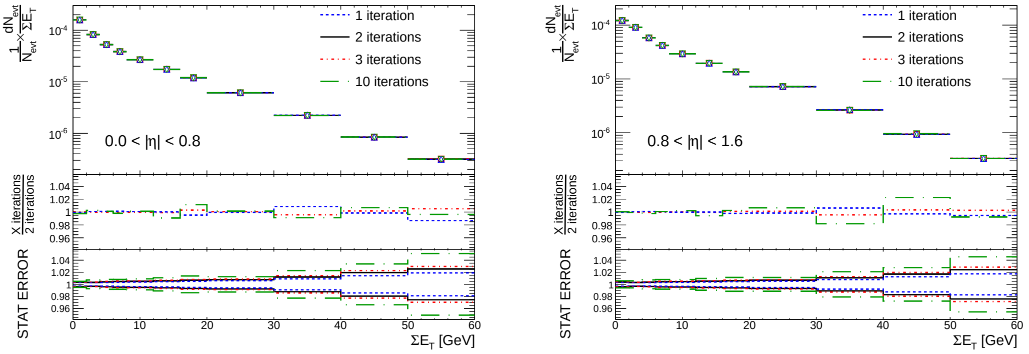

(a) $0.0 < |\eta| < 0.8$ **(b)** $0.8 < |\eta| < 1.6$

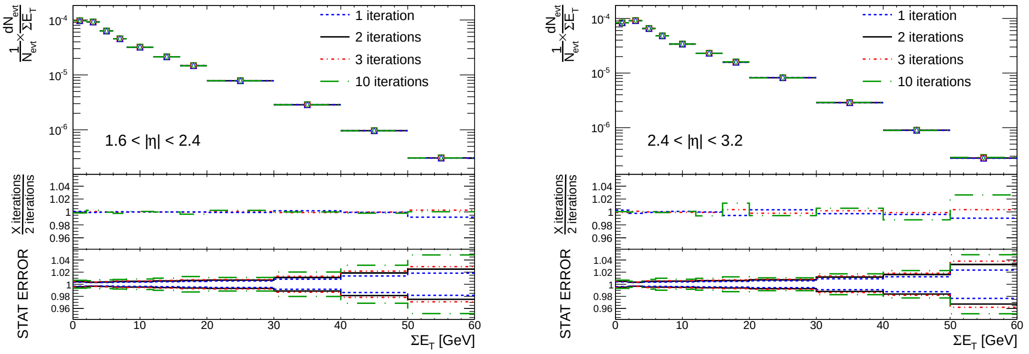

(c) $1.6 < |\eta| < 2.4$ **(d)** $2.4 < |\eta| < 3.2$

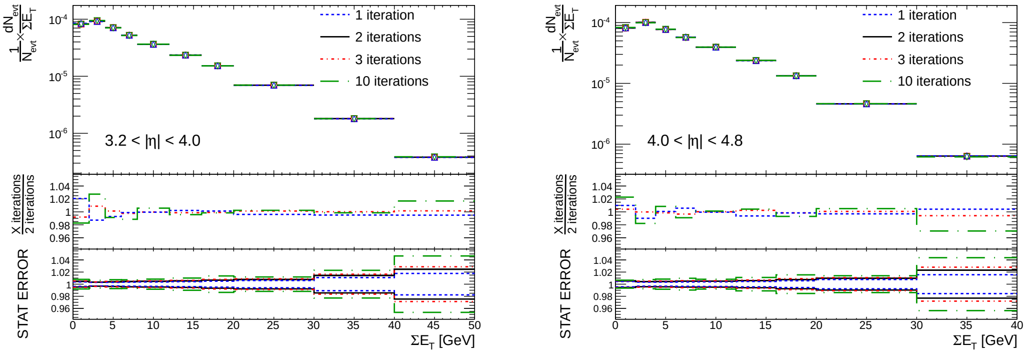

(e) $3.2 < |\eta| < 4.0$ **(f)** $4.0 < |\eta| < 4.8$

Figure 4.12: Minimum bias ΣE_T distributions comparing the data unfolded separately with 2, 3 and 10 iterations; all examples use a `Pythia 6 AMBT1` unfolding matrix. (a) $0.0 < |\eta| < 0.8$; (b) $0.8 < |\eta| < 1.6$; (c) $1.6 < |\eta| < 2.4$; (d) $2.4 < |\eta| < 3.2$; (e) $3.2 < |\eta| < 4.0$; (f) $4.0 < |\eta| < 4.8$.

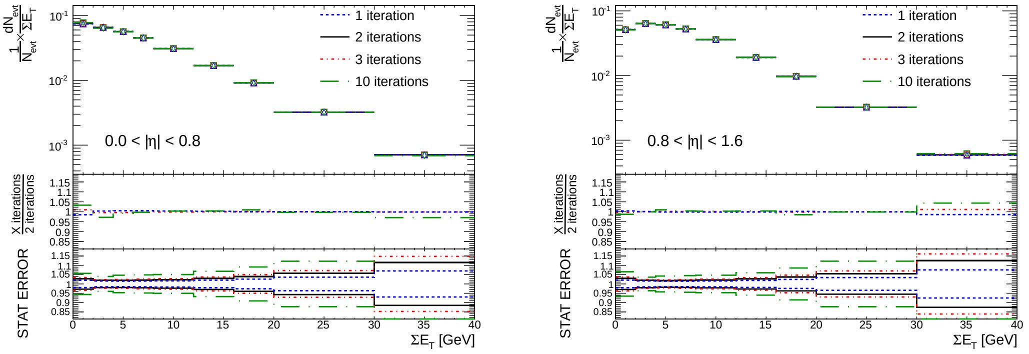

(a) $0.0 < |\eta| < 0.8$ **(b)** $0.8 < |\eta| < 1.6$

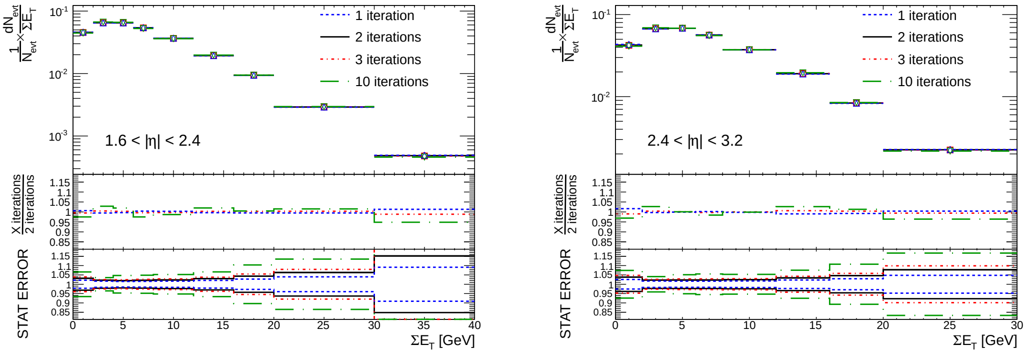

(c) $1.6 < |\eta| < 2.4$ **(d)** $2.4 < |\eta| < 3.2$

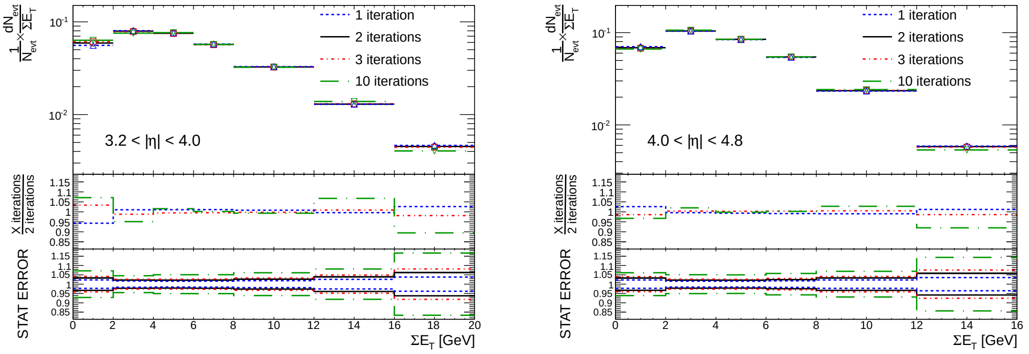

(e) $3.2 < |\eta| < 4.0$ **(f)** $4.0 < |\eta| < 4.8$

Figure 4.13: Di-jet ΣE_T distributions comparing the data unfolded separately with 2, 3 and 10 iterations; all examples use a `Pythia 6 AMBT1` unfolding matrix. (a) $0.0 < |\eta| < 0.8$; (b) $0.8 < |\eta| < 1.6$; (c) $1.6 < |\eta| < 2.4$; (d) $2.4 < |\eta| < 3.2$; (e) $3.2 < |\eta| < 4.0$; (f) $4.0 < |\eta| < 4.8$.

$$n(C_i^{data}) = \frac{1}{\epsilon_i} \sum_j P(T_i^{MC} \mid R_j^{MC}) n(R_j^{data}) \tag{4.11}$$

This procedure is performed after each iteration, thus reducing the dependency of the correction on the choice of prior.

If an event is selected at the reconstructed level only, it is migrated from the reconstructed bin into the fake bin (represented by bin 18 on the $x-$axis in Figure 4.9). This bin is included in Equation (4.8), such that a given reconstructed event has a probability of originating from the fake bin. The probability that a given data event is removed is determined from the fake ΣE_T spectrum in the MC, which is itself determined from the smearing matrix. For example, if there are more fake events with $\Sigma E_T = 1$ GeV than $\Sigma E_T = 10$ GeV then it is more probable that an event will be removed from the former than the latter bin. Since no truth information is available for fake events, this correction is somewhat ad-hoc and dependent on the choice of MC. To counter this, the MC is first reweighted to the data before unfolding. The results of this method are discussed in the following section.

4.5.7 Closure tests

To assess that the Imagiro framework works as expected and does not introduce any spurious bias, simple closure tests[9] are shown in Figure 4.14 and Figure 4.15. These were performed using two statistically independent, reweighted `Pythia 6 AMBT1` samples: the first is unfolded using a matrix constructed from the second, and compared to its truth. The results agree within statistical error, demonstrating that no bias of this type is present.

The importance of reweighting the MC to the data becomes more apparent when considering the treatment of fake events; if the MC provides an inaccurate description of the fake distribution, a bias will be introduced in the correction procedure. Ideally the unfolding process should remove any dependency on the type of event (nominal or otherwise) used to populate the smearing matrix; if the nominal reconstructed

---

[9] The usage of the term ‘closure test’ varies, but it is generally a measure of whether two results coincide within the relevant uncertainties.

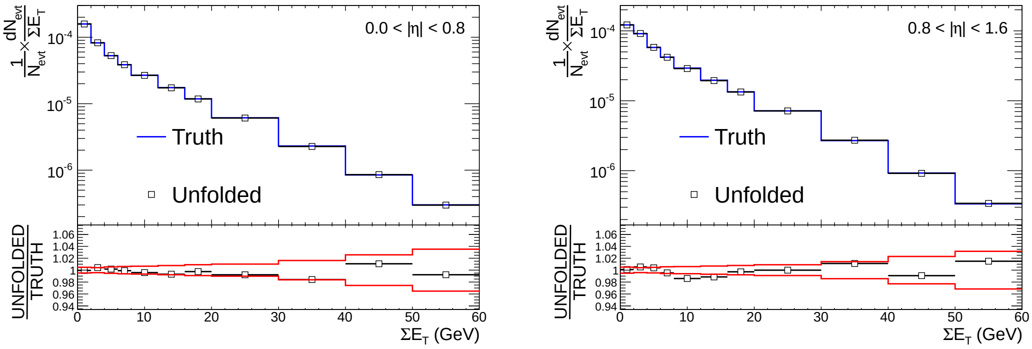

(a) $0.0 < |\eta| < 0.8$ **(b)** $0.8 < |\eta| < 1.6$

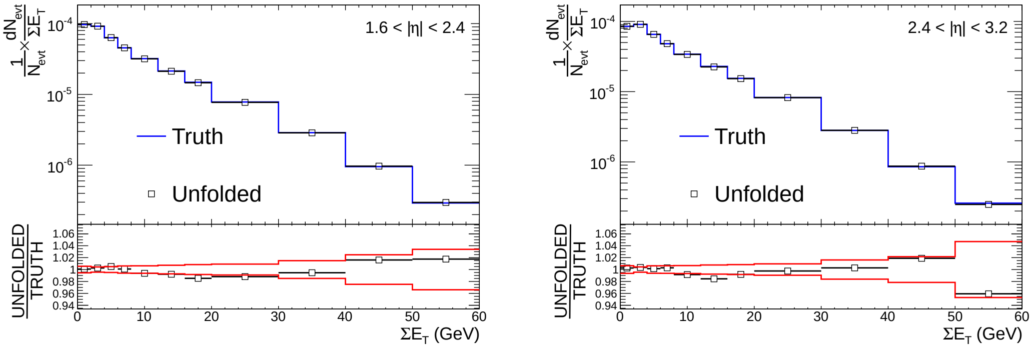

(c) $1.6 < |\eta| < 2.4$ **(d)** $2.4 < |\eta| < 3.2$

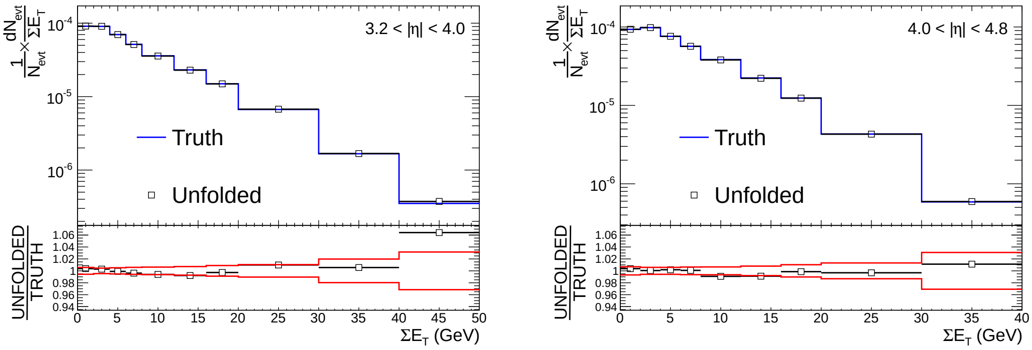

(e) $3.2 < |\eta| < 4.0$ **(f)** $4.0 < |\eta| < 4.8$

Figure 4.14: Minimum bias selection. `Pythia 6 AMBT1` reconstructed unfolded with a statistically independent `Pythia 6 AMBT1` unfolding matrix compared with `Pythia 6 AMBT1` truth. The red histogram in the ratio distribution shows the statistical error on the unfolded data, while the black histogram shows the degree of closure. The distributions are plotted in the following $|\eta|$ bins: (a) $0.0 < |\eta| < 0.8$; (b) $0.8 < |\eta| < 1.6$; (c) $1.6 < |\eta| < 2.4$; (d) $2.4 < |\eta| < 3.2$; (e) $3.2 < |\eta| < 4.0$; (b) $4.0 < |\eta| < 4.8$.

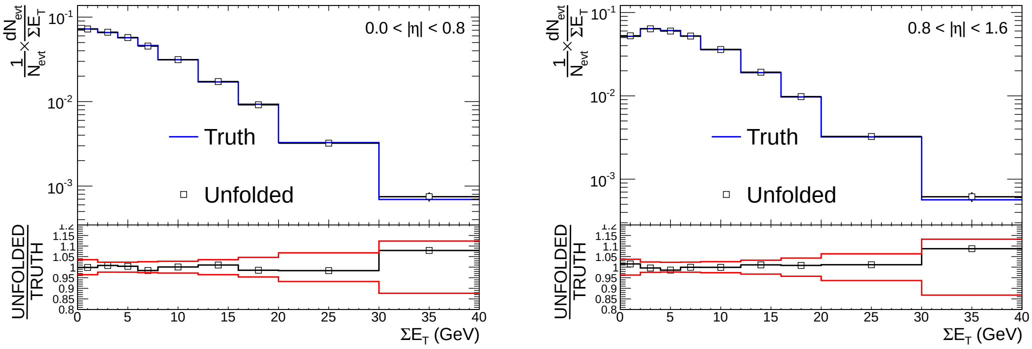

(a) $0.0 < |\eta| < 0.8$ **(b)** $0.8 < |\eta| < 1.6$

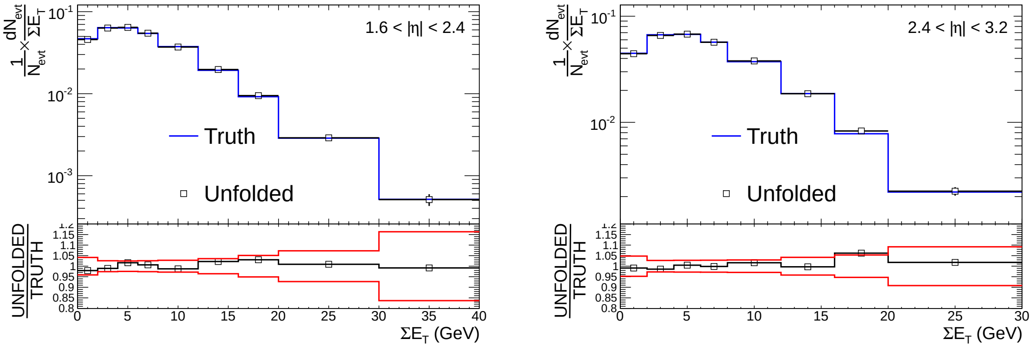

(c) $1.6 < |\eta| < 2.4$ **(d)** $2.4 < |\eta| < 3.2$

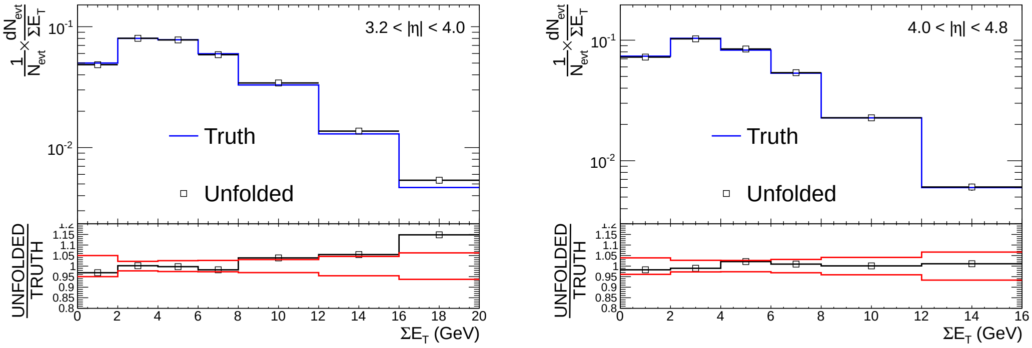

(e) $3.2 < |\eta| < 4.0$ **(f)** $4.0 < |\eta| < 4.8$

Figure 4.15: Di-jet selection. `Pythia 6 AMBT1` reconstructed unfolded with a statistically independent `Pythia 6 AMBT1` unfolding matrix compared with `Pythia 6 AMBT1` truth. The red histogram in the ratio distribution shows the statistical error on the unfolded data, while the black histogram shows the degree of closure. The distributions are plotted in the following $|\eta|$ bins: (a) 0.0 $< |\eta| <$ 0.8; (b) 0.8 $< |\eta| <$ 1.6; (c) 1.6 $< |\eta| <$ 2.4; (d) 2.4 $< |\eta| <$ 3.2; (e) 3.2 $< |\eta| <$ 4.0; (b) 4.0 $< |\eta| <$ 4.8.

`Pythia 6 AMBT1` sample is unfolded with a reweighted `Pythia 6 AMBT1` matrix and compared with the nominal `Pythia 6 AMBT1` truth, it should return complete closure.

However, as shown in Figure 4.16, biases of up to $\sim 35\%$ are observed in tests of this type with di-jet data. To investigate this, it was first noted that the di-jet sample contained many more (approximately a factor of 10) fake events than in the minimum bias sample. By setting the fake event weight equal to 1 — in effect, removing the effects of mis-modelling by replacing the fake distribution with a uniform distribution — the bias was reduced to at most 4% (Figure 4.17), indicating that the treatment of fake events was largely responsible for the non-closure. This confirmed the necessity of reweighting the MC to the data; if the unfolding were to be performed without reweighting, the choice of model (which dictates the shape of the fake event distribution) would introduce large biases immune to removal via successive iterations. Therefore, considering that the MCs' descriptions of the forward region are unconstrained by data, it was deemed instructive to improve them as best as possible by reweighting to real data before unfolding.

4.5.8 Physics model dependence

Whilst the reweighting and iterative procedures reduce the dependence of the unfolded distribution on the MC's modelling of the ΣE_T spectrum, it is possible that further dependencies on variables contributing to the ΣE_T exist. Ideally the aforementioned procedures would ensure closure when unfolding one MC with a smearing matrix filled with another MC; the detector simulation is the same for both, and iterations should reduce the dependency on a given model's ΣE_T spectrum. Figure 4.18 shows an example MC closure test in minimum bias data: here, `Pythia 6 DW` is unfolded with a `Pythia 6 AMBT1` unfolding matrix. The reasoning behind the choice of `Pythia 6 DW` is discussed shortly, but the same tests were performed using a variety of models, some of which — such as an older version of `H++`— are not included in further comparisons due to their being superseded by more recent versions. The residual model dependence is given by the non-closure, which ranges from 14% in the highest ΣE_T bin in the first $|\eta|$ bin to as large as 32% in the highest ΣE_T bin in the last $|\eta|$ bin. Ideally the unfolded result should agree within statistical error, which is at most 4%.

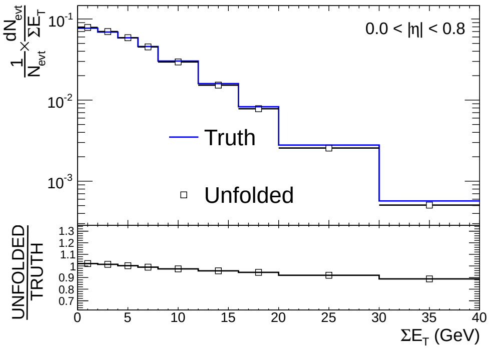

(a) $0.0 < |\eta| < 0.8$ **(b)** $0.8 < |\eta| < 1.6$

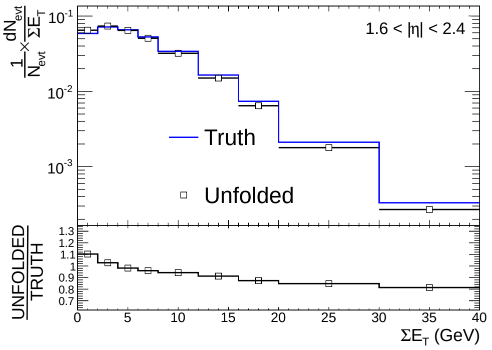

(c) $1.6 < |\eta| < 2.4$ **(d)** $2.4 < |\eta| < 3.2$

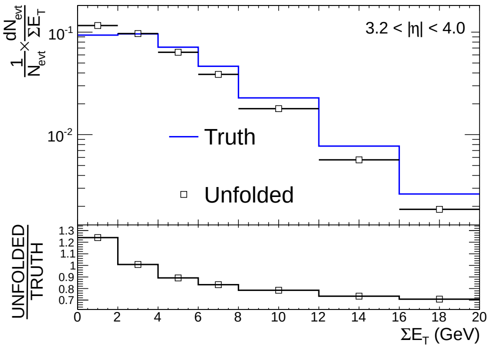

(e) $3.2 < |\eta| < 4.0$ **(f)** $4.0 < |\eta| < 4.8$

Figure 4.16: Di-jet selection. The nominal reconstructed `Pythia AMBT1` is unfolded with a reweighted `Pythia AMBT1` unfolding matrix and compared with `Pythia AMBT1` truth. The distributions are plotted in the following $|\eta|$ bins: (a) 0.0 $< |\eta| < 0.8$; (b) $0.8 < |\eta| < 1.6$; (c) $1.6 < |\eta| < 2.4$; (d) $2.4 < |\eta| < 3.2$; (e) $3.2 < |\eta| < 4.0$; (b) $4.0 < |\eta| < 4.8$.

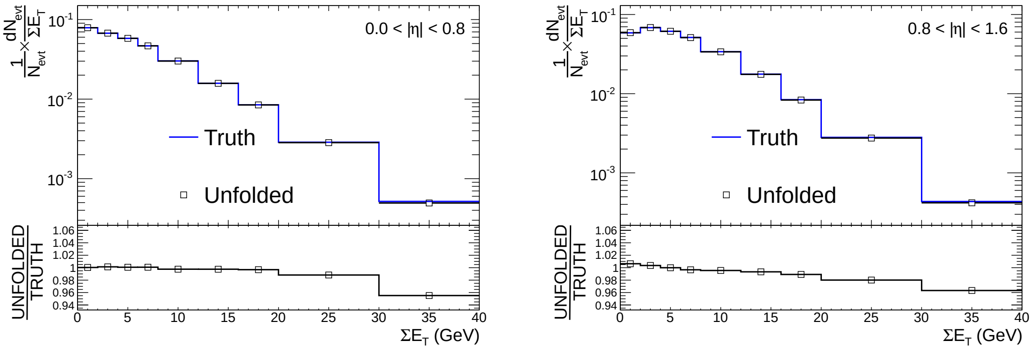

(a) $0.0 < |\eta| < 0.8$

(b) $0.8 < |\eta| < 1.6$

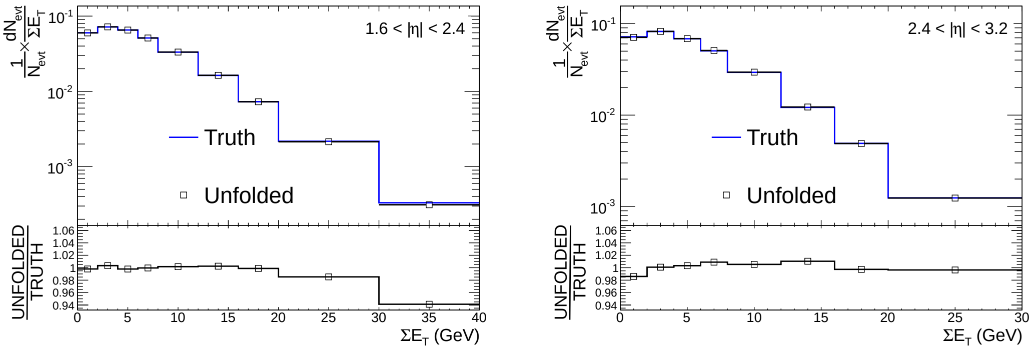

(c) $1.6 < |\eta| < 2.4$

(d) $2.4 < |\eta| < 3.2$

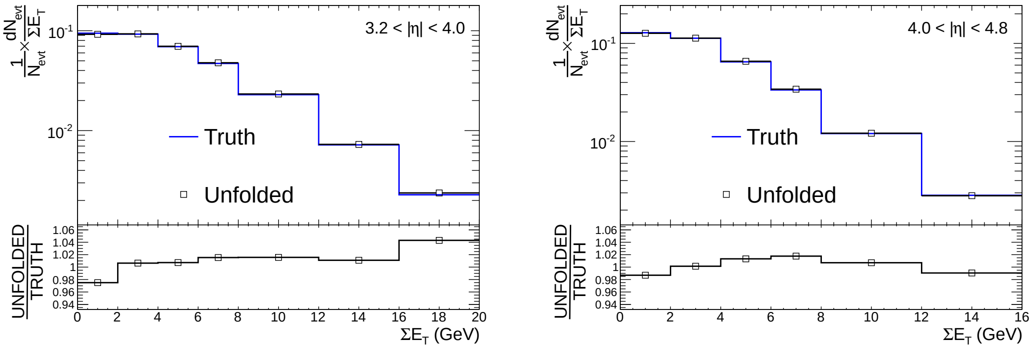

(e) $3.2 < |\eta| < 4.0$

(f) $4.0 < |\eta| < 4.8$

Figure 4.17: Di-jet selection. The nominal reconstructed `Pythia AMBT1` is unfolded with a reweighted `Pythia AMBT1` unfolding matrix and compared with `Pythia AMBT1` truth; fake event weights are set equal to 1. The distributions are plotted in the following $|\eta|$ bins: (a) $0.0 < |\eta| < 0.8$; (b) $0.8 < |\eta| < 1.6$; (c) $1.6 < |\eta| < 2.4$; (d) $2.4 < |\eta| < 3.2$; (e) $3.2 < |\eta| < 4.0$; (b) $4.0 < |\eta| < 4.8$.

This discrepancy can be reasoned in terms of the E_T of the topoClusters that contribute to the ΣE_T. Due to material interactions, low E_T topoClusters lose more energy before reaching the calorimeter, and thus their contribution to the ΣE_T requires a larger correction. For a given ΣE_T, one model might predict a large number of low E_T particles, and another a small number of high E_T particles, resulting in different detector responses. This feature is shown in Figure 4.19 for minimum bias data. Here the E_T-weighted $|E_T|$, normalised to the integral of the distribution, is plotted: this gives the fractional contribution of clusters of a given E_T to the sum over events of the ΣE_T. In the region $|\eta| < 2.4$ all the MC models agree with the data reasonably well. However, in the region $|\eta| > 2.4$ the data predict a softer E_T spectrum than the models, and their spread is quite large: `H++` and `Pythia 6 AMBT1` differ at the 20% level. The same distribution is plotted in Figure 4.20 for events with $\Sigma E_T > 15$ GeV, in order to assess the description of events with high ΣE_T. A similar relationship between `Pythia 6 AMBT1` and the data is observed; however, here `Pythia 6 DW` displays the largest deviation from the nominal model. The same tests are shown for di-jet data in Figure 4.21 and Figure 4.22. It is noted that `Pythia 6 AMBT1` is slightly softer than the data in the region $|\eta| < 3.2$, but agrees well in the forward region. The largest deviation from the nominal model is given by `H++ UE7-2`; the difference is even bigger than that between `Pythia 6 AMBT1` and data.

As a result of the distributions shown in Figures 4.18-4.22, and after conducting many combinations of closure tests similar to Figure 4.18 in both channels, `Pythia 6 DW` was used to gauge the model dependence in minimum bias, and `H++ UE7-2` for di-jet data. The values for the systematic uncertainty itself were derived by unfolding the data with these models and comparing to the data unfolded with `Pythia 6 AMBT1`, as discussed in Section 4.6.2.

Finally, Appendix A describes a study into how the model dependence varies as a function of various truth particle momentum cuts and potential cluster energy cuts. The nominal cuts (200 MeV for neutral particles and 500 MeV for charged particles) and maintaining no cluster energy cut were found to yield the smallest model dependence.

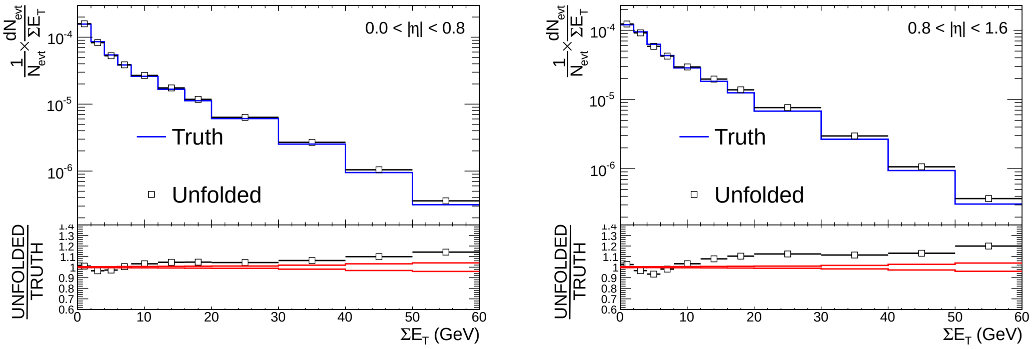

(a) $0.0 < |\eta| < 0.8$ **(b)** $0.8 < |\eta| < 1.6$

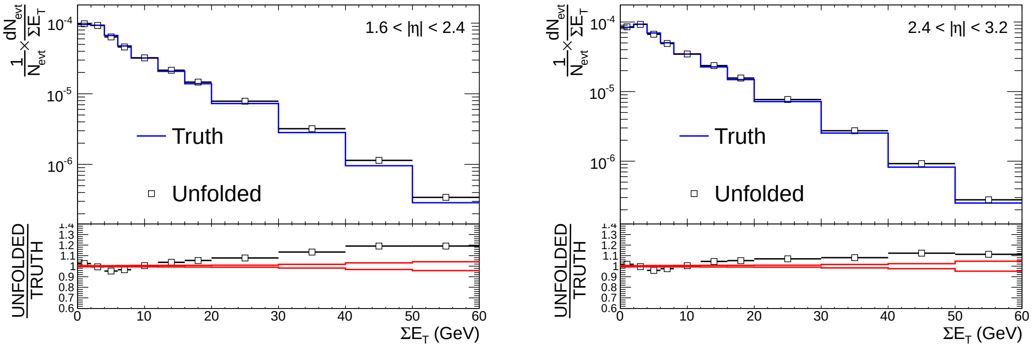

(c) $1.6 < |\eta| < 2.4$ **(d)** $2.4 < |\eta| < 3.2$

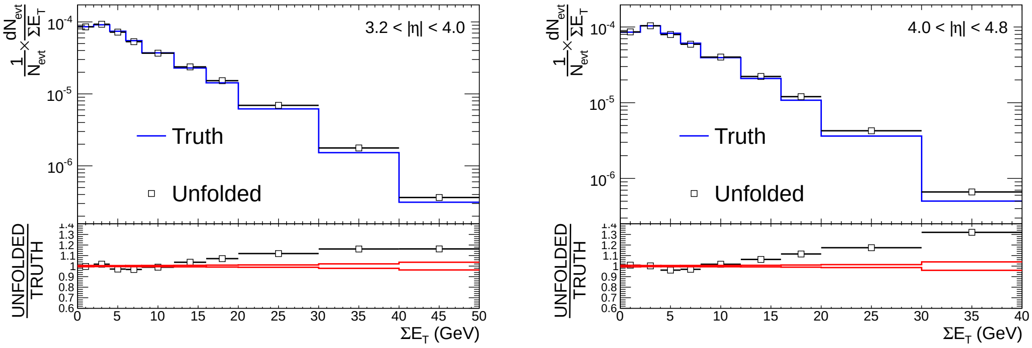

(e) $3.2 < |\eta| < 4.0$ **(f)** $4.0 < |\eta| < 4.8$

Figure 4.18: `Pythia 6 DW` reconstructed unfolded with a `Pythia 6 AMBT1` unfolding matrix compared with `Pythia 6 DW` truth, in minimum bias. The red histogram in the ratio distribution shows the statistical error on the unfolded data, while the black histogram shows the degree of model dependence. The distributions are plotted in the following $|\eta|$ bins: (a) $0.0 < |\eta| < 0.8$; (b) $0.8 < |\eta| < 1.6$; (c) $1.6 < |\eta| < 2.4$; (d) $2.4 < |\eta| < 3.2$; (e) $3.2 < |\eta| < 4.0$; (b) $4.0 < |\eta| < 4.8$.

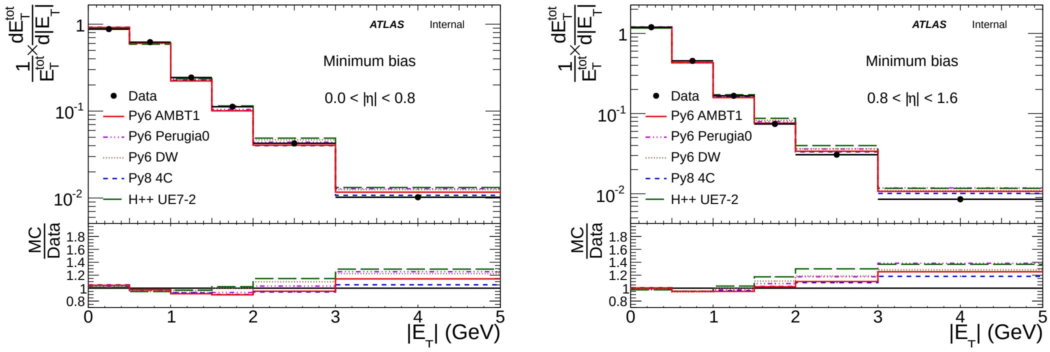

(a) $0.0 < |\eta| < 0.8$ **(b)** $0.8 < |\eta| < 1.6$

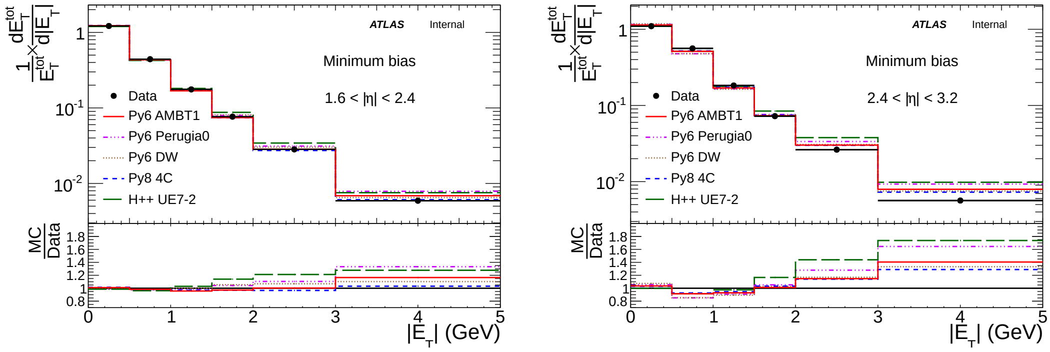

(c) $1.6 < |\eta| < 2.4$ **(d)** $2.4 < |\eta| < 3.2$

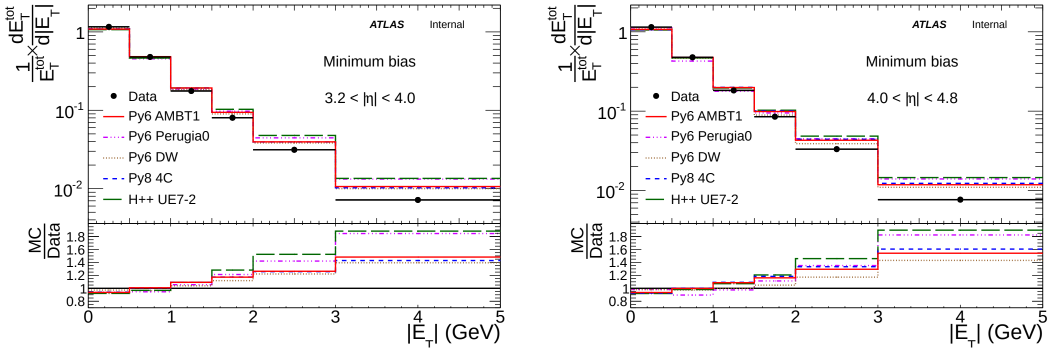

(e) $3.2 < |\eta| < 4.0$ **(f)** $4.0 < |\eta| < 4.8$

Figure 4.19: Distribution of $\frac{1}{E_T^{tot}} \times \frac{E_T^{tot}}{d|E_T|}$, where E_T^{tot} is the sum over events of the detector level ΣE_T, and E_T is the detector level cluster transverse energy in minimum bias in the following $|\eta|$ bins: (a) $0.0 < |\eta| < 0.8$; (b) $0.8 < |\eta| < 1.6$; (c) $1.6 < |\eta| < 2.4$; (d) $2.4 < |\eta| < 3.2$; (e) $3.2 < |\eta| < 4.0$; (b) $4.0 < |\eta| < 4.8$.

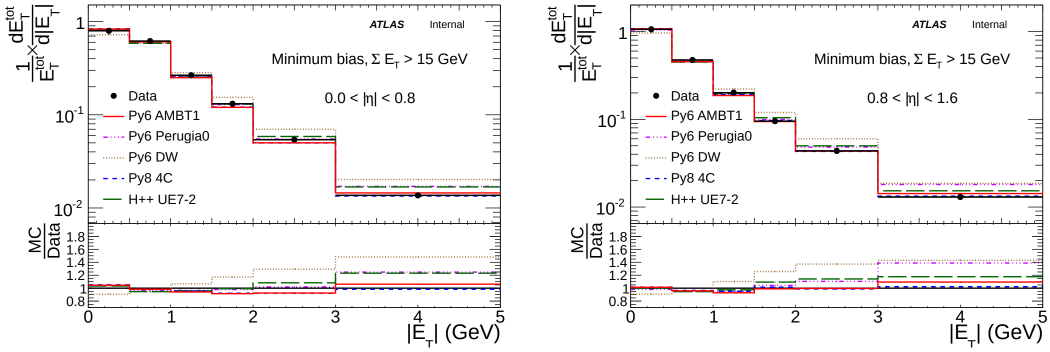

(a) $0.0 < |\eta| < 0.8$ **(b)** $0.8 < |\eta| < 1.6$

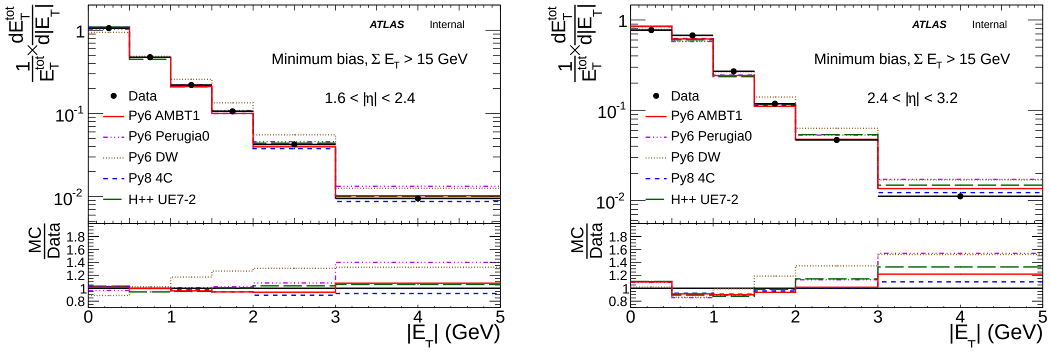

(c) $1.6 < |\eta| < 2.4$ **(d)** $2.4 < |\eta| < 3.2$

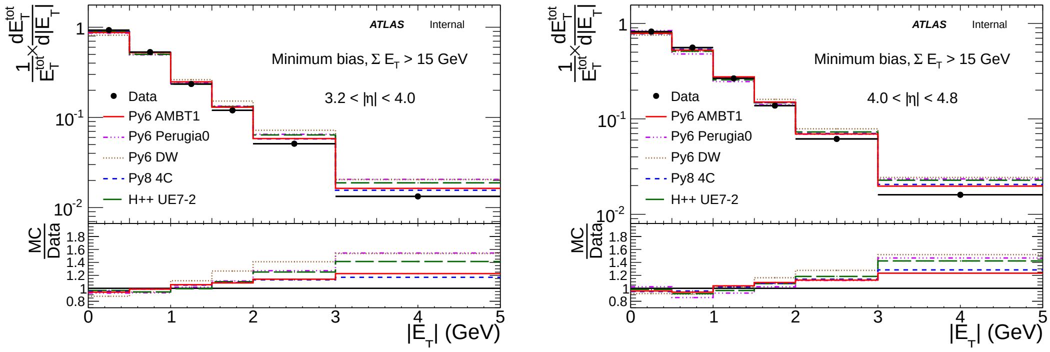

(e) $3.2 < |\eta| < 4.0$ **(f)** $4.0 < |\eta| < 4.8$

Figure 4.20: Distribution of $\frac{1}{E_T^{tot}} \times \frac{E_T^{tot}}{d|E_T|}$, where E_T^{tot} is the sum over events of the detector level ΣE_T, and E_T is the detector level cluster transverse energy in minimum bias with $\Sigma E_T > 15$ GeV, in the following $|\eta|$ bins: (a) 0.0 $< |\eta| < 0.8$; (b) $0.8 < |\eta| < 1.6$; (c) $1.6 < |\eta| < 2.4$; (d) $2.4 < |\eta| < 3.2$; (e) $3.2 < |\eta| < 4.0$; (b) $4.0 < |\eta| < 4.8$.

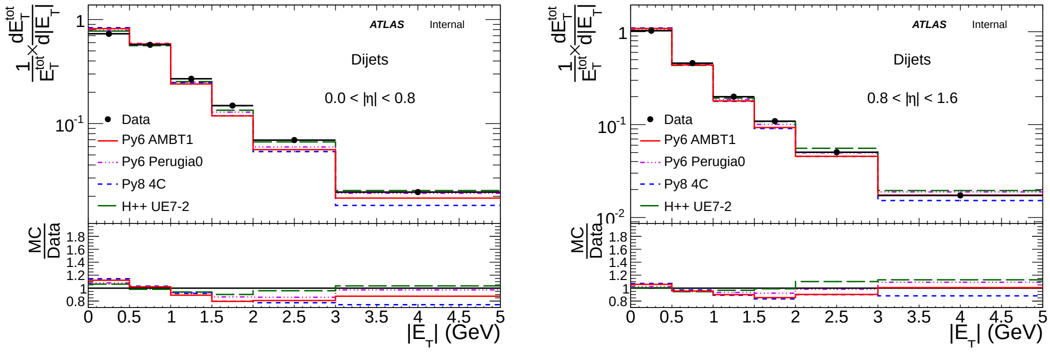

(a) $0.0 < |\eta| < 0.8$ **(b)** $0.8 < |\eta| < 1.6$

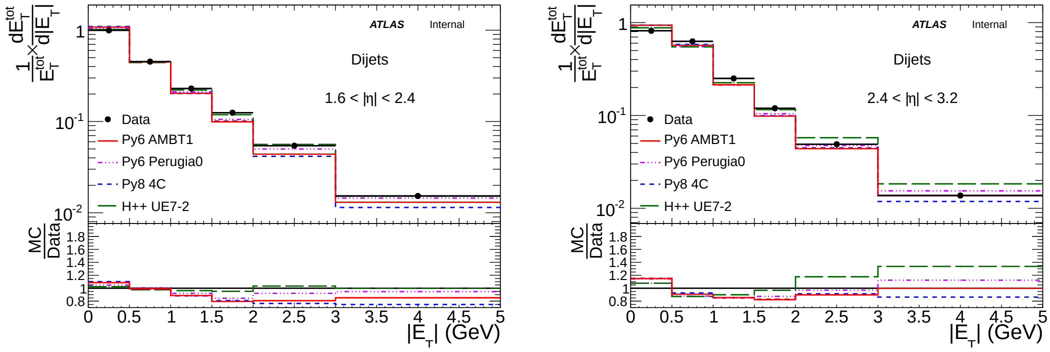

(c) $1.6 < |\eta| < 2.4$ **(d)** $2.4 < |\eta| < 3.2$

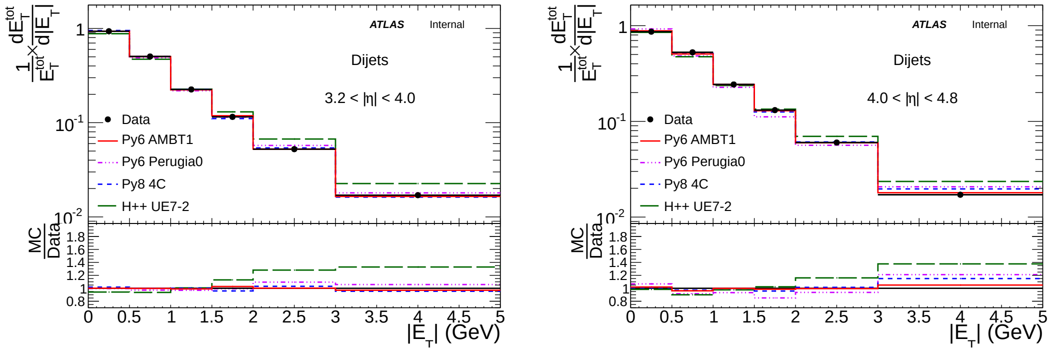

(e) $3.2 < |\eta| < 4.0$ **(f)** $4.0 < |\eta| < 4.8$

Figure 4.21: Distribution of $\frac{1}{E_T^{tot}} \times \frac{E_T^{tot}}{d|E_T|}$, where E_T^{tot} is the sum over events of the detector level ΣE_T, and E_T is the detector level cluster transverse energy in di-jet events in the following $|\eta|$ bins: (a) $0.0 < |\eta| < 0.8$; (b) $0.8 < |\eta| < 1.6$; (c) $1.6 < |\eta| < 2.4$; (d) $2.4 < |\eta| < 3.2$; (e) $3.2 < |\eta| < 4.0$; (b) $4.0 < |\eta| < 4.8$.

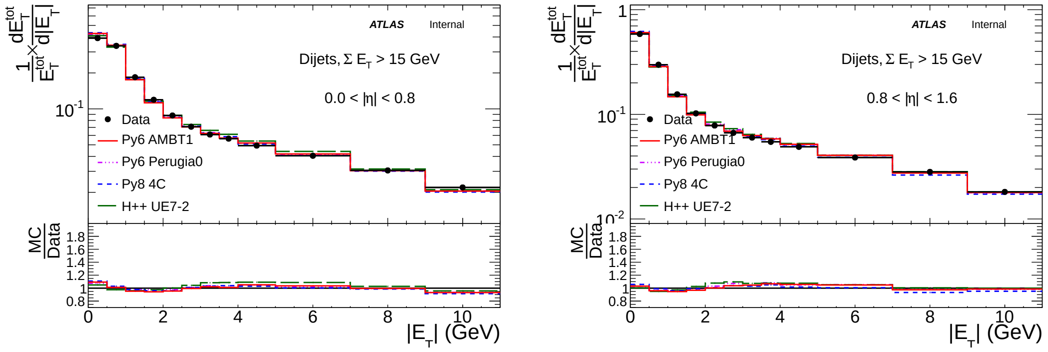

(a) $0.0 < |\eta| < 0.8$ (b) $0.8 < |\eta| < 1.6$

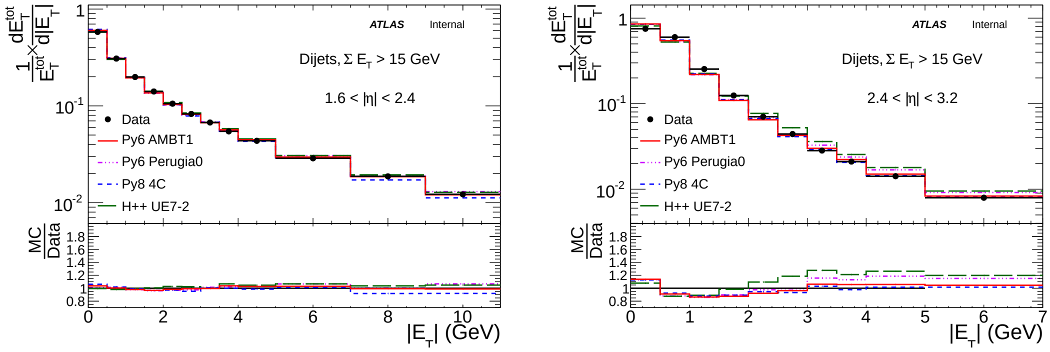

(c) $1.6 < |\eta| < 2.4$ (d) $2.4 < |\eta| < 3.2$

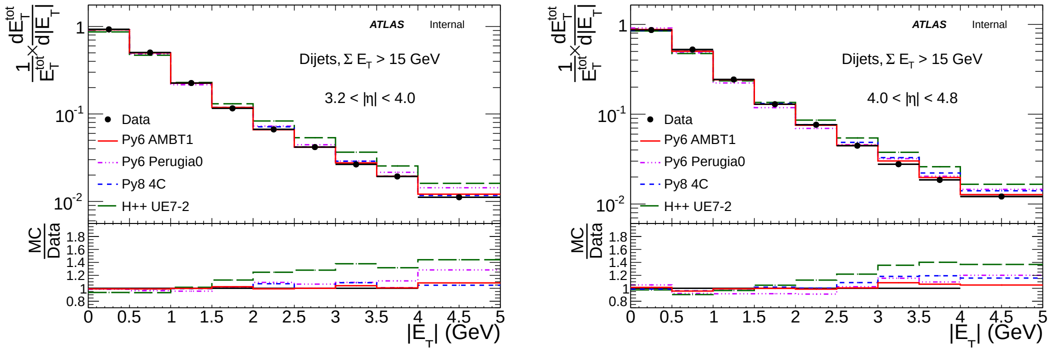

(e) $3.2 < |\eta| < 4.0$ (f) $4.0 < |\eta| < 4.8$

Figure 4.22: Distribution of $\frac{1}{E_T^{tot}} \times \frac{E_T^{tot}}{d|E_T|}$, where E_T^{tot} is the sum over events of the detector level ΣE_T, and E_T is the detector level cluster transverse energy in di-jet events with $\Sigma E_T > 15$ GeV, in the following $|\eta|$ bins: (a) $0.0 < |\eta| < 0.8$; (b) $0.8 < |\eta| < 1.6$; (c) $1.6 < |\eta| < 2.4$; (d) $2.4 < |\eta| < 3.2$; (e) $3.2 < |\eta| < 4.0$; (b) $4.0 < |\eta| < 4.8$.

4.5.9 Statistical error propagation

Before unfolding is performed, the statistical uncertainty on a given $|\eta|$ bin in an E_T^{flow} distribution is calculated as the error on the mean of its corresponding ΣE_T distribution. After unfolding is performed, the same uncertainty is dependent on the unfolding parameters.

The statistical errors on the MC and data ΣE_T distributions are propagated through the unfolding process according to the following error matrix:

$$\frac{\partial \hat{n}(C_i)}{\partial n(D_j)} = S_{ij} + \sum_{k=1}^{n_D} S_{ik} n(D_k) \left(\frac{1}{P(T_i)} \frac{\partial P(T_i)}{\partial n(D_j)} - \sum_{l=1}^{n_C} \frac{\epsilon_l}{P(T_l)} \frac{\partial P(T_l)}{\partial n(D_j))} S_{lk} \right) \tag{4.12}$$

Here, $\hat{n}(C_i)$ is the corrected data distribution, S_{ij} the smearing matrix, n_D (n_C) are the number of uncorrected (corrected) events, $P(T_i)$ the prior distribution, and $n(D_j)$ the uncorrected data distribution. As described in Section 4.5.6, ϵ_l represent efficiencies used to treat missed and fake events. Since the second part of the expression contains partial derivatives, it vanishes if only a single iteration is applied and the error is just given in terms of the smearing matrix ($\frac{\partial \hat{n}(C_i)}{\partial n(D_j)} = S_{ij}$). Notably, the error matrix depends on $\frac{\partial P(T_i)}{\partial n(D_j)}$, which is $\frac{\partial \hat{n}(C_i)}{\partial n(D_j)}$ from the previous iteration (as expected, the prior is replaced by the unfolded distribution). As such, this matrix takes into account the evolution of the statistical error with the number of iterations.

The error matrix is used to obtain the covariance matrix on the unfolded distribution, $V(\hat{n}(C_k), \hat{n}(C_l))$, via the following expression:

$$V(\hat{n}(C_k), \hat{n}(C_l)) = \sum_{i,j=1}^{n_D} \frac{\partial \hat{n}(C_k)}{\partial n(D_i)} V(n(D_i), n(D_j)) \frac{\partial \hat{n}(C_l)}{\partial n(D_j)} \tag{4.13}$$

Where $V(n(D_i), n(D_j))$ is the covariance matrix of the uncorrected distribution. Example covariance matrices are given in Figure 4.23 for the minimum bias sample. Strong positive correlations are noted in all $|\eta|$ bins, as may be expected. The diagonal of a covariance matrix is the variance, or the squared statistical error; from these matrices, the final unfolded statistical uncertainty can therefore be extracted. These errors are displayed on all distributions in Section 4.7.

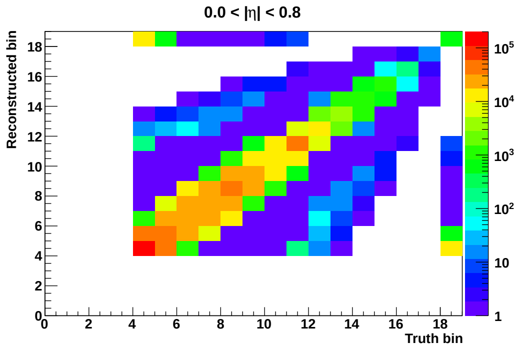

(a) $0.0 < |\eta| < 0.8$ **(b)** $0.8 < |\eta| < 1.6$

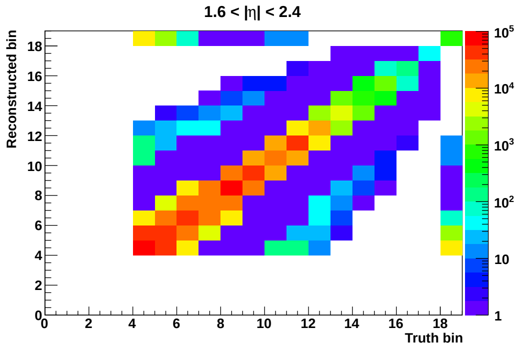

(c) $1.6 < |\eta| < 2.4$ **(d)** $2.4 < |\eta| < 3.2$

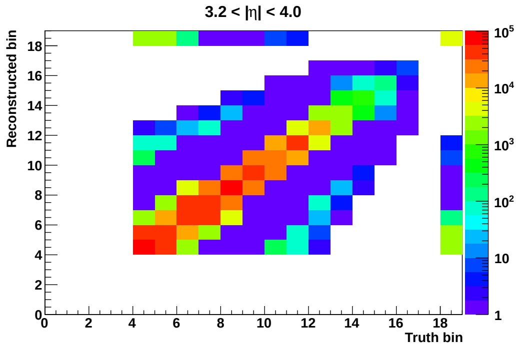

(e) $3.2 < |\eta| < 4.0$ **(f)** $4.0 < |\eta| < 4.8$

Figure 4.23: Minimum bias covariance matrices, after 2 iterations, in the following $|\eta|$ bins: (a) $0.0 < |\eta| < 0.8$; (b) $0.8 < |\eta| < 1.6$; (c) $1.6 < |\eta| < 2.4$; (d) $2.4 < |\eta| < 3.2$; (e) $3.2 < |\eta| < 4.0$; (b) $4.0 < |\eta| < 4.8$. Note that the axes correspond to the bin number of the unfolded distribution and not the units of the input variable. The magnitude in each bin, denoted by the logarithmic scale rainbow bar, indicates the (non-physical) size of the covariance.

4.6 Systematic uncertainties

The treatment of the statistical uncertainty (Section 4.5.9) and of one of the main sources of systematic uncertainty — the model dependence from unfolding (Section 4.5.8) — have already been discussed. This section details the remaining two dominant sources of systematic uncertainty common to both the inclusive pp and di-jet analyses: the MC's simulation of the energy response to low energy particles, and the MC's description of the ATLAS detector material. An additional source of systematic uncertainty, related to the measurement of jet energies and hence relevant to the di-jet analysis, is also described.

The following possible sources of systematic uncertainty were found to be negligibly small ($\mathcal{O}(0.1\%)$): pile-up, cluster energy resolution, contributions from noise and beam-induced backgrounds, simulation of the trigger selection, simulation of the primary vertex position, and simulation of the position of the FCal.

4.6.1 Calorimeter energy response

To improve its description of the simulated detector response to low energy particles, topoClusters in the MC used to unfolding the data are scaled by a factor $1+\alpha$, which depends on the topoCluster η (described in Section 4.4.2, with the scaling factors shown in Table 4.3). The systematic uncertainties associated with measuring α — calculated, for example, by varying the π^0 fit range and the background shape — are used to determine the systematic uncertainty of the MC's response to EM particles.

The uncertainty on the response to hadronic particles is determined separately for particles in the inner detector (taken here as $|\eta| < 2.4$), where the tracking information can be used to cross-check calorimeter measurements, and for particles in the calorimeters outside the inner detector. In the former case, a study of the ratio of the inner detector track measurement to the calorimeter energy measurement of isolated charged pions [50] is used. The uncertainty is calculated by taking the difference between data and MC in p and η bins: it is found to be 3.5% for $|\eta| < 0.8$ and 5% for $0.8 < |\eta| < 2.4$. For $|\eta| > 2.4$, the uncertainty is determined from the difference between data and MC in test-beam studies of charged pions [51]. This yields a one-sided uncertainty for hadrons of +5% for $2.5 < |\eta| < 3.2$ and +9% in the remaining η-space ($3.2 < |\eta| < 4.8$).

Finally, an average of the EM and hadronic uncertainties is calculated according to `Pythia 6 AMBT1`'s prediction of the relative contribution of the two particle types to the ΣE_T (Figure 4.24a). This combined error represents a 1σ deviation from the standard scaling factor α. The final error is calculated by scaling all topoClusters by $\pm 1\sigma$, unfolding each ΣE_T distribution, and comparing to the nominal unfolded value. This is shown in terms of the E_T^{flow} in Figure 4.24b.

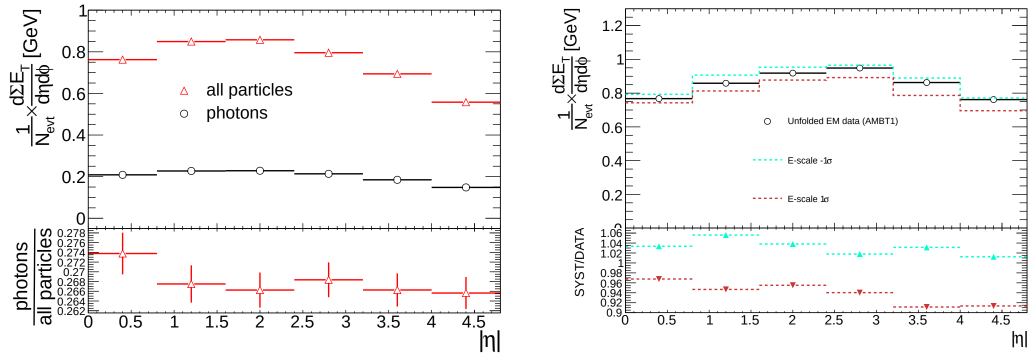

(a) Minimum bias

(b) Minimum bias

Figure 4.24: Figure (a) displays the relative contributions to the E_T^{flow} from EM and hadronic particles, according to `Pythia 6 AMBT1`. Figure (b) shows the nominal unfolded data E_T^{flow} (black) compared to E_T^{flow} distributions where the topoClusters are scaled according to the systematic errors discussed in the text; the ratio distribution gives the final systematic error on the energy response. Both figures show minimum bias data.

4.6.2 Model dependence

The model dependent systematic uncertainty is determined by comparing the results of unfolding the data with the nominal MC sample (`Pythia 6 AMBT1`) with the results from unfolding with the MC tune expected to return the largest discrepancy, according to closure tests and spectra comparisons (Section 4.5.8). Such tests are shown in terms of the E_T^{flow} for minimum bias (Figure 4.25a) and di-jet data (Figure 4.25b), with the ratio giving the fractional deviation from the nominal unfolding. In minimum bias both `H++ UE7-2` and `Pythia 6 DW` are compared to the nominal in order to confirm that, on average, `Pythia 6 DW` returns the largest deviation. In di-jet data only `H++ UE7-2`, which produced the largest model dependence in the aforementioned tests, is considered.

Ratio distributions equivalent to the E_T^{flow} ratios, but in terms of ΣE_T instead, are shown in Figures 4.26 and 4.27 for minimum bias and di-jet data, respectively. The model dependent systematic uncertainty in each bin is equal to the deviation from the nominal, and the final result is symmetrised to account for the possibility that the bias operates in a the opposite direction.

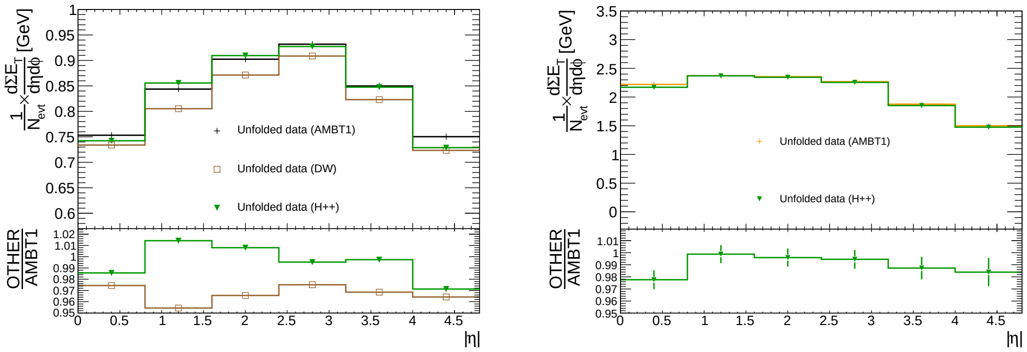

(a) Minimum bias **(b)** Di-jets

Figure 4.25: Figure (a): minimum bias data E_T^{flow}, unfolded using `Pythia 6 AMBT1`, `DW` and `H++ UE7-2` separately. Figure (b): di-jet data E_T^{flow}, unfolded using `Pythia 6 AMBT1` and `H++ UE7-2` separately.

4.6.3 Detector material

Since particles contributing to the ΣE_T lose energy by material interactions, it is important that the MC used in corrections provides an accurate description of not only the detecting medium, but also the material upstream of the calorimeters.

To this end, comparisons are made between the nominal `Pythia 6 AMBT1` sample and an "extra material" sample with exactly the same physics model but a different simulation of the ATLAS detector. A similar extra material sample is described in section 3 of reference [52]; specifics of the sample used here are listed below.

- In the inner detector:
  - an extra 5% of material added to the entire inner detector
  - an extra 20% of material added to the pixel and SCT services

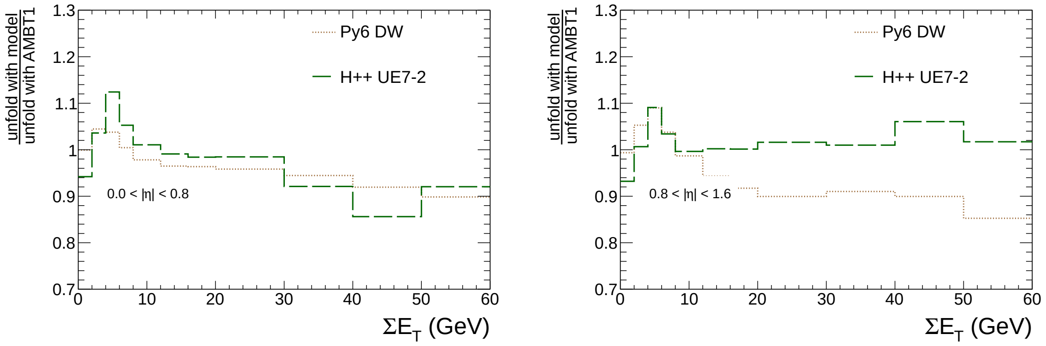

(a) $0.0 < |\eta| < 0.8$ **(b)** $0.8 < |\eta| < 1.6$

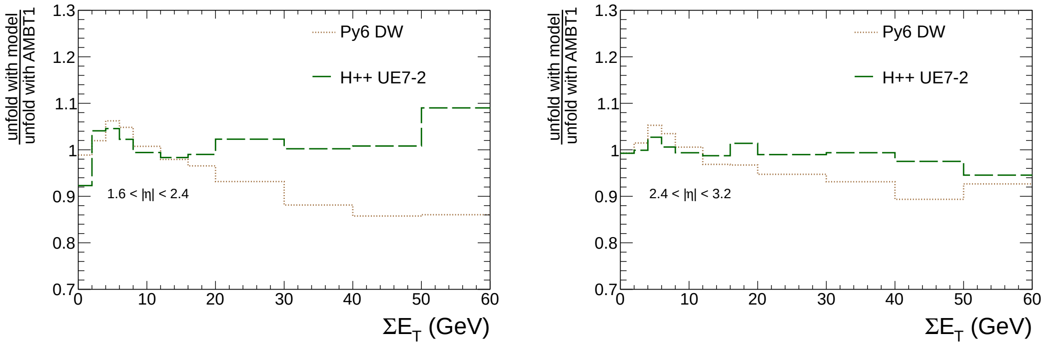

(c) $1.6 < |\eta| < 2.4$ **(d)** $2.4 < |\eta| < 3.2$

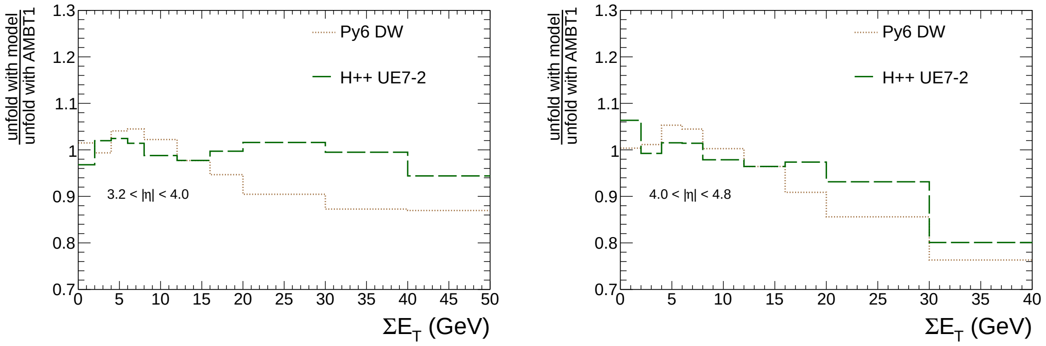

(e) $3.2 < |\eta| < 4.0$ **(f)** $4.0 < |\eta| < 4.8$

Figure 4.26: Ratio of minimum bias data ΣE_T distributions, unfolded using `Pythia 6 DW` and `H++ UE7-2` separately, to the same distribution unfolded using `Pythia 6 AMBT1`, in the following $|\eta|$ bins: (a) $0.0 < |\eta| < 0.8$; (b) $0.8 < |\eta| < 1.6$; (c) $1.6 < |\eta| < 2.4$; (d) $2.4 < |\eta| < 3.2$; (e) $3.2 < |\eta| < 4.0$; (b) $4.0 < |\eta| < 4.8$.

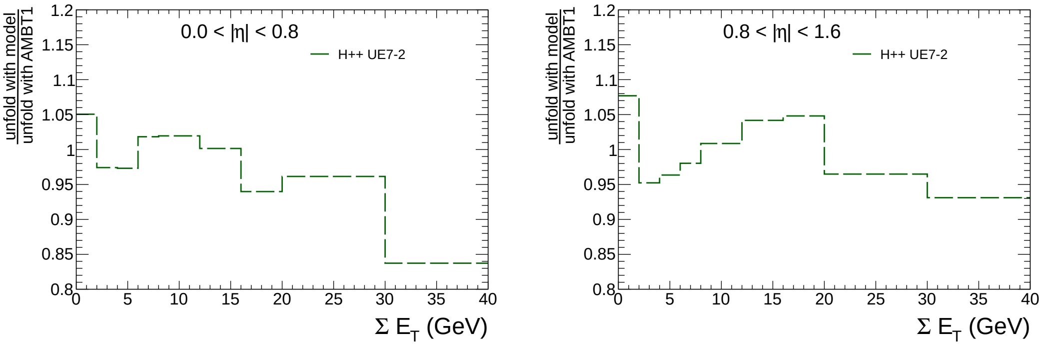

(a) $0.0 < |\eta| < 0.8$ **(b)** $0.8 < |\eta| < 1.6$

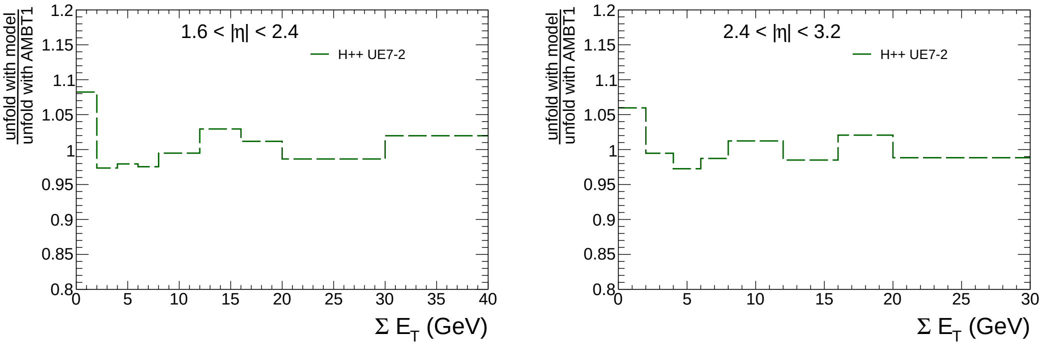

(c) $1.6 < |\eta| < 2.4$ **(d)** $2.4 < |\eta| < 3.2$

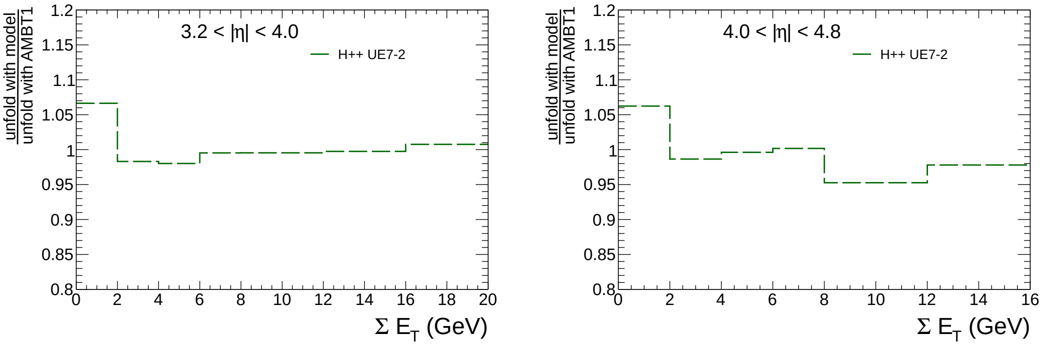

(e) $3.2 < |\eta| < 4.0$ **(f)** $4.0 < |\eta| < 4.8$

Figure 4.27: Ratio of di-jet data ΣE_T distributions unfolded using `H++ UE7-2` to the same distribution unfolded using `Pythia 6 AMBT1`, in the following $|\eta|$ bins: (a) $0.0 < |\eta| < 0.8$; (b) $0.8 < |\eta| < 1.6$; (c) $1.6 < |\eta| < 2.4$; (d) $2.4 < |\eta| < 3.2$; (e) $3.2 < |\eta| < 4.0$; (b) $4.0 < |\eta| < 4.8$.

  - $0.15X_0$ added to the end of the SCT/TRT endcap, and the inner detector endplate

- In the central calorimeter services:
  - $\dfrac{0.1}{sin(\theta)}X_0$ added in the barrel cryostat before the calorimeter
  - $\dfrac{0.05}{sin(\theta)}X_0$ added between the barrel pre-sampler and strips
  - an increase in the density of material in the endcap crack ($1.475 < |\eta| < 1.8$)
- In the forward region:
  - an increased thickness in one tube of the cryocylinders
  - a change of density in the pump material

Here X_0 is the usual radiation length for electromagnetic particles. Figure 4.28 compares the E_T^{flow} produced from the nominal and extra material samples, separately for the minimum bias and di-jet data sets. The resulting uncertainty depends on the $|\eta|$ region — though generally at the level of 2—4%, it increases up to 6% in the regions where calorimeter sub-systems overlap. This uncertainty is symmetrised to account for the possibility that the MC simulation either under or overestimates the amount of material.

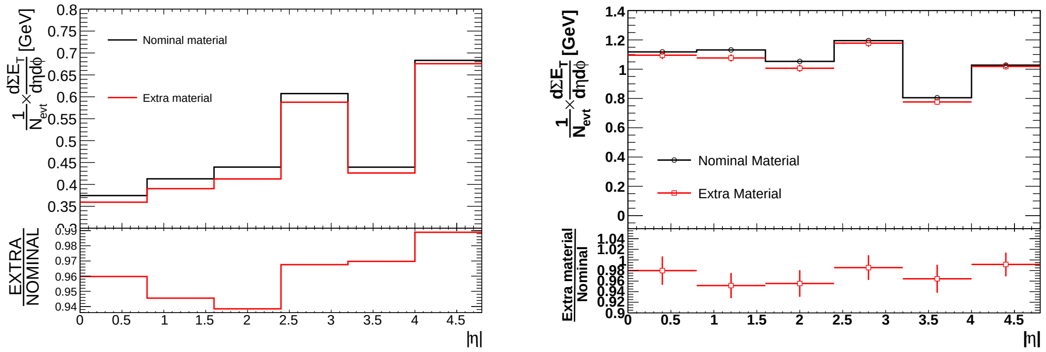

(a) Minimum bias **(b)** Di-jets

Figure 4.28: Distributions comparing the nominal `Pythia 6 AMBT1` reconstructed E_T^{flow} with the extra material `Pythia 6 AMBT1` reconstructed E_T^{flow}, in (a) minimum bias and (b) di-jet data.

4.6.4 Jet energy scale

The jet energy scale (JES) provides a systematic uncertainty on the measured jet energy, detailed calculations of which have been performed with the ATLAS detector [53]. Similar to the calibration method discussed in Section 4.4.4, it applies a correction to the raw jet energy. Therefore, an incorrect JES can alter the number of events passing the requirement that two jets with $E_T > 20$ GeV are present. The same is not true at the particle level, for which no JES is applicable; as such, it will not be accounted for by the unfolding. The effect of an incorrect JES is tested by performing the unfolding with the jet E_T shifted up and down by an $\eta-$ and E_T-dependent uncertainty function (described in reference [54]), compared with the nominal value. In the E_T^{flow} it is found to be 1.6% in the most central bin ($|\eta| < 0.8$), decreasing to 0.13% in the most forward bin. In the ΣE_T the effect is almost negligible, and is ignored altogether for $|\eta| > 2.4$.

4.7 Results

The final unfolded E_T^{flow} distributions are shown in Figures 4.29a and 4.29b. The statistical and systematic errors, combined in quadrature, are denoted by the green band; the systematic errors are always larger than the statistical, of the order $\mathcal{O}(10)$. In the minimum bias data a convexed distribution is observed — this is due to the truth p cuts, which remove relatively more particles from the central than forward region, where particles have a generally higher p. This effect is not as explicit in the di-jet data, which show a steadily falling distribution outside the most central $|\eta|$ bin. According to `Pythia 6 AMBT1`, the truth p cuts remove $\sim 18\%$ of events; in the equivalent $|\eta|$ bin in minimum bias, it is $\sim 25\%$. The difference here is due to the accepted di-jet events having a higher mean particle p, since the selection criteria biases towards small impact-parameter ("head-on") pp collisions and hence a harder scatter.

Comparisons with specific tunes of the models described in Section 2.7 are made. In the minimum bias distribution, both `Pythia 6 AMBT1` and `Pythia 6 AUET2B:CTEQ6L1` predict the data very well in the first two $|\eta|$ bins, and within error in the third. However, they fair less well for $|\eta| > 2.4$, with the prediction falling lower by at least an additional error sigma. This can be expected, since both these tunes were constrained by LHC data in the central region only. Conversely, `H++ UE7-2` and `Pythia 8 4C` (which is also tuned to early ATLAS minimum bias data) over-predict in the central region, but achieve a better description in the forward region. It is worth noting, however, that both models predict a larger E_T^{flow} overall, and as such neither provides a reliable description of the relative central-forward activity. Interestingly, `EPOS` delivers the best overall description; in particular, it is closest to the data in the most forward $|\eta|$ bin. In the central region at least, its success can be attributed to its having been tuned to LHC minimum bias data. Finally, despite being an older tune, `Pythia 6 DW` provides a reasonable description of the $|\eta|$ dependence; however, it significantly under-predicts the overall activity.

In the forward region, a similar relationship between data and MC is observed in the di-jet distribution as with the minimum bias: all models tend to under-predict the degree of activity. Here, however, only `Pythia 6 DW` lands within error (in the most forward two $|\eta|$ bins); `EPOS` now performs worst of all, most likely because it has never been tuned to underlying event data. The `Pythia 6 AUET2B:CTEQ6L1`

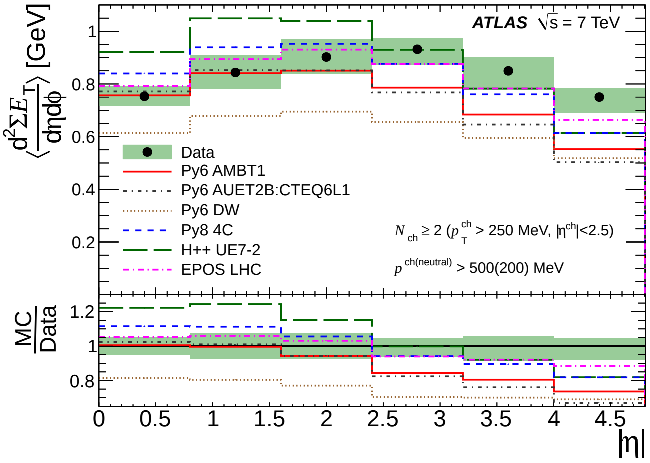

(a) Minimum bias

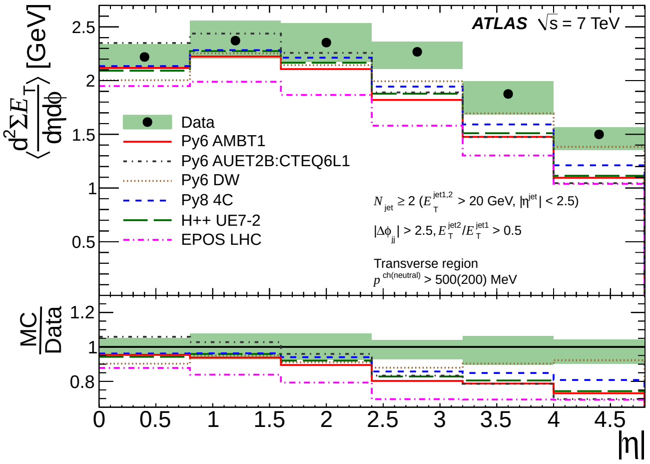

(b) Di-jets

Figure 4.29: Unfolded E_T^{flow} distribution compared to various MC models and tunes for (a) the minimum bias selection and (b) the di-jet selection in the transverse region. The filled band represents the total uncertainty on the unfolded data.

does feature tuning to ATLAS underlying event data — naïvely, one would expect it to provide the best description. This is not the case, however, with `Pythia 8 4C` performing better on average over all $|\eta|$.

The ratio of the minimum bias and di-jet results is shown in Figure 4.30. All systematic uncertainties except the physics model dependence and the jet energy scale are taken as correlated between the two distributions, and hence partially cancel in the ratio. In part, the ratio is > 1 in every $|\eta|$ bin because di-jet events, on average, contain higher p particles. However, the truth p cuts are not the whole story — removing them (shown in dark, dashed orange and denoted “no p cuts”) does not result in a flat ratio. The additional contribution to the di-jet data could originate from particles associated with the hard-scatter phase-space leaking into the transverse region.

Generally, both `Pythia 6 AMBT1` and `AUET2B:CTEQ6L1` predict the drop-off with $|\eta|$ most accurately. The remaining models bracket the data.

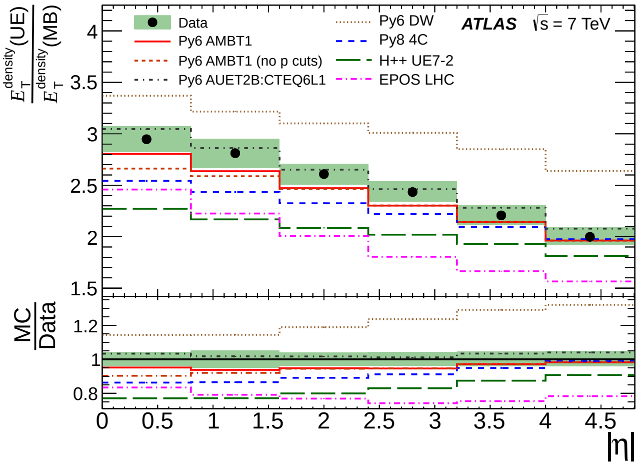

Figure 4.30: Unfolded E_T^{flow} distribution in the di-jet data transverse region divided by that in the minimum bias data, compared to various MC models and tunes. The filled band represents the total uncertainty on the unfolded data.

The final unfolded ΣE_T distributions are shown in Figures 4.31 and 4.32 for minimum bias and di-jet data, respectively. In both cases the data show a harder (higher mean) ΣE_T spectrum than the MC as the measurement moves from central to forward $|\eta|$. A broader distribution is observed in the data for $|\eta| < 3.2$ than in the forward region, implying that central events display more event-by-event variation in their ΣE_T. This feature is predicted by the various MC models and tunes; however, again, the overall description in the forward region is poor. The exception here is `Pythia 6 DW` in the di-jet distributions, which provides the best agreement overall, even describing the higher mean ΣE_T peak in the forward region. This improved description may be partially due to `DW` being a result of tuning to Tevatron underlying event data. Again, in the minimum bias data, `Pythia 6 AMBT1` describes the central distributions best.

4.7.1 Diffractive variations

In order to probe the dependency of the E_T^{flow} on the relative fractions of diffractive contributions, Figure 4.33 compares the unfolded minimum bias data to `Pythia 8 4C` with the default diffractive cross-sections (50.9 mb, 12.4 mb and 8.1 mb for non-diffractive, single-diffractive and double-diffractive processes, respectively), and to separate predictions by the same model with the diffractive components from the nominal sample either weighted by two or by a half, effectively doubling or halving the single- and double-diffractive contributions. Since diffractive events contain less activity than non-diffractive events, the observation that halving the diffractive component increases the E_T^{flow}— and vice-versa — is expected. However, the $|\eta|-$dependence is seen to be independent of the relative diffractive fractions; as such, it is concluded that variations in diffraction do not significantly effect the E_T^{flow} shape.

4.7.2 PDF variations

As discussed in Section 2.4.2, the choice of PDF used to model the non-perturbative component of the QCD cross-section can alter a given MC's prediction of the overall activity and $|\eta|-$dependence. Furthermore, it is necessary to constrain certain choices in the construction of a PDF to data.

To this end, Figure 4.34 shows the unfolded minimum bias and di-jet data compared to a group of `Pythia 8 A2` tunes. Here, the tunes are built on two PDF sets — `MSTW2008LO` and `CTEQ6L1`. First, the two tunes are compared directly; it is observed, in both datasets, that tuning parameters to `MSTW2008LO` (dashed blue) increases the overall activity relative to `CTEQ6L1` (solid green). Next, the PDF sets are compared directly by keeping the `CTEQ6L1` tune parameters constant, but

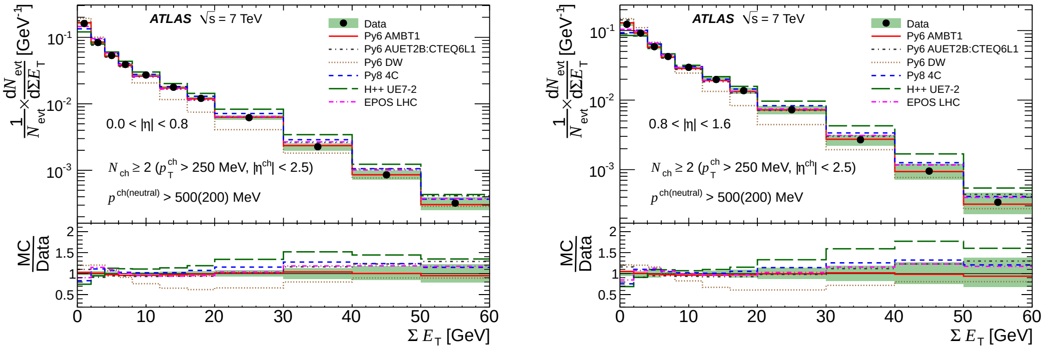

(a) $0.0 < |\eta| < 0.8$ **(b)** $0.8 < |\eta| < 1.6$

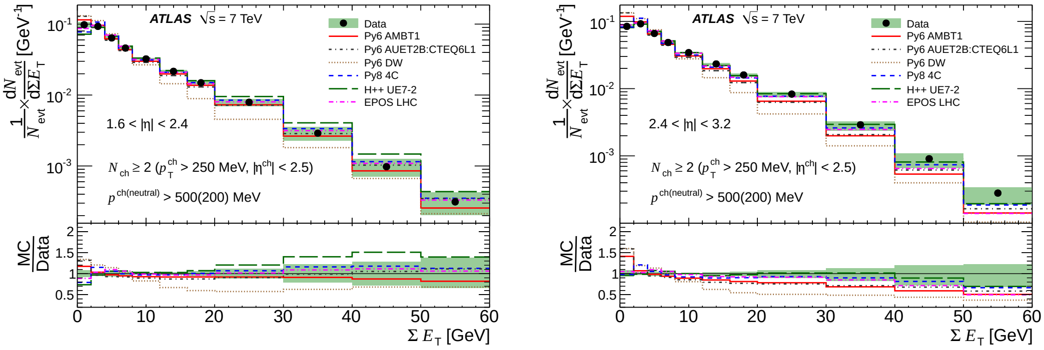

(c) $1.6 < |\eta| < 2.4$ **(d)** $2.4 < |\eta| < 3.2$

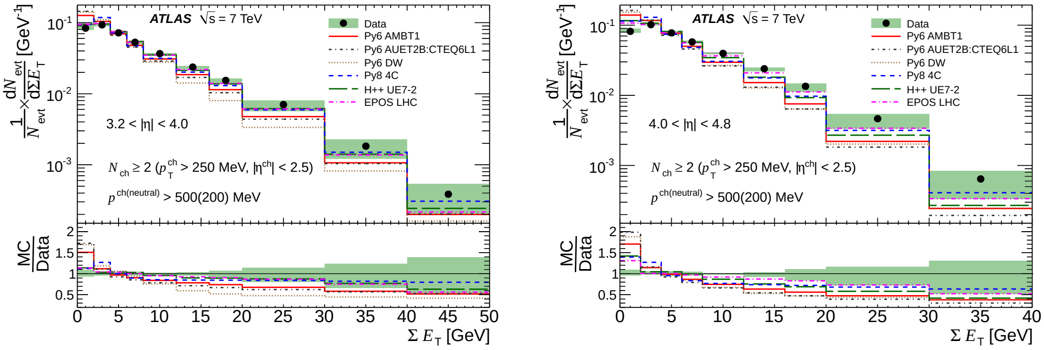

(e) $3.2 < |\eta| < 4.0$ **(f)** $4.0 < |\eta| < 4.8$

Figure 4.31: Unfolded ΣE_T distributions compared to various MC models and tunes for the minimum bias selection in the transverse region in the following $|\eta|$ regions: (a) $0.0 < |\eta| < 0.8$, (b) $0.8 < |\eta| < 1.6$, (c) $1.6 < |\eta| < 2.4$, (d) $2.4 < |\eta| < 3.2$, (e) $3.2 < |\eta| < 4.0$ and (f) $4.0 < |\eta| < 4.8$. The filled band in each plot represents the total uncertainty on the unfolded data.

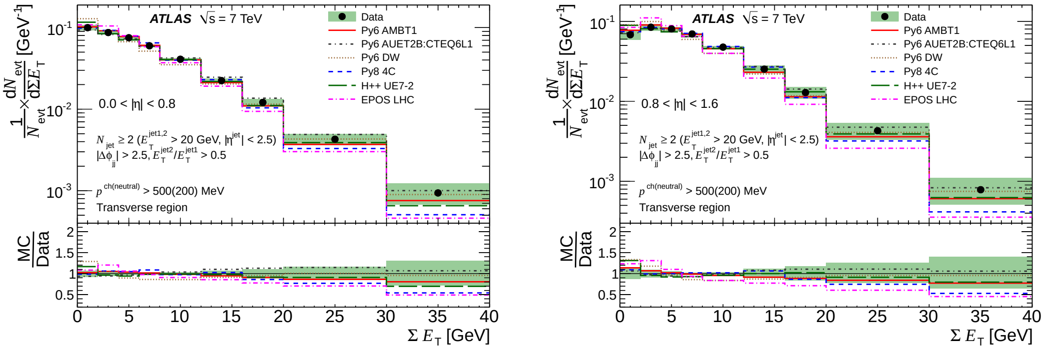

(a) $0.0 < |\eta| < 0.8$ **(b)** $0.8 < |\eta| < 1.6$

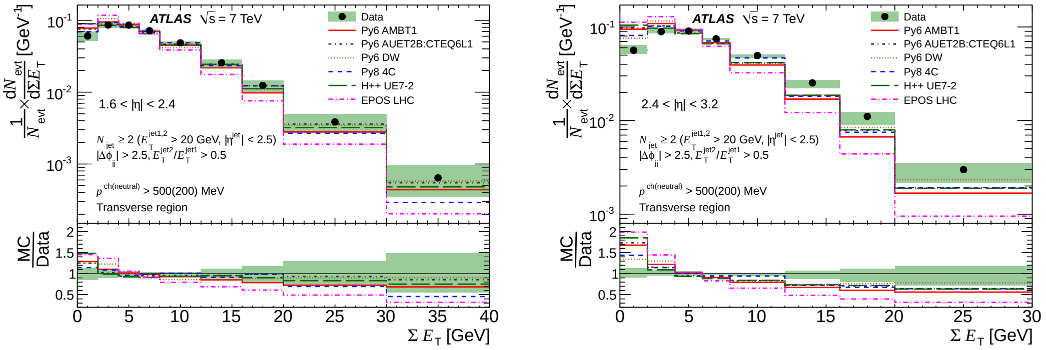

(c) $1.6 < |\eta| < 2.4$ **(d)** $2.4 < |\eta| < 3.2$

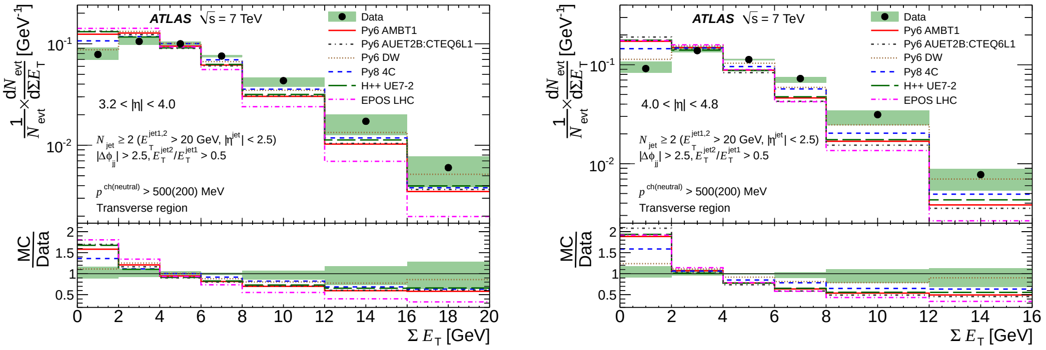

(e) $3.2 < |\eta| < 4.0$ **(f)** $4.0 < |\eta| < 4.8$

Figure 4.32: Unfolded ΣE_T distributions compared to various MC models and tunes for the di-jet selection in the transverse region in the following $|\eta|$ regions: (a) $0.0 < |\eta| < 0.8$, (b) $0.8 < |\eta| < 1.6$, (c) $1.6 < |\eta| < 2.4$, (d) $2.4 < |\eta| < 3.2$, (e) $3.2 < |\eta| < 4.0$ and (f) $4.0 < |\eta| < 4.8$. The filled band in each plot represents the total uncertainty on the unfolded data.

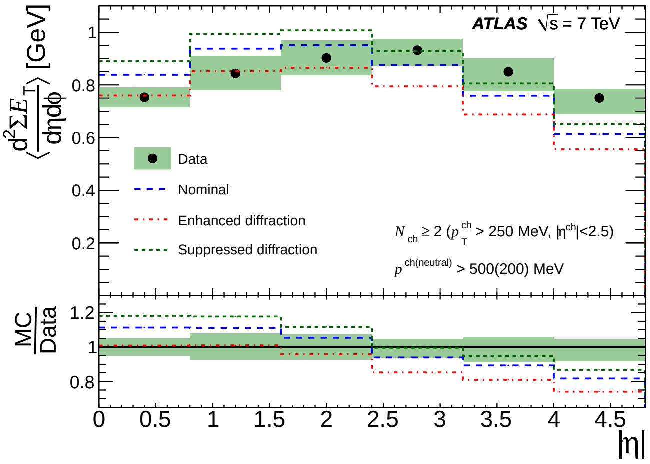

Figure 4.33: Unfolded E_T^{flow} distribution in the minimum bias data compared to `Pythia 8 4C` with the nominal diffractive cross-sections, as well as enhanced and suppressed diffractive cross-sections. The filled band represents the total uncertainty on the unfolded data.

switching the PDF set from `CTEQ6L1` to `MSTW2008LO` (dashed red), and comparing with the default `CTEQ6L1` tune. Switching the PDF set to `MSTW2008LO` decreases the activity in the central region, and increases it in the forward region. This can be reasoned in terms of the `MSTW2008LO` gluon PDF (Figure 4.34c), which features an increase in both high- and low-x gluon densities with respect to the mid-x region. As such, conservation of momentum dictates that there will be more particles with large longitudinal p and hence more forward activity.

As a final test, the PDFs' description of the relative forward to central activity is examined by scaling the default `CTEQ6L1` tune such that it agrees with `MSTW2008LO` in the most central $|\eta|$ bin (dashed green). This removes any increase (decrease) of activity in the forward region caused by an increase (decrease) of overall activity. The result is to pull the `CTEQ6L1` tune further away from the data in the forward region; as such, it is concluded that `MSTW2008LO` provides not only the best description overall, but also specifically in the forward region.

In addition, comparisons are made between the minimum bias E_T^{flow} and three `Pythia 6 AMBT2B` tunes [56] — two that use the above PDF sets (`MSTW2008LO` and `CTEQ6L1`) and another that uses a new PDF set, `CTEQ66c`. Unlike the `MSTW2008LO` and `CTEQ6L1` sets, `CTEQ66c` includes heavy flavour contributions from $c-$quarks. This is expected to increase the particle multiplicity in the forward region [57], as

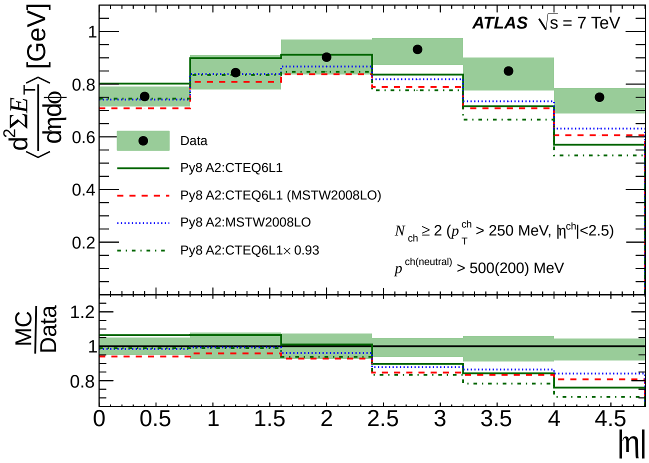

(a) Minimum bias

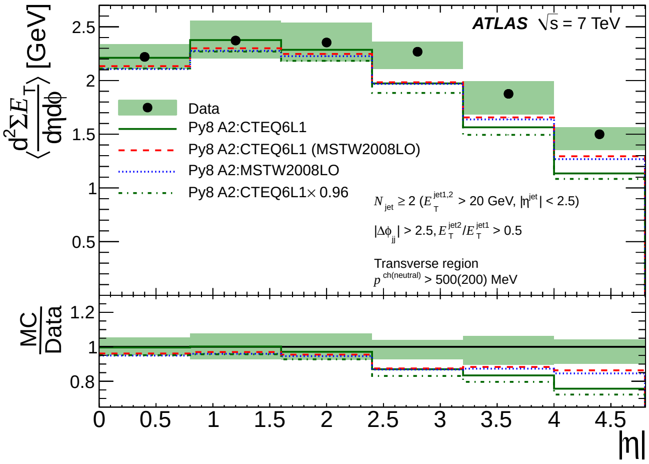

(b) Di-jets

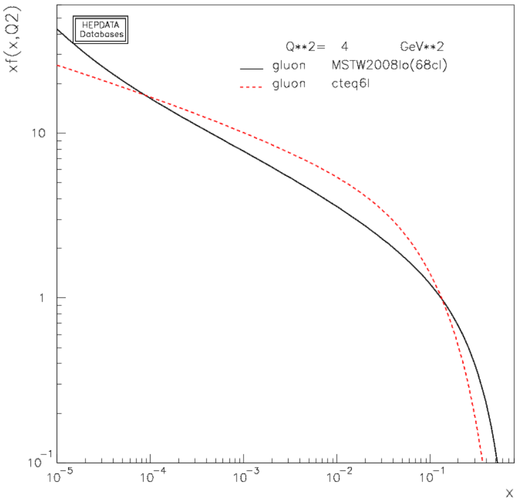

(c) Gluon PDFs

Figure 4.34: Unfolded E_T^{flow} distributions compared to `Pythia 8` with variations on the `MSTW2008LO` and `CTEQ6L1` PDFs used, as discussed in the text for (a) the minimum bias selection and (b) the di-jet selection. The filled band represents the total uncertainty on the unfolded data. (c) The `MSTW2008LO` and `CTEQ6L1` gluon PDFs for a low momentum transfer of $Q^2 = 4$ GeV. The $y-$axis is the product of the gluon's longitudinal momentum fraction x and the distribution function $f(x, Q^2)$, versus longitudinal momentum fraction x. This graph was made using the Durham HepData project [55].

heavy flavour content increases the parton density at high$-x$. However, as shown in Figure 4.35a, the activity is lower overall when compared to the standard `CTEQ6L1` PDF (the tune parameters are kept constant to allow direct comparison between the PDFs). This can again be explained in terms of the gluon PDFs, which are shown in Figure 4.35b: while the `CTEQ66c` PDF does have a slightly higher gluon fraction at high$-x$, it is much lower over the rest of the $x-$range. However, the $|\eta|-$dependence is improved with respect to both the standard `CTEQ6L1` and `MSTW2008LO` PDFs. Finally, in terms of the `AMBT2B` tune performance, the `MSTW2008LO` variation once again provides a comparatively better description than `CTEQ6L1`.

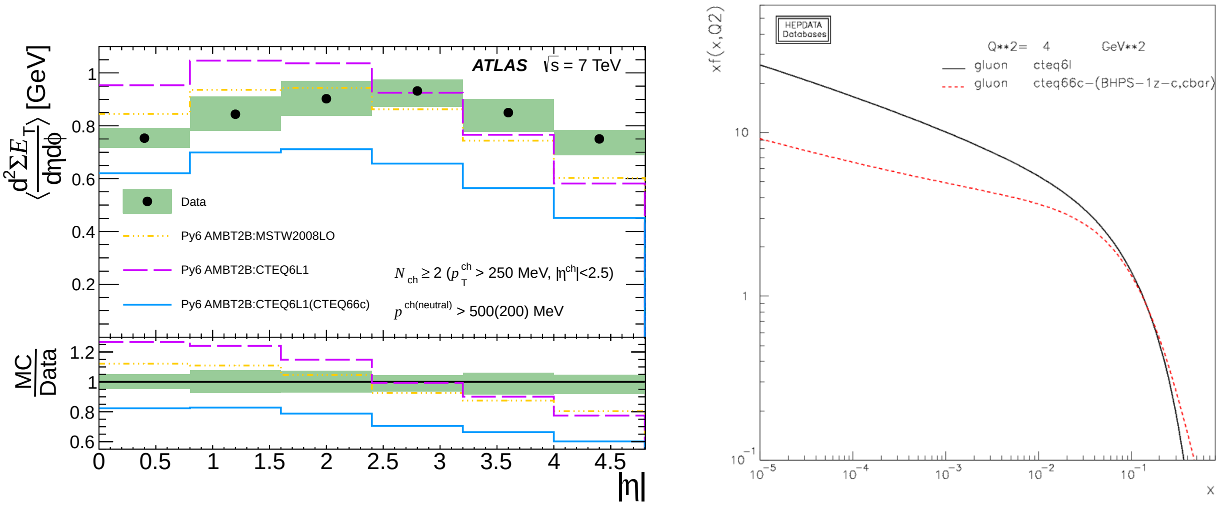

(a) Minimum bias

(b) Gluon PDFs

Figure 4.35: Figure (a) shows the unfolded minimum bias E_T^{flow} compared with `Pythia 6 AMBT2B` tunes, using the `MSTW2008LO`, `CTEQ6L1` and `CTEQ66c` PDF sets. Figure (b) shows the `CTEQ6L1` and `CTEQ66c` gluon PDFs for a low momentum transfer of $Q^2 = 4$ GeV. The $y-$axis is the product of the gluon's longitudinal momentum fraction x and the distribution function $f(x, Q^2)$, versus longitudinal momentum fraction x. This graph was made using the Durham HepData project [55].

4.8 Summary

Measurements of the E_T^{flow} and ΣE_T distributions as a function of $|\eta|$ in pp collisions have been conducted, for two event classes: one requiring, though not exclusively, the presence of low transverse momentum particles (minimum bias) and one requiring the presence of high transverse momentum particles (di-jets). To quantify the contribution from the underlying event to the total transverse energy, in the di-jet data the measurements are made in the region transverse in ϕ to the hard scatter. Both measurements include all charged particles with $p > 500$ MeV and all neutral particles with $p > 200$ MeV, and are the first of their type to utilise the entire acceptance ($|\eta| < 4.8$) of the ATLAS calorimeters. This allows the overall properties of inclusive pp collisions and the underlying event to be probed.

After using an iterative Bayesian unfolding to correct for detector effects, the results were compared to various MC models and tunes. In general all MC models under-predict the quantity of energy in the forward region with respect to the central region by 20-30%, with the exception of the `EPOS` model in minimum bias data and `Pythia 6 DW` tune in di-jet data. However, in minimum bias data the `Pythia 6 DW` tune underestimates the overall energy by 20-30%. In tests using the `Pythia 8 4C` tune, altering the contributions from diffractive processes was found to not change the relative central-forward E_T^{flow}. The PDF dependence was tested using the `Pythia 8 A2` series of tunes: it was found that the relative central-forward description is improved if `MSTW2008LO` PDFs are used instead of `CTEQ6L1` PDFs. Finally, the effect of including contributions from intrinsic charm using the `CTEQ66c` PDF was not found to improve the description with respect to the nominal `CTEQ6L1` PDF.

The results from these measurements are currently being used to constrain new ATLAS MC tunes. With the instantaneous luminosities at the LHC expected to increase even further when it commences with pp collisions at 14 TeV, these tunes will provide a much needed description of the relative forward-central contributions from pile-up and the underlying event, and ultimately facilitate more accurate measurements of low cross-section processes.

Chapter 5

A new technique for model independent missing transverse energy searches

“Mark Foley was right — there are no ghosts in this town.”
— Andrew Falkous

In addition to making measurements about the electroweak symmetry breaking scale, the LHC also provides the necessary energy to study above it. This chapter introduces a new technique for performing searches for large missing transverse energy ($\not\!\!E_T$) final states, which as discussed in Section 2.6 are a typical signature of physics beyond the Standard Model. Its strength lies in that it essentially measures well known SM processes, allowing the results to be interpreted independently of a specific “beyond the Standard Model” (BSM) theory. Furthermore, its measurements are made in terms of a ratio, allowing for the cancellation of correlated systematic uncertainties.

The measurement is conducted by selecting SM $Z \to \nu\bar{\nu}$ and $Z \to \mu^+\mu^-$ final states with a large $\not\!\!E_T$ and a jet. In the $Z \to \nu\bar{\nu}$ channel the jet requirement is necessary to ensure a $Z \to \nu\bar{\nu}$ candidate is selected, as otherwise there would be no observable net change in the transverse energy. For large $\not\!\!E_T$ BSM signatures the same is true, as the decay products are also invisible to the detector. As such the $Z \to \nu\bar{\nu}$ and BSM final states are equivalent; using $Z \to \nu\bar{\nu}$ candidates to perform the measurement therefore excludes them as a potential source of background. Events in the $Z \to \mu^+\mu^-$ channel can also be selected by the same method, provided that the muons are not included in the $\not\!\!E_T$ calculation. The expected SM ratio of branching fractions between the $Z \to \nu\bar{\nu}$ and $Z \to \mu^+\mu^-$ channels describes the benchmark for the measurement, explained in detail in the following section.

Due to time constraints the analysis itself is performed with Monte Carlo samples only, and as such the results should be interpreted as a proof of principle of the technique rather than a final measurement.

5.1 $Z \to ll$ production at the LHC

The primary Z boson production mechanism at the LHC is via the Drell-Yan channel, which involves $q\bar{q}$ annihilation: $q\bar{q} \to Z^0/\gamma^* \to l^+l^-$, shown in Figure 2.6b (Section 2.5). At next-to-leading order (NLO), the process may involve initial state radiation (ISR) from gluons (Figure 5.1a) and may occur through gluon scattering, yielding a jet in the final state (Figure 5.1b). This latter process can continue to increasing orders, such that multiple jets can accompany the leptonic final state, though the cross-section decreases with increasing orders.

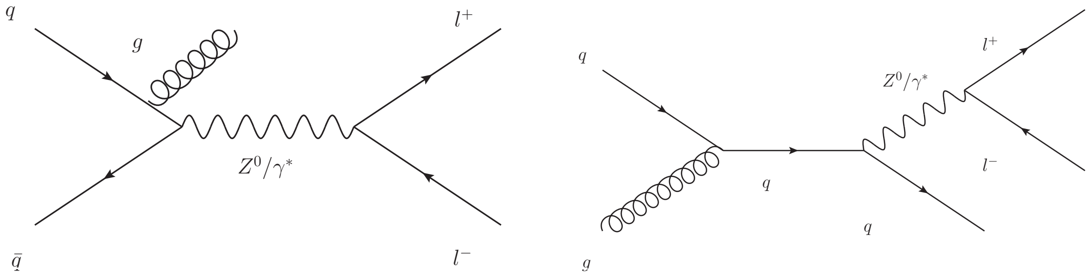

(a) Z production with ISR **(b)** Z production via gluon scattering

Figure 5.1: Next-to-leading order Drell-Yan Z boson production, showing (a) an initial state gluon and (b) production through gluon scattering, termed a "Z + 1 jet" process.

The total production cross-sections for various SM processes as a function of centre-of-mass energy $\sqrt{s}$, calculated to NLO accuracy with perturbative QCD, are shown in Figure 5.2. For LHC energies of $\sqrt{s} = 7$ TeV, the total Z cross-section is ≈ 30 nb, while the equivalent W cross-section is approximately three times larger;

this point will become more pertinent later. The $Z \rightarrow l^+l^-$ *branching fraction*, which represents the ratio of the $Z \rightarrow l^+l^-$ cross-section to the total $Z \rightarrow X$ cross-section, where X represents all allowed final states, is approximately 3.37% [58] for each of the muon, electron and tau channels.

As described in Section 2.5, the electroweak interaction also couples with neutrinos. The total $Z \rightarrow \nu\bar{\nu}$ branching fraction, where ν is any flavour of neutrino, is much larger than that of the $\mu^+\mu^-$ channel, with a value of approximately 20% [58]. Since neutrinos can not be directly detected, the $Z \rightarrow \nu\bar{\nu}$ cross-section was originally measured in e^+e^- collisions by subtracting the measured partial cross-sections ($Z \rightarrow ll$ and $Z \rightarrow hadrons$) from the total measured cross-section, obtained from line fits to the cross-section shape as a function of Z invariant mass [59].

The differing branching fractions between the neutrino and muon channels is a result of summing over the three neutrino flavours in the SM and the difference between the $Z \rightarrow \nu\bar{\nu}$ and $Z \rightarrow l^+l^-$ coupling strengths. Taking the ratio of these branching fractions yields a value of approximately 5.94:

$$\frac{\Gamma(Z \rightarrow \nu\bar{\nu})}{\Gamma(Z \rightarrow \mu^+\mu^-)} \approx 5.94 \tag{5.1}$$

Here $\Gamma(Z \rightarrow \nu\bar{\nu})$ represents the total branching fraction for $Z \rightarrow \nu\bar{\nu}$ processes. Experimentally this can be measured by using final states with jets to select $Z \rightarrow \nu\bar{\nu}$ events and placing requirements on the reconstructed di-muon invariant mass to select $Z \rightarrow \mu^+\mu^-$ events. Provided BSM particles interact with SM particles but interact only weakly with visible baryonic matter, at the detector level their presence would be inferred from a large $\not{E}_T$ and a final state jet from, for example, quark initial state radiation. As such these events can satisfy the selection criteria for $Z \rightarrow \nu\bar{\nu}$ events, detailed below. This would cause an increase in the ratio in Equation (5.1).

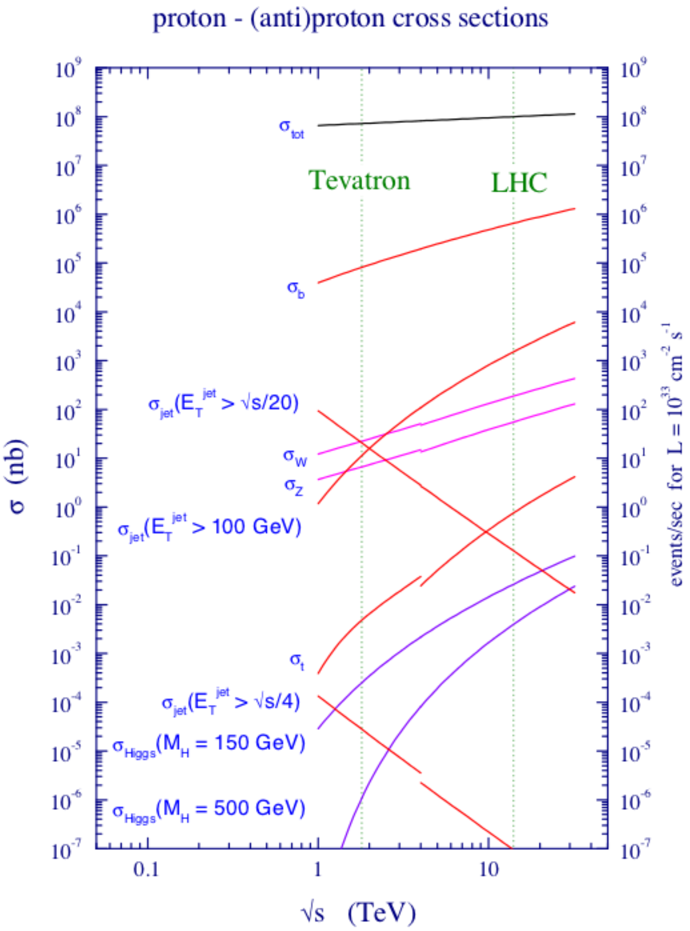

Figure 5.2: Standard Model cross-sections for a range of centre-of-mass energies, including the Tevatron and LHC. Taken from [60].

5.2 Definition of hadron level variables

The `ALPGEN` generator is used to produce $Z \to \nu\bar{\nu}$ and $Z \to \mu^+\mu^-$ Monte Carlo (MC) events at NLO, providing final states with $n-$jets, where $0 \leq n \leq 5$. The six samples are then weighted according to their relative cross-sections and combined.

The $\not{E}_T$ is equal to the vector sum of the Z boson decay products, plus any additional muons and neutrinos in the event. This best reflects the reconstructed level $\not{E}_T$ vector, which in the $Z \to \mu^+\mu^-$ case would not include the undetected neutrinos and omits muons. The lead jet is defined as the highest p_T jet in the event, which is taken to be the jet recoiling off the Z boson decay products.

5.3 Selection criteria

Due to time restrictions preventing a rigorous appraisal from being conducted, the event $Z \to \nu\bar{\nu}$ selection criteria used here is based on a previous analysis conducted by ATLAS, searching for final states with large $\not{E}_T$ and a single jet [61].

5.3.1 Hadron level selection

To select a $Z \to \nu\bar{\nu}$ event, the following fiducial region is constructed:

- A primary vertex with at least 2 ($p_T > 0.4$ GeV) tracks
- Lead jet $p_T > 120$ GeV and $|\eta| < 2.0$
- $\not{E}_T > 120$ GeV
- No more than two jets with $p_T > 30$ GeV and $|\eta| < 4.5$
- $\Delta\phi$ between the second jet and the $\not{E}_T$, $\Delta\phi_{jet2,\not{E}_T} > 0.5$
- No electrons or muons in the event

All hadron level jets are constructed using the anti-k_T algorithm with a jet radius $R = 0.4$. The lead jet and $\not{E}_T$ requirements ensure a high energy leading jet and large $\not{E}_T$. While technically it is instructive to require only a single jet to minimise background contributions from di-jet events, a second jet is allowed to increase the number of selected events, which needs to be as large as possible to make measurements in the statistically impoverished high $\not\!\!E_T$ ($\not\!\!E_T > 400$ GeV) region. To ensure that the second jet is not from di-jet production with the leading jet, a $\Delta\phi$ requirement is placed between it and the $\not\!\!E_T$ vector. Finally, to remove contamination from $Z \to l^+l^-$ and $W \to l\nu$ events, which would be present in real data, no final state electrons or muons are allowed.

To select $Z \to \mu^+\mu^-$ events, the same criteria is applied with the exception of the muon veto. In addition, two oppositely charged muons with $p_T > 20$ GeV and $|\eta| < 2.5$ and invariant mass $66 < M_Z < 116$ GeV are required. This cut helps reflect the reconstructed level selection.

5.3.2 Reconstructed level selection

At the reconstructed level, the $\not\!\!E_T$ is constructed by calculating the vector sum over all topological clusters (topoClusters) and taking the transverse component of the resulting energy. This is performed using calibrated topoClusters to account for energy losses in the detector, and does not include the contribution from muons; the latter is required because otherwise the $\not\!\!E_T$ in $Z \to \mu^+\mu^-$ events would be zero.

To select $Z \to \nu\bar{\nu}$ events, the same fiducial region as the hadron level is used. In addition, all events are required to pass an inclusive $\not\!\!E_T$ trigger [62] requiring a $\not\!\!E_T$ > 60 GeV at Event Filter. This trigger was found to be approximately 98% efficient for $\not\!\!E_T > 120$ GeV [61], and hence an $\not\!\!E_T$ cut of 120 GeV is chosen. Furthermore, standard ATLAS event cleaning is performed to better ensure a genuine collision event is selected. All jets are constructed using the anti-k_T algorithm ($R = 0.4$) with the leading jet required to pass additional requirements on its electromagnetic, f_{em}, and charged fraction, f_{ch}, where:

$$f_{em} = \frac{E_{em}}{E_{em} + E_{had}} > 0.1 \tag{5.2}$$

And:

$$f_{ch} = \frac{\sum^{N_{tracks}} p_T}{p_T^{jet}} > 0.02 \qquad (5.3)$$

Here E_{em}, E_{had} represent the jet energies measured in the electromagnetic (EM) and hadronic calorimeters; $\sum^{N_{tracks}} p_T$ is scalar sum of the p_T of the tracks associated with the primary vertex within a cone of radius $R = 0.4$ around the jet axis, and p_T^{jet} is the jet p_T as measured by the calorimeters. These requirements reduce the probability that the lead jet is produced by a cosmic ray or beam-background muon interacting with the calorimeters.

To enforce the veto on the presence of muons and electrons, requirements are placed on their reconstruction to better ensure that the detector level objects correspond to their true counterparts. To facilitate track reconstruction, both are required to originate from the inner detector ($|\eta| < 2.5$ for muons and $|\eta| < 2.47$ for electrons). Electron candidates are required to have $p_T > 20$ GeV and satisfy loose identification criteria, leading to a more stringent veto. Muon candidates are required to have $p_T > 7$ GeV, be identified in both the inner detector and muon spectrometer, and satisfy isolation criteria: the scalar sum of all tracks in a cone of radius $R = 0.2$ around (and excluding) the muon must be less than 1.6 GeV.

To select $Z \to \mu^+\mu^-$ events, two oppositely charged muons with $p_T > 20$ GeV, $|\eta| < 2.5$ and invariant mass $66 < M_Z < 116$ GeV are required. In addition, the same selection criteria as for $Z \to \nu\bar{\nu}$ candidates is required with the exception of the muon veto.

5.4 Background and signal

The dominant SM background process that can pass the $Z \to \nu\bar{\nu}$ selection cuts is from $W \to l\nu$ events where the lepton has either failed reconstruction or passed outside the acceptance. This hypothesis is corroborated by Figure 5.2, which shows that the W production cross-section at the LHC is approximately three times that of the Z; after accounting for the differing leptonic branching fractions [58], this increases to approximately a factor of ten. Further SM backgrounds include, in decreasing order of cross-section: single or pair production of top quarks, multijet production, beam-induced background muons and di-boson production. Figure 5.3 shows MC predictions of the $\not{E}_T$ in $Z \rightarrow \nu\bar{\nu}$, $Z \rightarrow \mu^+\mu^-$ and $W \rightarrow l\nu$ events at the hadron and reconstructed levels, after all selection cuts. The uncertainties in both distributions are purely statistical. To estimate their contribution to the background, the $W \rightarrow l\nu$ events are required to pass the same selection criteria as $Z \rightarrow \nu\bar{\nu}$ events. It is worth noting that in previous $\not{E}_T$ searches the $Z \rightarrow \nu\bar{\nu}$ and $Z \rightarrow \mu^+\mu^-$ channels are also considered as backgrounds.

The $Z \rightarrow \nu\bar{\nu}$ channel is predominant at both levels, indicating that the selection criteria is effective in selecting $Z \rightarrow \nu\bar{\nu}$ candidates. In the $Z \rightarrow \mu^+\mu^-$ channel, the kinematic and invariant mass requirements placed on potential $Z \rightarrow \mu^+\mu^-$ candidates causes a further reduction of the number of events. At the hadron level, the $W \rightarrow l\nu$ channel is higher than the $Z \rightarrow \mu^+\mu^-$ channel in the first two bins, but falls off more quickly as the $\not{E}_T$ increases. At the reconstructed level, however, the $W \rightarrow l\nu$ channel is higher than the $Z \rightarrow \mu^+\mu^-$ channel in all bins. This reflects both the requirement of the $Z \rightarrow \mu^+\mu^-$ candidate, which is subject to the muons' reconstruction efficiency, and the reduced strength of the $W \rightarrow l\nu$ muon veto at the reconstructed level, which is also dependent on the same effect. This is discussed in more detail in the following section.

In addition, to test the technique's sensitivity to BSM physics, an example dark matter candidate sample is included in Figure 5.3. The sample was produced using the MadGraph generator [63] and represents the $q\bar{q} \rightarrow \chi\chi$ production of $M = 200$ GeV dark matter particles via interaction with SM quarks or gluons (more detailed information can be obtained from reference [61]). Here, events are required to pass the $Z \rightarrow \nu\bar{\nu}$ selection. It is noted that while the small cross-section for this process results in a lower overall $\not{E}_T$ than the SM channels, the drop-off with increasing $\not{E}_T$ is much smaller. For higher $\not{E}_T$ values ($300 < \not{E}_T < 400$ GeV) it is equivalent to the $Z \rightarrow \mu^+\mu^-$ channel at the reconstructed level, and for the highest bin ($\not{E}_T > 400$ GeV) it is fractionally higher at the hadron level and approximately a factor of two larger at the reconstructed level.

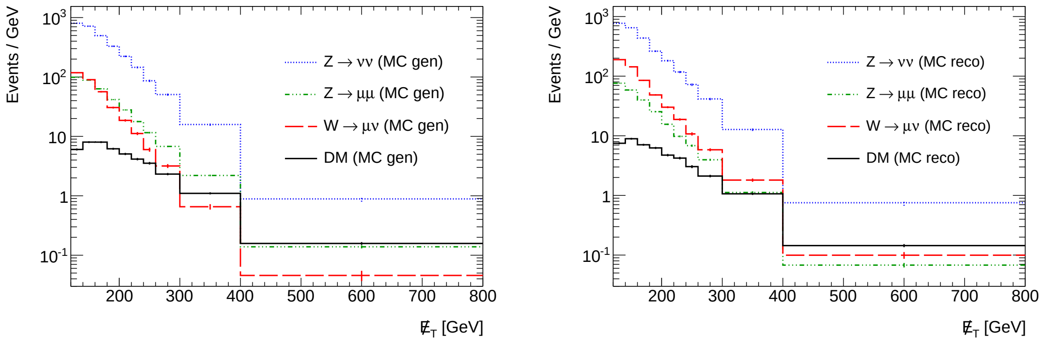

(a) $E\!\!\!/_T$ in hadron level events **(b)** $E\!\!\!/_T$ in reconstructed level events

Figure 5.3: `ALPGEN` MC 2011 predictions of the number of events from $Z \to \nu\bar{\nu}$, $Z \to \mu^+\mu^-$, $W \to l\nu$ and $q\bar{q} \to \chi\chi$ processes after all analysis selection cuts, as a function of (a) truth and (b) reconstructed $E\!\!\!/_T$. For the purposes of future data-MC comparison, these histograms are scaled by the total 2011 data integrated luminosity ($\int \mathcal{L}dt = 4.7$ fb^{-1}).

5.5 Results

To test how well the hadron level MC reproduces the expected ratio of cross-sections between $Z \to \nu\bar{\nu}$ and $Z \to \mu^+\mu^-$ candidates, Figure 5.4a shows their ratio as a function of $E\!\!\!/_T$ with an equivalent selection applied in both channels: events are required to have a $Z \to \nu\bar{\nu}$ or $Z \to \mu^+\mu^-$ candidate with invariant mass $66 < M_Z < 116$, a leading jet with $p_T > 40$ GeV and $E\!\!\!/_T > 40$ GeV. On average the result is slightly larger than the expected value (Equation (5.1)), and features a dependency on the $E\!\!\!/_T$. This is thought to be due to the difference in the $Z \to \nu\bar{\nu}$ and $Z \to \mu^+\mu^-$ invariant mass spectra, the latter of which — despite the invariant mass requirement — includes contributions from virtual γ^* and Z interference. The equivalent distribution at the reconstructed level is not shown, as it is not possible to place an invariant mass requirement in the $Z \to \nu\bar{\nu}$ channel. Again, the uncertainties shown in these and all following distributions are purely statistical.

The same distribution after all analysis cuts, at both the hadron and reconstructed levels, is shown in Figure 5.4b. The ratio at both levels increases significantly with respect to Figure 5.4a. This is due to the requirement of a Z boson candidate in the $Z \to \mu^+\mu^-$ channel only, which is necessary at the reconstructed level to reflect the selection that would be required in real data, and at the hadron level to ensure the selection is as close as possible to the reconstructed selection. The hadron level now reflects the selection necessary to perform corrections, which must account for the requirements placed at the reconstructed level. A significant discrepancy between the hadron and reconstructed level predictions is also observed, ranging from 25% in the first $\not\!\!E_T$ bin to over 30% in the highest, as shown in the ratio between the hadron and reconstructed distributions (lower panel). This provides an estimate of the correction factor necessary to correct real data back to the hadron level. Most of this discrepancy can be accounted for by the muon identification and reconstruction efficiency, which amounts to $\sim 90\%$ per muon [64] and hence $\sim 80\%$ per $Z \to \mu^+\mu^-$ candidate. The correction factor is not flat across the $\not\!\!E_T$ spectrum, however, with the high $\not\!\!E_T$ region showing the largest discrepancy. Further work is required to determine a reason for this $\not\!\!E_T$ dependency.

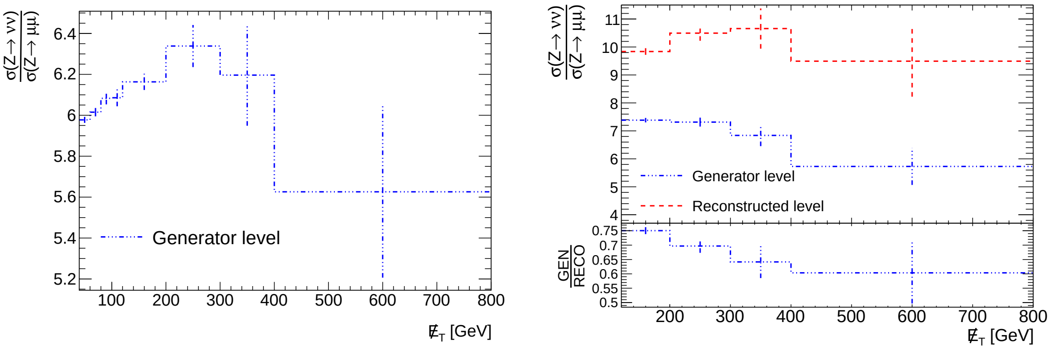

(a) Ratio without analysis cuts **(b)** Ratio with analysis cuts

Figure 5.4: Figure (a) shows the hadron level ratio of $Z \to \nu\bar{\nu}$ to $Z \to \mu^+\mu^-$ cross-sections where only a Z boson candidate is required in each channel. Figure (b) shows the same ratio at both the hadron and reconstructed levels after all analysis selection cuts.

To investigate the effect of $W \to l\nu$ background on the measurement, Figure 5.5 shows the ratio of cross-sections between $Z \to \nu\bar{\nu}$ plus $W \to l\nu$ candidates to $Z \to \mu^+\mu^-$ candidates as a function of $\not\!\!E_T$, in blue (red) at the hadron (reconstructed) levels. This provides an estimate of how the measurement would look in data if no signal events were present. As expected, including $W \to l\nu$ events increases the ratio at both the hadron and reconstructed levels (by approximately 10% and 20%, respectively). The effect is more pronounced at the reconstructed level, where, due to the aforementioned muon reconstruction inefficiencies, the muon veto is less effective.

Finally, to test the sensitivity of the measurement to the presence of dark matter particles in the presence of this background, Figure 5.5 also shows the ratio of cross-sections between $Z \rightarrow \nu\bar{\nu}$ plus $W \rightarrow l\nu$ plus dark matter candidates to $Z \rightarrow \mu^+\mu^-$ candidates, in green (purple) at the hadron (reconstructed) levels. This provides an estimate of how the measurement would look in data if signal events were present. The dark matter signal at both levels causes an increase across all bins with respect to the background-only prediction, with an $\sim 20\%$ increase for $\not{E}_T > 400$ GeV. The statistical error, however, limits a more precise calculation of the actual deviation. The lower panel shows the ratio between the hadron and reconstructed predictions, separately for the background-only (blue) and background plus signal scenarios (green). The two are almost exactly the same, indicating that the correction factor is independent of the presence of signal. This is an important result, as it shows that the correction procedure is not biased by the choice of signal model. It can be explained in terms of the the muon reconstruction efficiency, which affects both the $Z \rightarrow \nu\bar{\nu}$ and dark matter candidate selection approximately equally and hence cancels in their ratio.

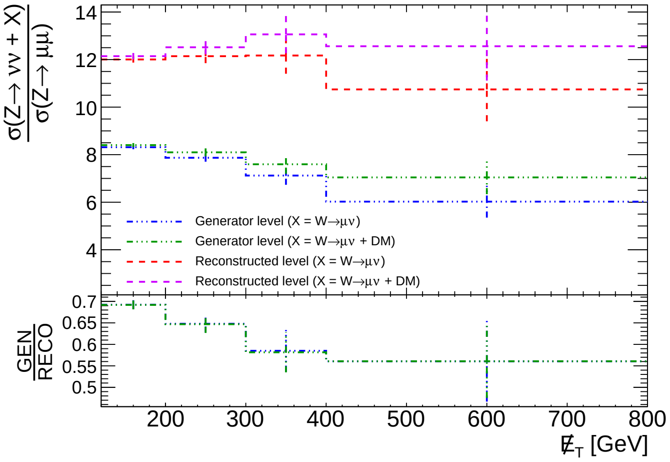

Figure 5.5: The ratio of $Z \rightarrow \nu\bar{\nu}$ plus background ($W \rightarrow l\nu$) to $Z \rightarrow \mu^+\mu^-$ cross-sections at the hadron (blue) and reconstructed (red) levels, and their ratio (lower blue distribution). Also shown is the ratio of $Z \rightarrow \nu\bar{\nu}$ plus background ($W \rightarrow l\nu$) plus signal ($q\bar{q} \rightarrow \chi\chi$) to $Z \rightarrow \mu^+\mu^-$ cross-sections, at the hadron (green) and reconstructed (purple) levels, and their ratio (lower green distribution).

5.5.1 Discussion

The results presented here provide an MC-based proof of principle of this method. As expected, the contribution from background is large across the $\not{E}_T$ range; in fact, the effect would be even greater if all further backgrounds mentioned in Section 5.4 were included. At higher $\not{E}_T$ values, however, the contribution from signal becomes more prominent, inducing a clear increase in the $Z \to \nu\bar{\nu}$ to $Z \to \mu^+\mu^-$ ratio.

The estimate of the correction factor necessary to bring the reconstructed MC (and real data) back to the hadron level is mostly accounted for in terms of muon reconstruction efficiencies. The unfolding technique described in the previous analysis (Section 4.5) could, for example, be used to perform such corrections. When applied to real data, this would enable direct comparison between experiment and theory independent of the detector used to record the data.

To complete the analysis, a thorough assessment of the potential backgrounds and systematic uncertainties would be performed. Those uncertainties correlated between the $Z \to \nu\bar{\nu}$ and $Z \to \mu^+\mu^-$ channels, such as the jet energy scale uncertainty, would cancel when calculating their ratio. This would yield a more accurate result than non-ratio based measurements. When correcting the data back to the hadron level, the background could either be subtracted directly, using data-driven estimates, or, as in this study, included in the MC sample used in the unfolding.

Finally, the statistical accuracy of the measurement as a whole would be improved by both increasing the number of generated MC events and by including the contribution from $Z \to e^+e^-$ events in the denominator of Equation (5.1). The latter would require a more involved selection criteria than in the $Z \to \mu^+\mu^-$ channel, which could be achieved by using existing ATLAS measurements as points of reference. Before conducting the study in data the statistical significance in the high $\not{E}_T$ region would need to be estimated first, potentially by using the distributions in Figure 5.3.

5.6 Summary

A new technique for performing model independent $\not{E}_T$ searches has been presented. It infers the presence of new particles with large $\not{E}_T$ from a deviation in the ratio of SM branching fractions between $Z \to \nu\bar{\nu}$ and $Z \to \mu^+\mu^-$ candidates. Preliminary MC studies indicate that the measurement is sensitive to the presence of an example dark matter candidate in a high background environment, causing a $\sim 20\%$ shift from SM expectations for $\not{E}_T > 400$ GeV. Furthermore, the correction factor necessary to correct the reconstructed level to the hadron level was found to be independent of the presence of signal.

Chapter 6

Measuring the inner detector trigger tracking efficiency

"Probe the earth to see where your main roots run."
— Henry David Thoreau

The high event rate at the LHC presents a challenging environment from which to extract interesting physics signatures. At the online level it is necessary — when all LHC bunches are filled — for the ATLAS trigger to reduce the 40 MHz bunch crossing rate to the 500 Hz output rate that can be written to disk offline. As a result the ATLAS High Level Trigger (HLT) algorithms must be fast and efficient to ensure that both interesting and rare physics events are not lost. Monitoring the performance of the inner detector (ID) trigger algorithms — responsible for reconstructing tracks from signatures such as muons, electrons and final states containing *b*-quarks — is therefore an important check of ATLAS data taking efficiency.

6.1 Inner detector monitoring

There are two main categories of event reconstruction — online and offline. The online reconstruction is performed by the HLT algorithms, which operate during ATLAS data taking and are consequently restricted to limited latencies: $\sim 10ms$ at level 2 (LVL2) and $\sim 1s$ at event filter (EF). The offline reconstruction is performed after ATLAS has finished taking data, allowing its algorithms to utilise a complete description of the detector and all the information provided by its sub-systems.

Numerous studies comparing the track reconstruction performance of the ID trigger with respect to the offline reconstruction have been conducted [65, 66]. A version of the code used to perform these analyses is also employed at the first stage of data reprocessing, forming part of an automated framework that monitors the ID trigger performance. This allows the efficiency of a given algorithm to be quickly determined without having to wait for the data to complete the various stages of checks necessary to ensure the highest quality for the analysis level.

This analysis makes a performance measurement without being biased — and hence essentially blinded — by the offline reconstruction. It therefore represents the first “true” measurement of the ATLAS ID trigger algorithm reconstruction efficiency. This important point is explained more clearly in terms of how the reconstruction efficiency is defined (Section 6.1.3). The code developed for the analysis has also been adapted to operate automatically at the first stage of data reprocessing.

To make a performance measurement of the ID without such a bias, only online information is used. This is performed by using objects defined at the EF, instead of fully reconstructed offline objects, as the reference sample with respect to which the efficiency is measured. Furthermore, the following criteria are necessary for a given EF object to be used to measure the ID trigger tracking efficiency:

- it is not required to have been reconstructed by the ID trigger algorithms
- it is a track belonging to a physics signature and hence should have been reconstructed by the ID algorithms

To meet these requirements, the following analysis utilises the “tag and probe” method, described below.

6.1.1 Tag and probe method

The tag and probe technique employed here uses standard candle SM processes to select reference ‘probe’ tracks from a properly ‘tagged’ sample of events. The tag track is required to have tracks in both the inner detector and an independent detector, while the probe track is required to be reconstructed in the independent detector only (Figure 6.1). The tag and probe candidates used in this analysis are muons from both $J/\Psi \rightarrow \mu^+\mu^-$ and $Z \rightarrow \mu^+\mu^-$ decays, treated separately. As such, the muon spectrometer is used as the independent detector. Muons provide a clean signature with which to make measurements, as they radiate much less bremsstrahlung than, say, electrons[1]. To form a tag and probe pair, the candidates must have an invariant mass close to the J/Ψ or Z mass. This, combined with the requirement of a tag track, helps to ensure that the probe track represents the muon spectrometer component of a muon produced from a J/Ψ or Z resonance decay. Since these particles' invariant masses differ by a factor of 30 ($M_{J/\Psi} \approx 3.1$ GeV), measuring their decay products allows the efficiency to be calculated over a wide range of momenta.

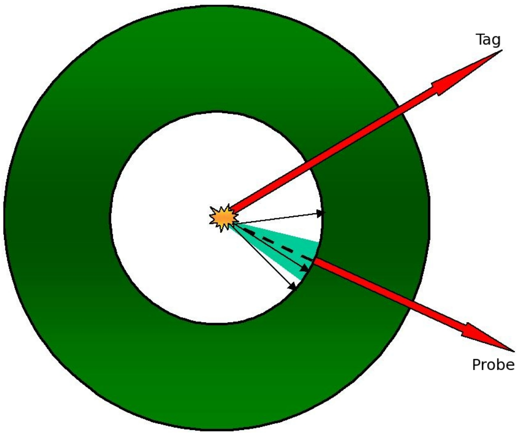

Figure 6.1: Simplified transverse view of the ATLAS detector. The inner circle represents the inner detector, and the green doughnut the muon spectrometer. Red arrows indicate muon tracks, black arrows indicate ID tracks, and the turquoise triangle represents the probe muon RoI within which the efficiency is determined.

6.1.2 Candidate selection

As outlined previously, it is necessary that the trigger used to select the $J/\Psi \rightarrow \mu^+\mu^-$ and $Z \rightarrow \mu^+\mu^-$ candidates places an ID requirement only on the tag muon; specifically, this requirement ensures that the tag muon candidate has tracks in both the ID and muon spectrometer and that these tracks are matched. This matching process is

---

[1] The probability of bremsstrahlung emission is proportional to $1/m^2$ of the incoming charged particle. Since $m_\mu \approx 100 m_e$, a muon is approximately 10^4 times less likely to radiate via bremsstrahlung.

specific to the muon reconstruction algorithm used (see [67] for a full description and performance review of ATLAS muon reconstruction algorithms), but the general process is to propagate all ID tracks with sufficient momentum out to the first station in the muon spectrometer and perform a match χ^2 using the difference between any nearby segment and the predicted extrapolation. Tracks passing this selection can then be defined as good muon objects and used as tag candidates.

The probe muon is required to have a track only in the muon spectrometer, not the ID. The direction of flight and the transverse impact parameter, d_0, must therefore be obtained by extrapolation to the interaction point. The extrapolation attempts to take into account energy losses of the muon in the upstream material (eg. calorimeters). This is not perfect, however, leading to differences in the extrapolated d_0 and the value obtained from direct measurement by the ID.

Furthermore, the p_T resolution is strongly dependent on which detector subsystem is used to measure it. For ID muons with $4 < p_T < 20$ GeV the resolution is dominated by multiple scatters, and has a value of $\sigma_{p_T}/p_T \approx 2\%$. For muon spectrometer tracks, the resolution is most dependent on energy loss fluctuations for $p_T < 10$ GeV (low$-p_T$), and multiple scatters for $p_T > 10$ GeV (high$-p_T$). For low$-p_T$ muon spectrometer tracks this results in a resolution of $\sigma_{p_T}/p_T \approx 5\%$ [67]. As such, stand-alone muon spectrometer tracks suffer from worse measurement than their combined counterparts, since the latter uses the better measured ID track parameters to calculate the p_T.

To form a di-muon candidate, the tag and probe pair is required to pass a set of selection criteria: explicitly, the two muons must have opposite signed charge, originate from separate RoIs within the ID, and the invariant mass of the di-muon pair must fall within a window centred on the mass of the intended meson or gauge boson candidate (exact values are given in Table 6.1). Note that the separate RoI and invariant mass requirements ensure that the di-muon pair is not made by a tag muon and its own muon spectrometer track, the latter of which can be poorly measured and thus mimic a separate probe track.

If these requirements are satisfied, the muon pair are deemed to have been products of a genuine $J/\Psi \rightarrow \mu^+\mu^-$ or $Z \rightarrow \mu^+\mu^-$ decay; as a sanity check, Figure 6.2 shows invariant mass plots for each decay type in data and MC. The MC used here represents signal events generated by the `Pythia 6` (`Pythia 8`) models for the $J/\Psi \rightarrow \mu^+\mu^-$

($Z \rightarrow \mu^+\mu^-$) channels. Though displaying clear peaks at the respective invariant masses, data and MC do not agree well, with the data having a broader distribution in both channels. This suggests the presence of background in the data sample, which may falsely alter the efficiency. This is investigated quantitatively in Section 6.1.4.

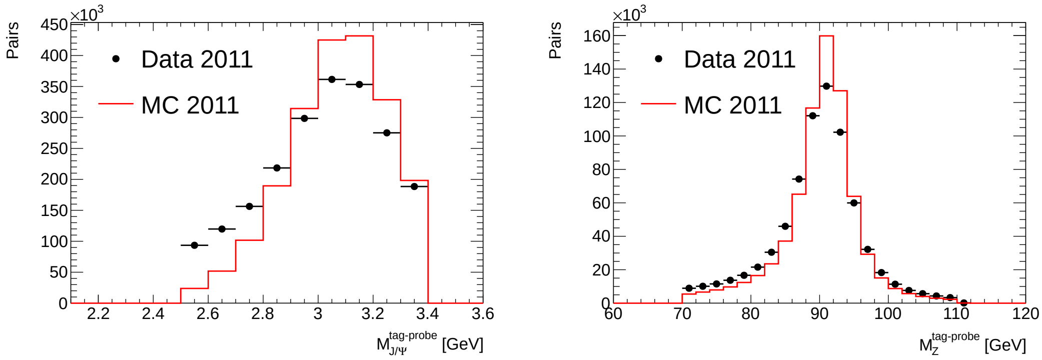

(a) $J/\Psi \rightarrow \mu^+\mu^-$ 2011 **(b)** $Z \rightarrow \mu^+\mu^-$ 2011

Figure 6.2: The tag and probe invariant mass spectrum, for (a) $J/\Psi \rightarrow \mu^+\mu^-$ and (b) $Z \rightarrow \mu^+\mu^-$ candidates. The MC used in figure (a) represents prompt J/Ψ decays (though the invariant mass spectrum should not be dependent on lifetime). In both cases the MC is normalised to the integral of the data, and the range is restricted by the trigger invariant mass requirement.

	probe p_T (GeV)	probe $\lvert\eta\rvert$	$q_{\mu^1} \cdot q_{\mu^2}$	$M_{inv}^{tag-probe}$(GeV)
J/Ψ	> 4.0	< 2.5	< 0	$2.5 < M_{J/\Psi}^{tag-probe} < 3.4$
Z	> 10.0	< 2.5	< 0	$71.2 < M_Z^{tag-probe} < 111.2$

Table 6.1: Numerical values for tag and probe di-muon ($J/\Psi \rightarrow \mu^+\mu^-$ or $Z \rightarrow \mu^+\mu^-$) candidate selection.

6.1.3 Calculating the track reconstruction efficiency

If a di-muon candidate is selected, the efficiency of the L2 and EF reconstruction algorithms can be measured. The base requirement for a given algorithm to be considered efficient is that it successfully reconstructed a suitable ID track in the probe RoI. Initially this was tested by applying a matching requirement in terms of (η, ϕ) between the probe and any potential ID track candidate. However, it was found that the large measurement errors on the J/Ψ probe muon ϕ variable resulted in ID track candidates being missed, producing a falsely low efficiency.

To circumnavigate the dependency of the efficiency on the probe muon resolution, a given algorithm is considered efficient if it provides an ID track from the probe RoI that forms a J/Ψ or Z di-muon candidate with the tag track. The criteria to form an ID-tag di-muon candidate are:

- the ID track is required to originate from the probe RoI
- the ID-tag pair are required to pass an invariant mass cut: $1.5 < M_{J/\Psi}^{tag-ID} < 6.2$ GeV and $60.0 < M_Z^{tag-ID} < 120.0$ GeV for the $J/\Psi \to \mu^+\mu^-$ and $Z \to \mu^+\mu^-$ channels respectively

The invariant mass cuts are looser than those for the tag and probe selection (Table 6.1); this is to ensure that the matching is less dependent on the ID (or tag) track parameter resolutions. To determine the exact values, Figure 6.3 shows the tag and probe invariant mass ($M_{J/\Psi}^{tag-probe}$) versus the tag and ID track invariant mass ($M_{J/\Psi}^{tag-ID}$) for the IDSCAN and Strategy A algorithms in 2011 ($\sqrt{s} = 7$ TeV) and 2012 ($\sqrt{s} = 8$ TeV) pp collision data, respectively. The first bin on the $M_{J/\Psi}^{tag-ID}$ axis represents inefficiencies — if $M_{J/\Psi}^{tag-ID} = 0$, then the tag has not managed to find a match; that there are approximately twice as many entries in this bin for Strategy A indicates that it is less efficient than IDSCAN, which is indeed observed in the final results.

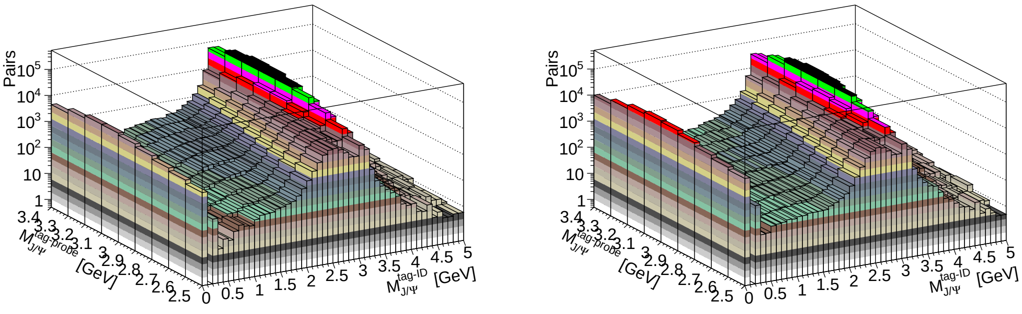

(a) $J/\Psi \to \mu^+\mu^-$ 2011 **(b)** $J/\Psi \to \mu^+\mu^-$ 2012

Figure 6.3: The tag and probe invariant mass spectrum versus the tag and ID track invariant mass spectrum in the $J/\Psi \to \mu^+\mu^-$ channel, for (a) IDSCAN 2011 and (b) Strategy A 2012 data. The $z-$axis shows the number of tag and probe pairs per event, on a logarithmic scale.

The entries in the third bin on the same axis ($0.2 < M_{J/\Psi}^{tag-ID} < 0.3$ GeV) represent cases where the tag track has been matched to its own ID track, yielding an invariant mass for the pair of $M_{J/\Psi}^{tag-ID} \approx 2M_{\mu} \approx 0.21$ GeV. This is possible if the two muon RoIs overlap — a common occurrence in J/Ψ decays, which, due to their small mass, tend to have a significant longitudinal boost. Therefore this bin is also considered as inefficient, placing the lowest possible matching cut at around $M_{J/\Psi}^{tag-ID} > 300$ MeV.

The region between this bin and the peak around the J/Ψ mass on the $M_{J/\Psi}^{tag-ID}$ axis is populated by potential ID-tag candidates. Hypothetically all these pairs could be considered as successful matches — a separate ID track has been found, and the resulting pair may have an invariant mass away from the J/Ψ mass due to resolution effects on either or both of the tracks. However, it was found that treating all the candidates in this region as efficient renders the measurement more dependent on tracks not originating from the J/Ψ candidate. As such, the final cut values were chosen to minimise this effect whilst also being loose enough to minimise the dependency of the efficiency on resolution effects.

In the $Z \to \mu^+\mu^-$ channel the matching criteria is less dependent on resolution effects — the ID track pattern recognition algorithms are ideally suited to high$-p_T$ reconstruction, and tracks of this type traverse a greater distance in the muon spectrometers and hence register more hits in the tracking chambers. It was found that the efficiency was largely independent of the chosen cuts, varying by as little as 0.01% over a wide range. As such the actual values are somewhat arbitrary, and were chosen to safely ensure that any residual resolution effects (the resolution is inversely dependent on the track curvature, which is small for high$-p_T$ tracks) are accounted for.

The efficiency is defined as:

$$\epsilon_{ID} = \frac{N_{ID+tag}}{N_{tag}} \tag{6.1}$$

Here N_{ID+tag} is equal to the total number of ID-tag pairs, and N_{tag} is equal to the total number of tag and probe candidates. The benefit of using EF instead of offline muons is apparent from Equation (6.1) — if an offline muon was required in the denominator, then ϵ_{ID} would be defined in terms of events that had passed the full reconstruction. This biases the final efficiency, since an inefficient event at (say) L2 may not pass the requirements after full reconstruction; thus, despite being inefficient, it would not be included in Equation (6.1).

6.1.4 Systematic uncertainties

It is possible that a background muon, such as those originating from decays in flight of light mesons and from semi-leptonic $b-$ and $c-$hadron decays, forms a tag muon and hence a tag and probe pair. This can alter both the numerator and denominator in Equation (6.1).

To test and assign a suitable systematic uncertainty to this effect in the 2011 data sample, a measurement of the background is performed. Since discrepancies between the data and MC invariant mass spectra are thought to be due to contributions from background, the J/Ψ and Z invariant mass spectra are used to model and hence provide a handle on this background.

The $J/\Psi \to \mu^+\mu^-$ channel is considered first, as the discrepancy between data and MC is more prominent. As a first step, signal $J/\Psi \to \mu^+\mu^-$ MC is used to perform a fit over the entire tag and probe invariant mass range allowed by the trigger used to select the events in data ($2.5 < M_{J/\Psi}^{tag-probe} < 4.3$ GeV), shown in Figure 6.4a. The function with the smallest χ^2/degree of freedom fit was found to be a convolution of a Gaussian and a Breit-Wigner.

With the shape of the signal peak determined, this functional form is used to fit the signal in data, with a polynomial of varying orders used to fit the background (Figure 6.4b). The background function with the smallest χ^2/degree of freedom fit to the signal plus background was found to be a parabola. Figures 6.4c and 6.4d show separately both the efficiency and the signal to signal plus background ratio ($S/(S+B)$) as a function of invariant mass.

From these distributions the efficiency as a function of $S/(S+B)$ is obtained, in the following manner: using Figure 6.4c, the $S/(S+B)$ values are grouped into bins of width 0.1, for $0 < S/(S+B) < 1$. In a given $S/(S+B)$ bin the efficiency is then obtained by separately summing the numerator and denominator values corresponding to the invariant mass of each point in the bin, as given by the numerator and denominator histograms used to make Figure 6.4d, and dividing the two sums. The statistical uncertainty on the efficiency is calculated using binomial error propagation, as the numerator and denominator histograms contain correlated entries. In both cases the bins with $M_{J/\Psi}^{tag-probe} > 4.0$ are excluded as the fit obtained in Figure 6.4a does not describe the shape of the distribution well in this region. The resulting distribution yields the efficiency as a function of $S/(S+B)$, as shown in Figure 6.4e. A linear extrapolation is then performed to obtain the efficiency given a hypothetical "pure" sample (100% signal).

From Figure 6.4e a constant systematic error is derived by calculating the average efficiency (in the analysis range $2.5 < M_{J/\Psi}^{tag-probe} < 3.4$ GeV) and taking the difference with the pure signal efficiency, yielding a value of $\sim 0.4\%$ in each variable bin at L2 and 0.3% at EF. When determining the efficiency as a function of the probe muon p_T, however, the systematic derivation was performed separately in two bins of probe muon p_T: $0 < p_T^{probe} < 8$ GeV and $8 < p_T^{probe} < 13$ GeV. Since the algorithms are suited to high$-p_T$ reconstruction, it was hypothesised that the efficiency would be less background dependent in the region $8 < p_T^{probe} < 13$ GeV. This is confirmed, with the Strategy A systematic uncertainty found to be $\sim 0.8\%$ ($\sim 0.5\%$) in the $0 < p_T^{probe} < 8$ GeV region and $\sim 0.1\%$ ($\sim 0.05\%$) in the $8 < p_T^{probe} < 13$ GeV region at L2 (EF). A similar relationship is found in the other algorithms at L2 and EF.

The same process is repeated for 2012 data and MC, as shown in Figure 6.5, yielding a slightly larger systematic value of $\sim 1\%$ at L2 and ~ 0.6 at EF. These larger values suggest a higher level of background in the 2012 data than 2011; this may be a result of the higher instantaneous luminosities at which the LHC ran in 2012, resulting in more pile-up vertices, which may in turn lead to a higher probability that a track from these additional vertices mimics one of the J/Ψ tracks.

To finalise the study, the process was repeated in both 2011 and 2012 data with an offline track required to be matched to the probe. This translates to an offline track being required in the denominator of Equation (6.1), causing the efficiency to be defined in terms of the offline reconstruction. This is necessary when measuring the efficiency as a function of d_0 or z_0, as the probe parameters are determined via extrapolation and hence inaccurate. Figure 6.6 shows this efficiency as a function of the signal to signal plus background ratio for each year. It is much less dependent on the fraction of background, varying by $\sim 0.01\%$ ($< 0.01\%$) in 2011 and $\sim 0.2\%$ ($\sim 0.02\%$) in 2012 at L2 (EF). This indicates that the efficiency is less dependent on the presence of a J/Ψ candidate if an offline track is required. In all cases this systematic uncertainty was found to be negligible ($< 0.1\%$) for $Z \rightarrow \mu^{+}\mu-$ candidates.

In addition, the systematic effect of varying the tag-ID matching cut was estimated by comparing the efficiency with respect to invariant mass between the nominal cut values and slightly tightened ($2.0 < M_{J/\Psi}^{tag-ID} < 5.7$ GeV and $70 < M_{Z}^{tag-ID} < 110$ GeV) and slightly loosened ($1.0 < M_{J/\Psi}^{tag-ID} < 6.7$ GeV and $50 < M_{Z}^{tag-ID} < 130$ GeV) versions, shown in Figure 6.7. The cut variations were chosen so as to avoid cutting too deeply into the $M_{J/\Psi}^{tag-ID}$ invariant mass peak (Figure 6.3). The resulting systematic uncertainty, obtained separately for each variable using similar distributions, is $\sim 0.4\%$ and $\sim 0.1\%$ for J/Ψ at L2 and EF for both years, with smaller values for the measurements with respect to offline tracks. It is noted that the uncertainty obtained from the looser cut is larger than that from the tighter cut, due to the presence of more background events. This systematic is again found to be negligible for Z candidates.

To obtain the total systematic uncertainty on the upper-bound, the systematic obtained from the tighter cut is added in quadrature with that obtained from the background systematic. The lower-bound is equal to the systematic obtained from the looser cut only.

6.1.5 Results

The L2 and EF track reconstruction efficiencies as a function of various probe and event variables, for both J/Ψ and $Z \rightarrow \mu^{+}\mu^{-}$ candidates, are shown in Figures 6.8-6.14. In all distributions at L2 the IDSCAN algorithm is shown for 2011, with the Strategy A and B labels referring to the 2012 implementations of IDSCAN and SiTrack, respectively. As discussed in Section 3.3.1, the Strategy A (IDSCAN) algorithm is the primary L2 algorithm for muon reconstruction; however, for reasons that will be discussed shortly, the Strategy B algorithm was ultimately used as the lead L2 algorithm in 2012. Results from the offline-like algorithm, Strategy C, are also shown, with an overview given after the main discussion. In all figures the efficiency at the EF level averages at 99% in 2011 and 99.2% in 2012 for $J/\Psi \rightarrow \mu^{+}\mu^{-}$ candidates. For $Z \rightarrow \mu^{+}\mu^{-}$ candidates it is 100% for both years. As such the EF distributions are only discussed if some dependency on the plotted variable is observed. The data used here represent the complete integrated luminosity in 2011 (4.9 fb^{-1}) and

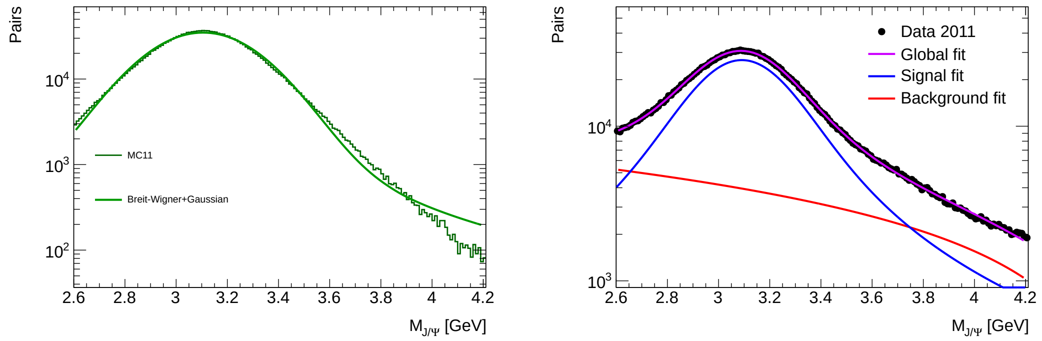

(a) $J/\Psi \rightarrow \mu^+\mu^-$ data 2011 **(b)** $J/\Psi \rightarrow \mu^+\mu^-$ MC 2011

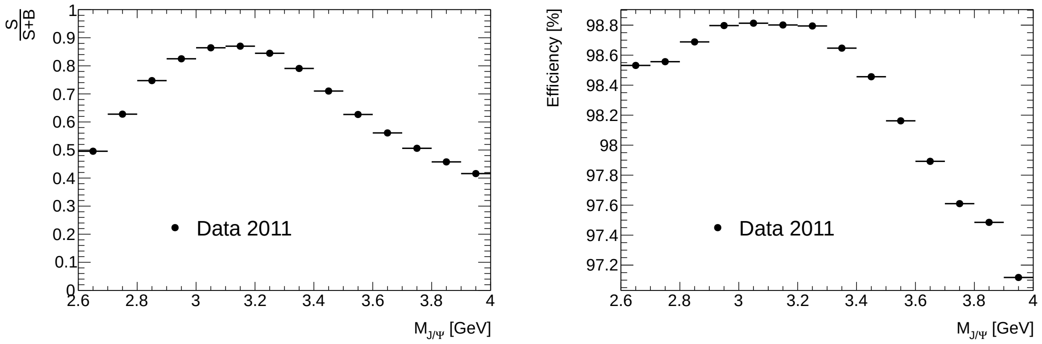

(c) S/(S+B) as a function of $M_{J/\Psi}^{tag-probe}$ **(d)** Efficiency as a function of $M_{J/\Psi}^{tag-probe}$

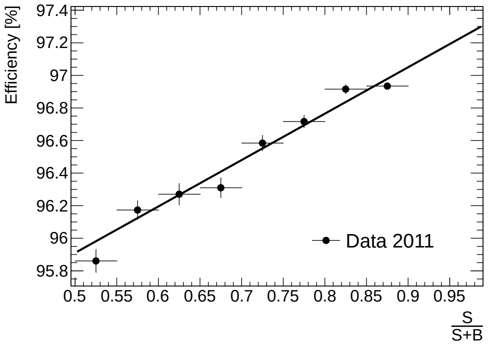

(e) Efficiency as a function of S/(S+B)

Figure 6.4: Figure (a) shows the invariant mass of signal $J/\Psi \rightarrow \mu^+\mu^-$ MC 2011 IDSCAN tag and probe pairs. The shape is fit with a convolution of a Gaussian and a Breit-Wigner function. Figure (b) shows the invariant mass of $J/\Psi \rightarrow \mu^+\mu^-$ data 2011 IDSCAN tag and probe pairs. The signal peak is fit with a convolution of a Gaussian and a Breit-Wigner, and the background shape fit with a parabola. Figure (c) shows S/(S+B) as a function of $M_{J/\Psi}^{tag-probe}$, and Figure (d) shows the IDSCAN track reconstruction efficiency as a function of $M_{J/\Psi}^{tag-probe}$. In both these figures the $x-$axis range is limited to 4 GeV, as the fit defined in (a) does not describe the signal shape for $M_{J/\Psi}^{tag-probe} > 4$ GeV. Finally, Figure (e) shows the efficiency as a function of S/(S+B). A linear fit is made to the data and extrapolated to the "pure-signal" scenario, $S/(S+B) = 1$.

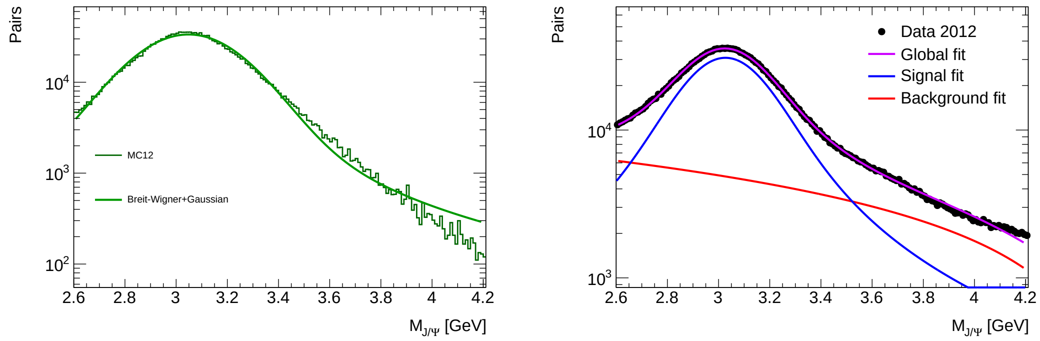

(a) $J/\Psi \rightarrow \mu^+\mu^-$ data 2012 **(b)** $J/\Psi \rightarrow \mu^+\mu^-$ MC 2012

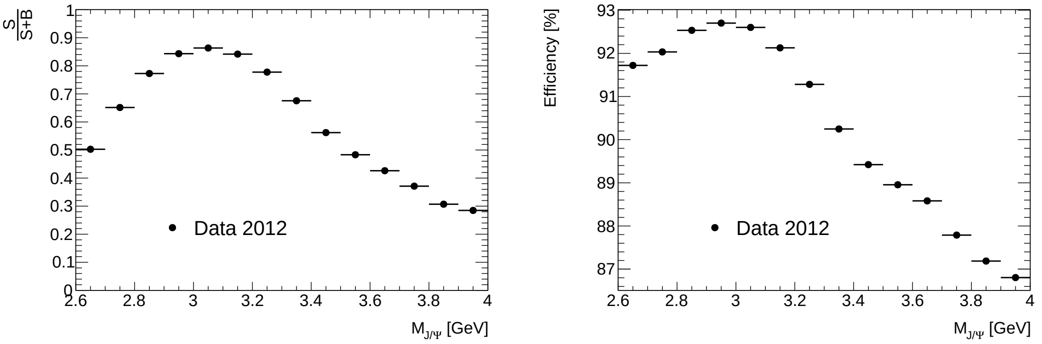

(c) S/(S+B) as a function of $M_{J/\Psi}^{tag-probe}$ **(d)** Efficiency as a function of $M_{J/\Psi}^{tag-probe}$

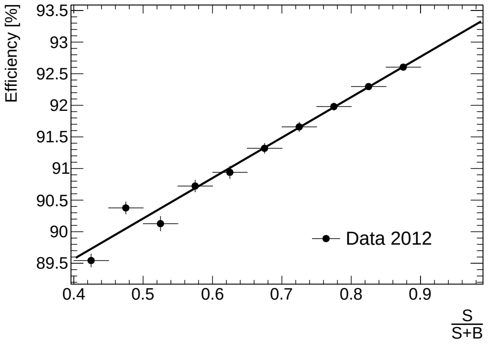

(e) Efficiency as a function of S/(S+B)

Figure 6.5: Figure (a) shows the invariant mass of signal $J/\Psi \rightarrow \mu^+\mu^-$ MC 2012 Strategy A tag and probe pairs. The shape is fit with a convolution of a Gaussian and a Breit-Wigner function. Figure (b) shows the invariant mass of $J/\Psi \rightarrow \mu^+\mu^-$ data 2012 Strategy A tag and probe pairs. The signal peak is fit with a convolution of a Gaussian and a Breit-Wigner, and the background shape fit with a parabola. Figure (c) shows S/(S+B) as a function of $M_{J/\Psi}^{tag-probe}$, and Figure (d) shows the Strategy A track reconstruction efficiency as a function of $M_{J/\Psi}^{tag-probe}$. In both these figures the $x-$axis range is limited to 4 GeV, as the fit defined in (a) does not describe the signal shape for $M_{J/\Psi}^{tag-probe} > 4$ GeV. Finally, Figure (e) shows the efficiency as a function of S/(S+B). A linear fit is made to the data and extrapolated to the “pure-signal” scenario, $S/(S+B) = 1$.

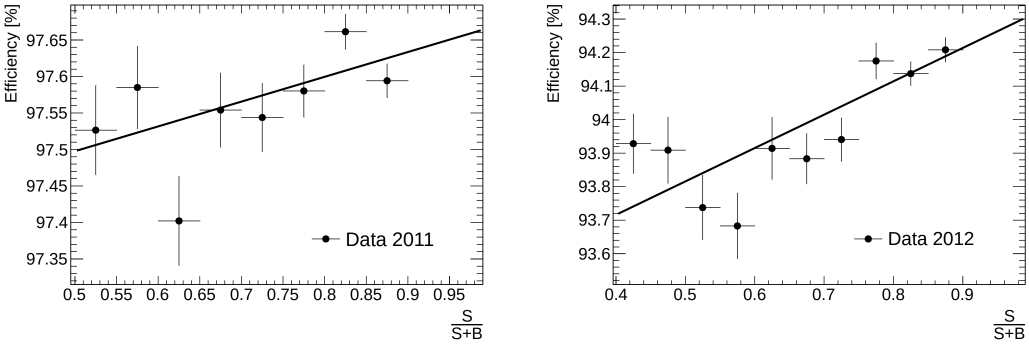

(a) Offline efficiency as a function of S/(S+B) in 2011 **(b)** Offline efficiency as a function of S/(S+B) in 2012

Figure 6.6: Figure (a) shows the IDSCAN track reconstruction efficiency as a function of signal over signal plus background, in 2011 data, when an offline track is required to be matched to the probe. Figure (b) shows the equivalent for Strategy A in 2012 data.

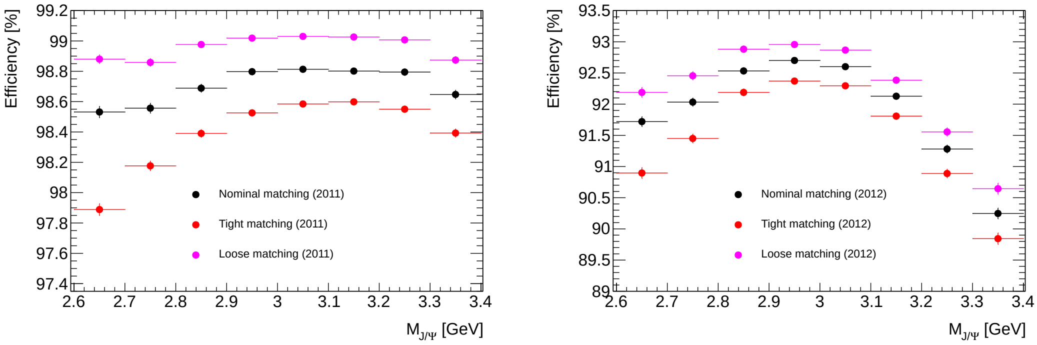

(a) Efficiency versus invariant mass in 2011 **(b)** Efficiency versus invariant mass in 2012

Figure 6.7: Figure (a) shows the IDSCAN reconstruction efficiency in data as a function of tag and probe invariant mass. Figure (b) shows the equivalent for Strategy A. The black distribution corresponds to tag candidates matched with the nominal ($1.5 < M_{J/\Psi}^{tag-ID} < 6.2$ GeV) matching cut; the red distribution corresponds to a tighter matching requirement ($2.0 < M_{J/\Psi}^{tag-ID} < 5.7$ GeV); and the magenta distribution corresponds to a looser matching requirement ($1.0 < M_{J/\Psi}^{tag-ID} < 6.7$ GeV).

approximately the same from the 2012 data set. As such, the effects of pile-up are present and can be measured.

For low probe p_T muons ($4 < p_T < 13$ GeV), shown in Figure 6.8, Strategy A features a sharp drop in efficiency, lowering the average efficiency to $\sim 92\%$. This is not observed in its 2011 equivalent, which returns an approximately flat efficiency of $\sim 97\%$. Insight into the cause of this drop was obtained via co-operation with a separate analysis group measuring the B_s lifetime using $B_s \rightarrow J/\Psi\phi$ decays. The measured mean lifetime was found to be substantially shorter in 2012 than 2011 data, with a fractional difference of $\sim 10\%$. This indicated that a significant number of delayed J/Ψ decays[2] were being missed from the calculation. Since decays of this type are displaced from the primary vertex, the efficiency with respect to the probe track d_0 was examined (Figure 6.9). Here an offline track matched to the probe track is used to obtain the d_0, as the probe track suffers from poor resolution; the systematic uncertainty on each point is smaller, as discussed in Section 6.1.4. The Strategy A efficiency is strongly dependent on d_0, dropping as low as 80% for $0.5 < d_0 < 1.5$ mm, while its 2011 equivalent remains flat (within errors). A similar relationship is observed in Strategy A in terms of the offline track displacement along the beamline, z_0, though the dependency is not as great (Figure 6.10).

To ascertain the cause of the efficiency loss, an investigation into the Strategy A pattern recognition software was conducted. It was found that the requirement placed on the z-position of track hits used to construct vertices was too severe, causing many displaced vertices to be missed. As mentioned in Section 3.3.1 this was initially tightened when moving from IDSCAN to Strategy A to ensure high$-p_T$ tracks would not be missed in the increased pile-up environment. As such the Strategy B algorithm, which maintained a flat efficiency of $\sim 98\%$, was used as the default for low$-p_T$ muon tracking and analysis in 2012.

To determine if the efficiency has any geometrical dependence, Figures 6.11 and 6.12 show the efficiency with respect to the probe track η and ϕ variables, respectively. In the $J/\Psi \rightarrow \mu^+\mu^-$ channel the efficiency is generally flat for $|\eta| < 1.0$, but drops are observed in all algorithms at L2 and EF in the bins $1.0 < |\eta| < 1.2$. This corresponds to the crack region described in Section 3.2.1, which causes poor track resolution. The same effect is not observed in the $Z \rightarrow \mu^+\mu^-$ channel in all algorithms

---

[2] Delayed (long-lifetime) decays can occur if the J/Ψ is significantly boosted, and hence subject to time dilation proportional to the boost.

at L2 except Strategy B, and completely absent at EF. This may be expected, since high$-p_T$ muons are less affected by energy loss through material interactions. Here, however, there is some dependency at high pseudorapidity, which corresponds to the pixel, SCT and TRT end-caps. As shown in Figure 3.2 in Section 3.2.1, the end-cap granularity decreases at high η; this affects high$-p_T$ muons more than low$-p_T$ as their tracks curve less, resulting in fewer detector hits.

The near hermetic coverage in the azimuthal plane results in an efficiency independent of ϕ for all algorithms except Strategy B in the $Z \rightarrow \mu^+\mu^-$ channel (Figure 6.12). It is therefore deduced that the Strategy B algorithm has some implicit geometric dependency, possibly due to its use of combinations of various detector layers (described in Section 3.3.3).

Figure 6.13 shows the efficiency as a function of the mean number of pp interactions per bunch crossing, $< \mu >$. This variable provides a handle on how the efficiency depends on the number of additional pile-up vertices, and can be compared directly between the two years. As can be seen in Figure 6.13b, IDSCAN featured a decreasing efficiency with increasing $< \mu >$ for high$-p_T$ muons. This motivated the aforementioned tightening of the cuts utilised by Strategy A, resulting in a flat efficiency for all $< \mu >$ in 2012. Therefore while this optimisation mistakenly caused a drop in efficiency for low$-p_T$ muons, it correctly increased it at high$-p_T$. A smaller dependency, relatively speaking, is seen in the $J/\Psi \rightarrow \mu^+\mu^-$ channel at L2.

The efficiency as a function of the number of offline reconstructed vertices per event is shown in Figure 6.14. This variable is similar to $< \mu >$ in that it provides a measure of the pile-up dependency; however, as there were changes in the vertexing algorithms between 2011 and 2012, a direct comparison between the two years is not possible. As may be expected, the $Z \rightarrow \mu^+\mu^-$ distributions reflect their $< \mu >$ equivalents, with a drop-off in efficiency observed for IDSCAN in 2011. A similar dependency is also observed in the $J/\Psi \rightarrow \mu^+\mu^-$ channel for IDSCAN, varying by approximately 4% as the number of vertices increases. The overall variation is smaller in Strategy A in both channels, again due to the optimisation. By comparison with Strategy B, Strategy A is more sensitive to the number of vertices as it begins its track pattern recognition by finding the vertex $z-$position. This is reflected in the flat efficiency produced by Strategy B.

In almost all distributions in both channels the Strategy C algorithm maintains a flat efficiency of $\sim 98\%$ for $J/\Psi \rightarrow \mu^+\mu^-$ and $\sim 99\%$ for $Z \rightarrow \mu^+\mu^-$. This reflects the fact that it employs the offline software pattern recognition techniques similar to the EF software. It does however display the $\eta-$dependence observed in the other algorithms.

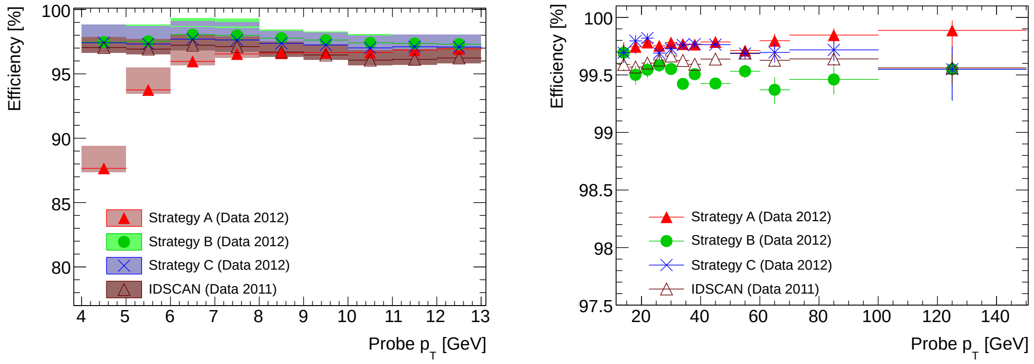

(a) $J/\Psi \rightarrow \mu^+\mu^-$, L2 **(b)** $Z \rightarrow \mu^+\mu^-$, L2

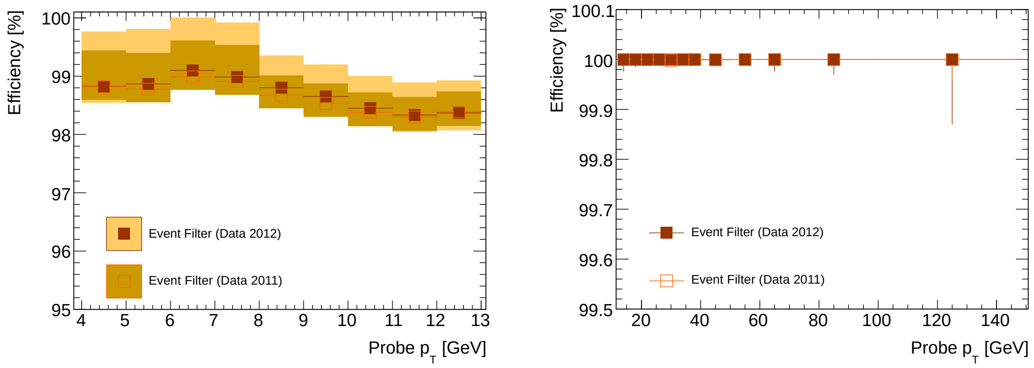

(c) $J/\Psi \rightarrow \mu^+\mu^-$, EF **(d)** $Z \rightarrow \mu^+\mu^-$, EF

Figure 6.8: The ID muon track reconstruction efficiency as a function of the probe muon p_T, in (a,c) $J/\Psi \rightarrow \mu^+\mu^-$ at L2 and EF; and (b,d) $Z \rightarrow \mu^+\mu^-$ at L2 and EF.

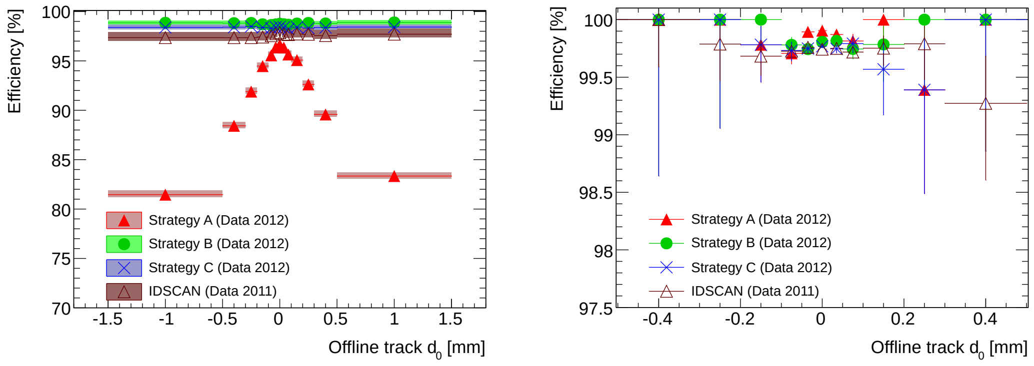

(a) $J/\Psi \rightarrow \mu^+\mu^-$, L2 **(b)** $Z \rightarrow \mu^+\mu^-$, L2

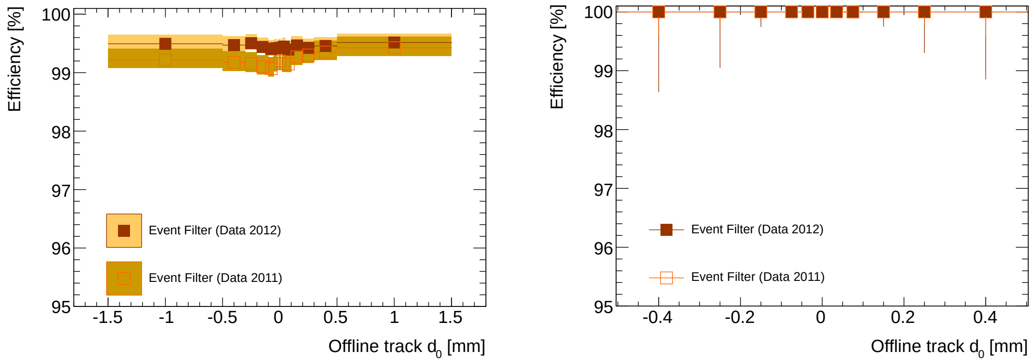

(c) $J/\Psi \rightarrow \mu^+\mu^-$, EF **(d)** $Z \rightarrow \mu^+\mu^-$, EF

Figure 6.9: The ID muon track reconstruction efficiency as a function of the offline track (matched to the probe) d_0, in (a,c) $J/\Psi \rightarrow \mu^+\mu^-$ at L2 and EF; and (b,d) $Z \rightarrow \mu^+\mu^-$ at L2 and EF.

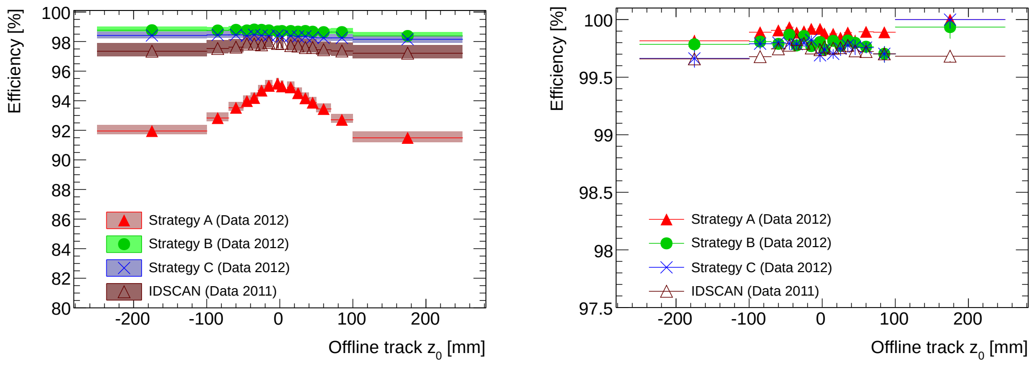

(a) $J/\Psi \rightarrow \mu^+\mu^-$, L2 **(b)** $Z \rightarrow \mu^+\mu^-$, L2

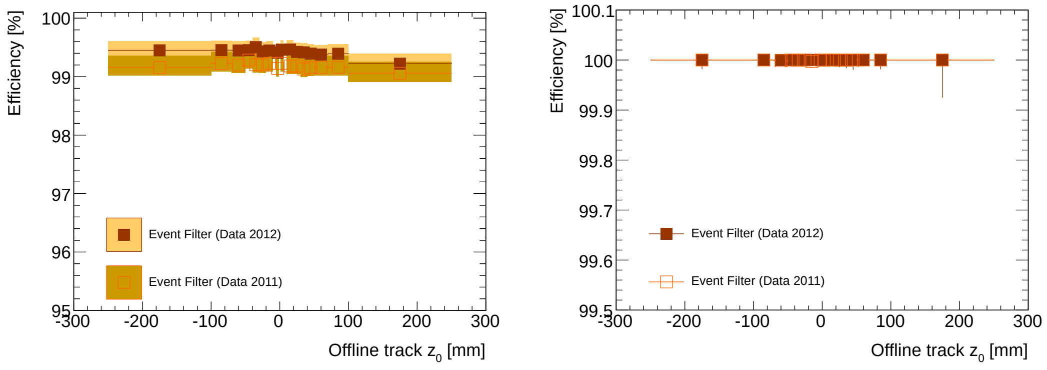

(c) $J/\Psi \rightarrow \mu^+\mu^-$, EF **(d)** $Z \rightarrow \mu^+\mu^-$, EF

Figure 6.10: The ID muon track reconstruction efficiency as a function of the offline track (matched to the probe) z_0, in (a,c) $J/\Psi \rightarrow \mu^+\mu^-$ at L2 and EF; and (b,d) $Z \rightarrow \mu^+\mu^-$ at L2 and EF.

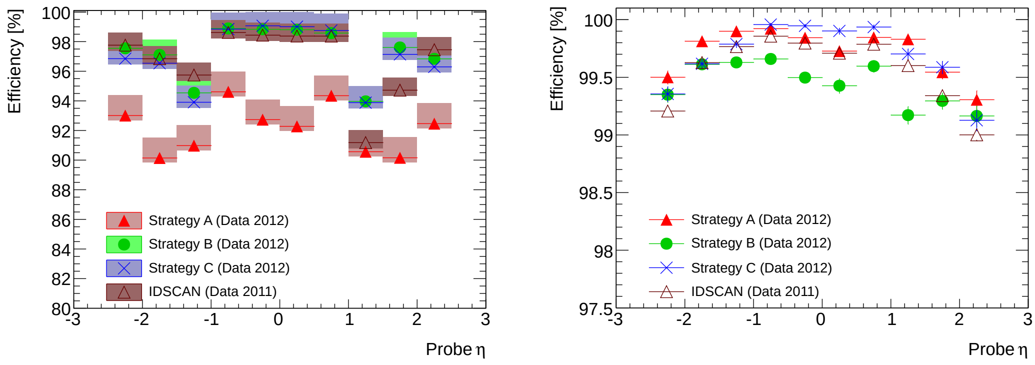

(a) $J/\Psi \rightarrow \mu^+\mu^-$, L2 **(b)** $Z \rightarrow \mu^+\mu^-$, L2

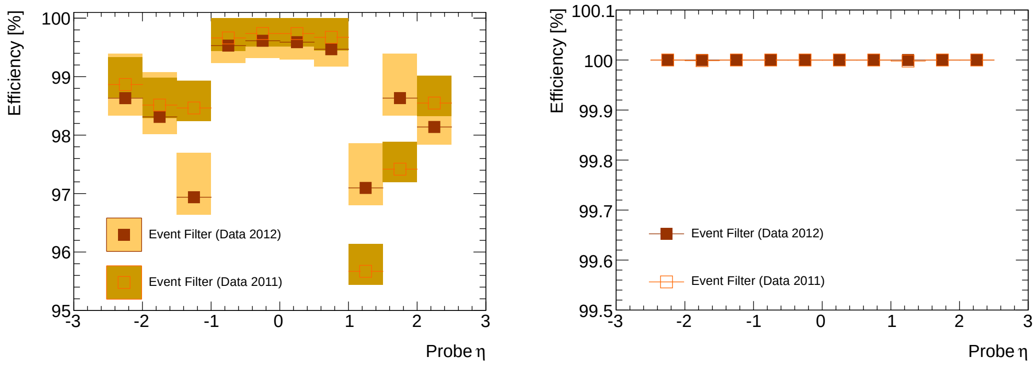

(c) $J/\Psi \rightarrow \mu^+\mu^-$, EF **(d)** $Z \rightarrow \mu^+\mu^-$, EF

Figure 6.11: The ID muon track reconstruction efficiency as a function of the probe muon η, in (a,c) $J/\Psi \rightarrow \mu^+\mu^-$ at L2 and EF; and (b,d) $Z \rightarrow \mu^+\mu^-$ at L2 and EF.

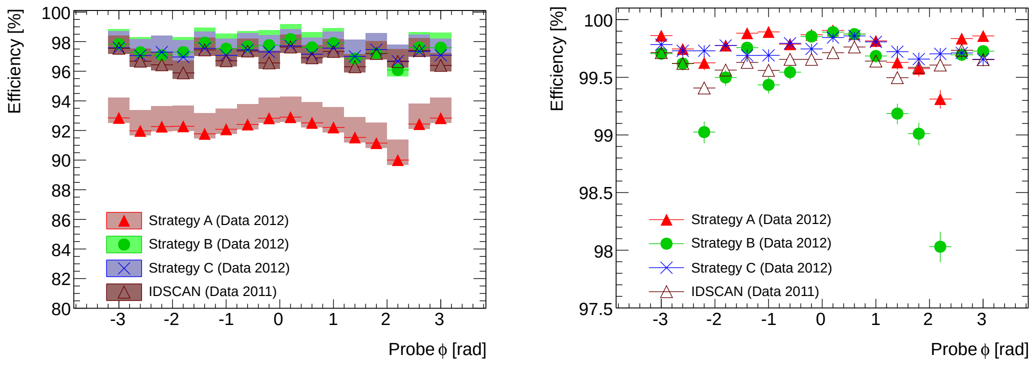

(a) $J/\Psi \to \mu^+\mu^-$, L2 **(b)** $Z \to \mu^+\mu^-$, L2

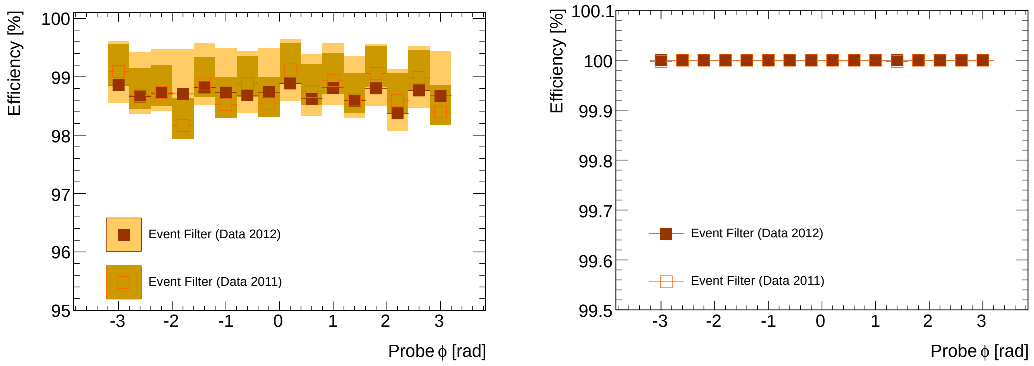

(c) $J/\Psi \to \mu^+\mu^-$, EF **(d)** $Z \to \mu^+\mu^-$, EF

Figure 6.12: The ID muon track reconstruction efficiency as a function of the probe muon ϕ, in (a,c) $J/\Psi \to \mu^+\mu^-$ at L2 and EF; and (b,d) $Z \to \mu^+\mu^-$ at L2 and EF.

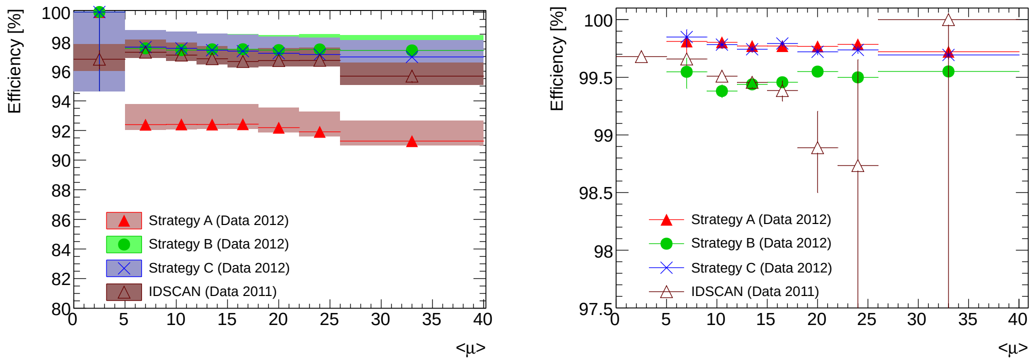

(a) $J/\Psi \rightarrow \mu^+\mu^-$, L2 **(b)** $Z \rightarrow \mu^+\mu^-$, L2

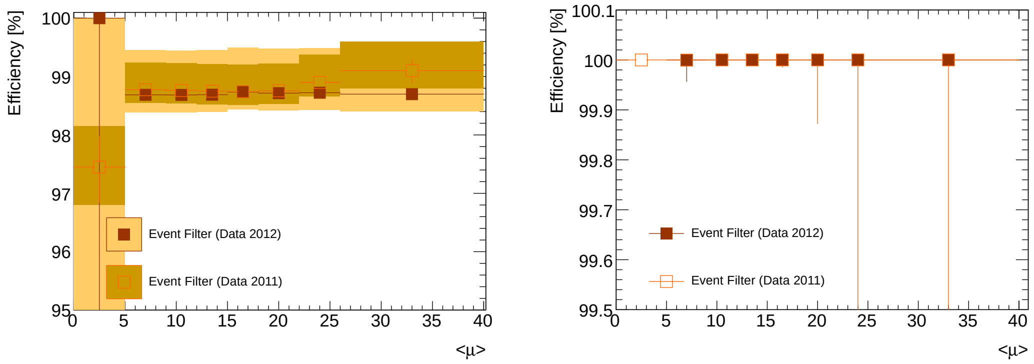

(c) $J/\Psi \rightarrow \mu^+\mu^-$, EF **(d)** $Z \rightarrow \mu^+\mu^-$, EF

Figure 6.13: The ID muon track reconstruction efficiency as a function of $< \mu >$, the mean number of pp interactions per bunch crossing, in (a,c) $J/\Psi \rightarrow \mu^+\mu^-$ at L2 and EF; and (b,d) $Z \rightarrow \mu^+\mu^-$ at L2 and EF.

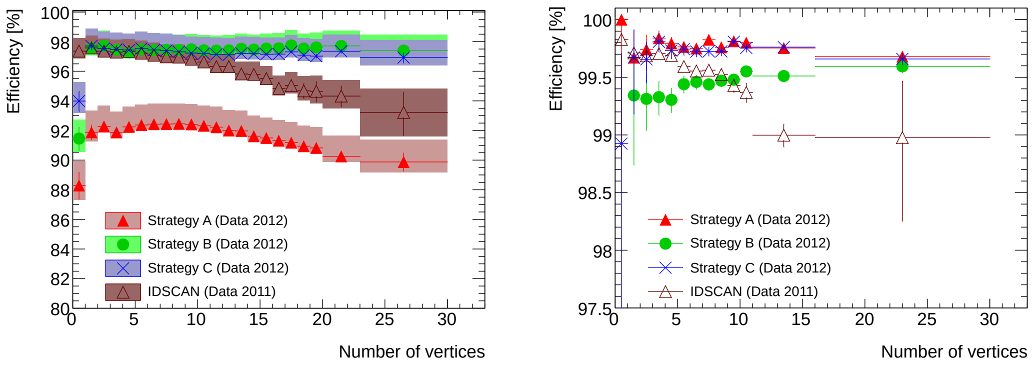

(a) $J/\Psi \to \mu^+\mu^-$, L2 **(b)** $Z \to \mu^+\mu^-$, L2

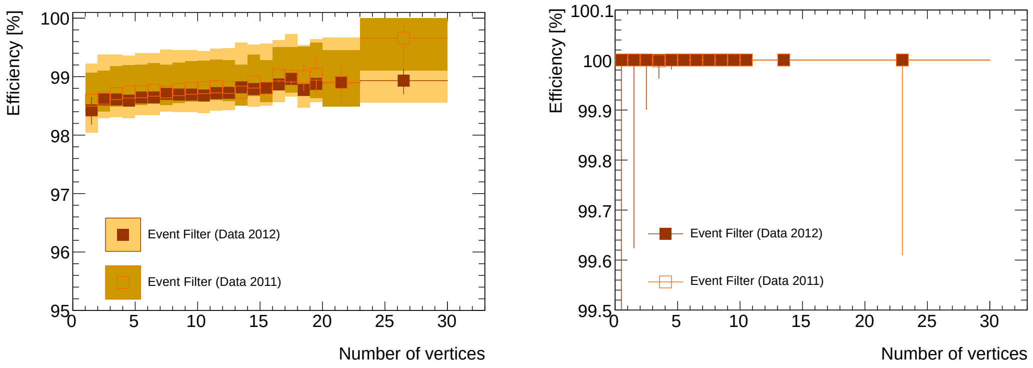

(c) $J/\Psi \to \mu^+\mu^-$, EF **(d)** $Z \to \mu^+\mu^-$, EF

Figure 6.14: The ID muon track reconstruction efficiency as a function of the number of offline reconstructed vertices per event, in (a,c) $J/\Psi \to \mu^+\mu^-$ at L2 and EF; and (b,d) $Z \to \mu^+\mu^-$ at L2 and EF.

6.2 Summary

The muon track reconstruction efficiency for the inner detector High Level Trigger algorithms has been measured using pp collision data collected by the ATLAS detector at $\sqrt{s} = 7$ TeV and $\sqrt{s} = 8$ TeV. The efficiency is calculated using the tag and probe method to select muons from $J/\Psi \to \mu^+\mu^-$ and $Z \to \mu^+\mu^-$ decays, with a given inner detector algorithm considered efficient if it provides a suitable track to form a $J/\Psi \to \mu^+\mu^-$ or $Z \to \mu^+\mu^-$ candidate with the tag muon. This yields measurements unbiased by the offline reconstruction, the first of their type with ATLAS. Furthermore, the analysis code is installed at the first stage of data reprocessing as part of an automated monitoring framework.

The average efficiencies for $J/\Psi \to \mu^+\mu^-$ candidates in 2011 ($\sqrt{s} = 7$ TeV) and 2012 data ($\sqrt{s} = 8$ TeV) are shown in Table 6.2. The uncertainties account for deviations in the efficiency as a result of background, the choice of matching cut and the statistical uncertainty.

The average efficiencies for $Z \to \mu^+\mu^-$ candidates in 2011 and 2012 data are shown in Table 6.3. The statistical and systematic uncertainties are found to be negligible ($< 0.1\%$).

$J/\Psi \to \mu^+\mu^-$	Level 2 (%)	Event Filter (%)
2011	$96.9^{+0.4}_{-0.6}$	$98.7^{+0.1}_{-0.3}$
2012	$97.5^{+0.4}_{-1.1}$	$98.8^{+0.1}_{-0.6}$

Table 6.2: Numerical values for the Level 2 and Event Filter reconstruction efficiency in 2011 and 2012 data for low$-p_T$ muons.

$Z \to \mu^+\mu^-$	Level 2 (%)	Event Filter (%)
2011	99.6	100
2012	99.7	100

Table 6.3: Numerical values for the Level 2 and Event Filter reconstruction efficiency in 2011 and 2012 data for high$-p_T$ muons.

Chapter 7

Conclusions

With the LHC having delivered its final pp collisions in February 2013, it now enters an upgrade phase with the aim of commencing collisions at $\sqrt{s} = 14$ TeV in 2015. During these first years of operation the LHC surpassed many expectations, delivering a total integrated luminosity of over 29 fb^{-1}, of which the ATLAS detector successfully recorded approximately 27 fb^{-1}. This has come at a price, however, with the number of additional interactions per pp bunch crossing steadily increasing as the LHC achieved higher luminosities, peaking at approximately 38 in 2012. The main body of this work represents a small part of the collective effort to efficiently record and accurately model the events in this environment.

To this aim, measurements of the contribution to the total transverse energy from both pile-up and the underlying event in the entirety of the ATLAS detector have been presented. The measurements were corrected for detector effects, yielding hadron-level distributions that can be directly compared with current Monte Carlo predictions. In general all Monte Carlo models and tunes under-predict the quantity of transverse energy in the forward region with respect to the central region by 20-30%. The degree of diffraction was not found to alter the central-forward ratio, and a preferred Parton Distribution Function was shown to reduce the central-forward discrepancy. These results are being used to build new Monte Carlo tunes that, for the first time, constrain the central-forward contributions from both pile-up and the underlying event. This is an essential step for any LHC analysis that is dependent upon Monte Carlo predictions of non-perturbative QCD.

In the spirit of the LHC as a discovery machine, a new technique designed to be sensitive to new physics processes has been presented. Utilising well known Standard

Model processes, it infers the presence of new particles with large $\not\!\!E_T$ and jet final states from a deviation in the ratio of branching fractions between $Z \rightarrow \nu\bar{\nu}$ and $Z \rightarrow \mu^+\mu^-$ candidates. The strength of this technique over existing methods lies in its model independent approach — it is essentially sensitive to any new particle with a high $\not\!\!E_T$ plus jet final state. Furthermore, as the measurement is defined in terms of a ratio, correlated systematic uncertainties would cancel, yielding a more accurate measurement. This is particularly important in searches for new particles, which typically have very small cross-sections.

Preliminary Monte Carlo studies indicate that the measurement is sensitive to the presence of an example dark matter candidate in a high background environment, causing a $\sim 20\%$ shift from Standard Model expectations for $\not\!\!E_T > 400$ GeV. An estimate of the correction factor necessary to bring the reconstructed Monte Carlo back to the hadron level is performed, and found to be largely dependent on the muon reconstruction efficiency. When applied to real data and with all sources of background and systematic uncertainty considered, this technique would potentially facilitate accurate measurements of physics beyond the Standard Model.

Finally, a detailed analysis of the efficiency with which the inner detector trigger algorithms reconstruct muon tracks has been presented. It utilises the tag and probe technique to select reference muons, against which an unbiased measure of the inner detector track reconstruction efficiency is obtained. In general the High Level Trigger algorithms maintain an efficiency of between 96% to 100%, depending on the reconstruction level and p_T of the reference muon. However, a drop in efficiency in the leading Level 2 algorithm at low muon p_T is observed in the 2012. This was found to be due to an optimisation of its parameters for high p_T track reconstruction. To facilitate a quick response to such issues, the software used to conduct this analysis is installed at the first stage of ATLAS data reprocessing, forming part of an automated performance monitoring framework.

Appendix A

Model dependence as a function of various cuts

"If you're going to do a job, do it properly."
— Old proverb

The extent of the model dependence in the corrections may depend on the truth particle p cuts. In order to investigate this Figure A.1 shows the data corrected back to different truth level definitions using `H++ UE7-2` and `Pythia 6 AMBT1`. Here, as opposed to the more involved unfolding technique applied to obtain final analysis results, the bin-by-bin correction method is used, which multiplies the data in each $|\eta|$ bin by the ratio of hadron to reconstructed level entries in the same bin. As we deviate from the default cuts the model dependence in the most central $|\eta|$ bins increases. For harder p cuts the `UE7-2` correction reduces with respect to the `AMBT1` correction factor; the harder the cut the more the correction procedure has to account for particles that are not in the truth definition but that do contribute to the E_T^{flow} at the cluster level. For `UE7-2` there are generally more soft particles so this effect results in an under correction as compared to `AMBT1` as the p cut is increased. For lower p cuts `UE7-2` has a larger correction for the reasons discussed above.

In order to determine whether making a minimum $|E|$ cut on the individual clusters and whether excluding both low $|E|$ clusters and low p truth particles affects the model dependence, Figure A.2 shows the data corrected back to varying truth level cuts with varying cluster $|E|$ cuts applied. Due to the large variation in particle response it is difficult to determine the best set of cuts when attempting to exclude lower energy particles. With the cuts used in this example the model dependence increases as harder cuts are made.

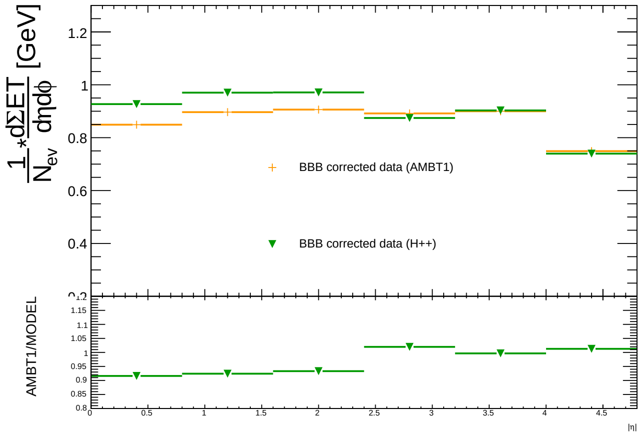

(a) $p_T^{charged} > 400$ MeV and $p_T^{neutral} > 100$ MeV

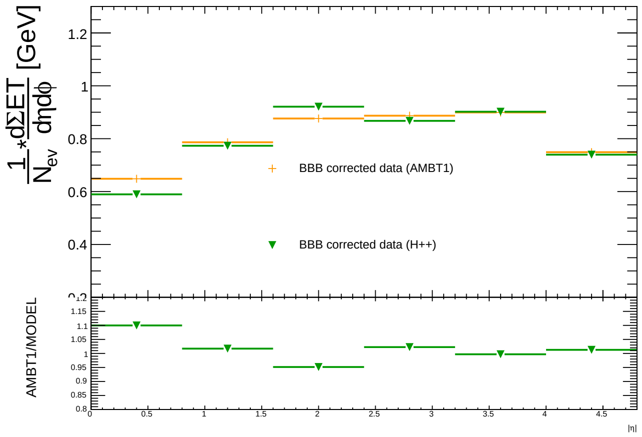

(b) $p_T^{charged} > 600$ MeV and $p_T^{neutral} > 300$ MeV

Figure A.1: EM-scale topoCluster E_T^{flow} comparisons, correcting `H++ UE7-2` using `Pythia 6 AMBT1` and vice-versa using the bin-by-bin (BBB) method, in minimum bias data for the following hadron level selection cuts: (a) charged $p > 400$ MeV; neutral $p > 100$ MeV (b) charged $p > 600$ MeV; neutral $p > 300$ MeV.

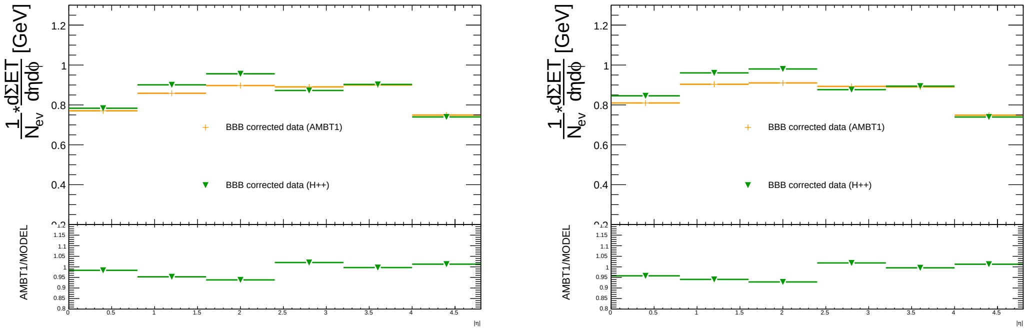

(a) $p_T^{charged} > 400$ MeV and $p_T^{neutral} > 100$ MeV

(b) $p_T^{charged} > 400$ MeV, $p_T^{neutral} > 100$ MeV, $E^{topo} > 200$ MeV

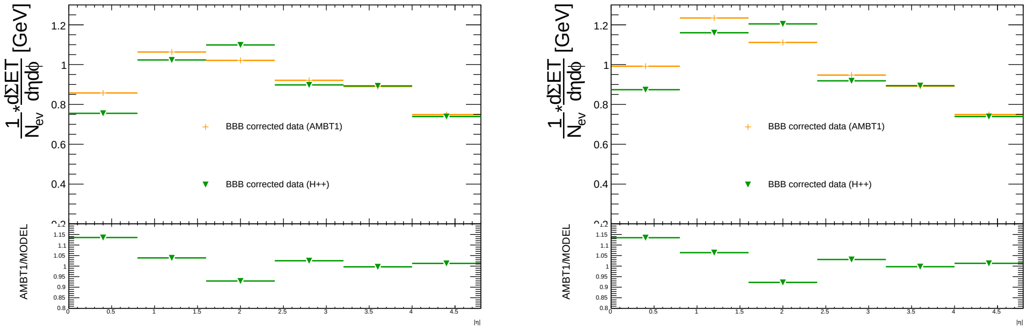

(c) $p_T^{charged} > 800$ MeV, $p_T^{neutral} > 500$ MeV, $E^{topo} > 500$ MeV

(d) $p_T^{charged} > 1$ GeV, $p_T^{neutral} > 700$ MeV, $E^{topo} > 700$ MeV

Figure A.2: EM-scale topoCluster E_T^{flow} comparisons, correcting `H++ UE7-2` using `Pythia 6 AMBT1` and vice-versa, using the bin-by-bin method (BBB), in minimum bias data for the following hadron and reconstructed level cuts: (a) charged $p > 500$ MeV; neutral $p > 200$ MeV; no topoCluster $|E|$ cut (b) charged $p > 500$ MeV; neutral $p > 200$ MeV; topoCluster $|E| > 200$ MeV (c) charged $p > 800$ MeV; neutral $p > 500$ MeV; topoCluster $|E| > 500$ MeV (d) charged $p > 1$ GeV; neutral $p > 700$ MeV; topoCluster $|E| > 700$ MeV.

Bibliography

[1] CDF Collaboration Collaboration, F. Abe et al., *Observation of top quark production in $\bar{p}p$ collisions*, Phys.Rev.Lett. **74** (1995) 2626–2631, `arXiv:hep-ex/9503002 [hep-ex]`.

[2] G. Salamanna, *Measurement of the top quark mass with the ATLAS detector*, `arXiv:1302.4472 [hep-ex]`.

[3] D0 collaboration Collaboration, O. Brandt, *Measurements of the top quark mass at D0*, `arXiv:1301.0755 [hep-ex]`.

[4] CDF Collaboration, T. Aaltonen et al., *Precision Top-Quark Mass Measurements at CDF*, Phys.Rev.Lett. **109** (2012) 152003, `arXiv:1207.6758 [hep-ex]`.

[5] G. P. Salam and G. Soyez, *A Practical Seedless Infrared-Safe Cone jet algorithm*, JHEP **0705** (2007) 086, `arXiv:0704.0292 [hep-ph]`.

[6] M. Cacciari, G. Salam, and G. Soyez, *The anti-k_t jet clustering algorithm*, JHEP **0804** (2008) 063, `arXiv:0802.1189 [hep-ph]`.

[7] A. Martin, W. Stirling, R. Thorne, and G. Watt, *Parton distributions for the LHC*, Eur.Phys.J. **C63** (2009) 189–285, `arXiv:0901.0002 [hep-ph]`.

[8] J. Pumplin, D. Stump, J. Huston, H. Lai, P. M. Nadolsky, et al., *New generation of parton distributions with uncertainties from global QCD analysis*, JHEP **0207** (2002) 012, `arXiv:hep-ph/0201195 [hep-ph]`.

[9] Ames-Bologna-CERN-Dortmund-Heidelberg-Warsaw Collaboration, A. Breakstone et al., *Charged Multiplicity Distribution in p p Interactions at ISR Energies*, Phys.Rev. **D30** (1984) 528.

[10] ATLAS Collaboration, G. Aad et al., *Rapidity gap cross sections measured with the ATLAS detector in pp collisions at $\sqrt{s} = 7$ TeV*, Eur.Phys.J. **C72** (2012) 1926, `arXiv:1201.2808 [hep-ex]`.

[11] GEANT4 Collaboration, S. Agostinelli et al., *GEANT4: A simulation toolkit*, Nucl. Instrum. Meth. **A506** (2003) 250–303.

[12] T. Sjostrand, S. Mrenna, and P. Z. Skands, *PYTHIA 6.4 Physics and Manual*, JHEP **0605** (2006) 026, `arXiv:hep-ph/0603175 [hep-ph]`.

[13] T. Sjostrand, S. Mrenna, and P. Z. Skands, *A Brief Introduction to PYTHIA 8.1*, Comput.Phys.Commun. **178** (2008) 852–867, `arXiv:0710.3820 [hep-ph]`.

[14] B. Andersson, G. Gustafson, G. Ingelman, and T. Sjostrand, *Parton Fragmentation and String Dynamics*, Phys.Rept. **97** (1983) 31–145.

[15] J. R. Forshaw and D. A. Ross, *Quantum Chromodynamics and the Pomeron*, Cambridge University Press **No. 9** (1997) 17.

[16] G. A. Schuler and T. Sjostrand, *Hadronic diffractive cross-sections and the rise of the total cross-section*, Phys.Rev. **D49** (1994) 2257–2267.

[17] H1 Collaboration, A. Aktas et al., *Measurement and QCD analysis of the diffractive deep-inelastic scattering cross-section at HERA*, Eur.Phys.J. **C48** (2006) 715–748, `arXiv:hep-ex/0606004 [hep-ex]`.

[18] B. Webber, *A QCD Model for Jet Fragmentation Including Soft Gluon Interference*, Nucl.Phys. **B238** (1984) 492.

[19] H. Drescher, M. Hladik, S. Ostapchenko, T. Pierog, and K. Werner, *Parton based Gribov-Regge theory*, Phys.Rept. **350** (2001) 93–289, `arXiv:hep-ph/0007198 [hep-ph]`.

[20] M. L. Mangano, M. Moretti, F. Piccinini, R. Pittau, and A. D. Polosa, *ALPGEN, a generator for hard multiparton processes in hadronic collisions*, JHEP **0307** (2003) 001, `arXiv:hep-ph/0206293 [hep-ph]`.

[21] ATLAS Collaboration, G. Aad et al., *The ATLAS Experiment at the CERN Large Hadron Collider*, JINST **3** (2008) S08003.

[22] ATLAS Collaboration, W. Armstrong et al., *ATLAS: Technical proposal for a general-purpose p p experiment at the Large Hadron Collider at CERN*, .

[23] N. Konstantinidis, M. Sutton, J. Baines, D. Emelyanov, F. Parodi, et al., *A fast tracking algorithm for the ATLAS level 2 trigger*, Nucl.Instrum.Meth. **A566** (2006) 166–169.

[24] CDF Collaboration, T. Aaltonen et al., *Measurement of Particle Production and Inclusive Differential Cross Sections in $p\bar{p}$ Collisions at $\sqrt{s}$ =1.96 TeV*, Phys. Rev. D **79** (2009) 112005, `arXiv:0904.1098 [hep-ex]`. [*Erratum ibid* **82** (2010) 119903].

[25] ALICE Collaboration, K. Aamodt et al., *Charged-particle multiplicity measured in proton-proton collisions at $\sqrt{s}$ = 7 TeV with ALICE at LHC*, Eur. Phys. J. C **68** (2010) 345, `arXiv:0911.5430`.

[26] CMS Collaboration, *Charged particle multiplicities in pp interactions at $\sqrt{s}$ =0.9, 2.36 and 7 TeV*, JHEP **01** (2011) 079, `arXiv:1011.5531`.

[27] ATLAS Collaboration, *Charged-particle multiplicities in pp interactions measured with the ATLAS detector at the LHC*, New J. Phys. **13** (2010) 053033, `arXiv:1012.5104`.

[28] CDF Collaboration, D. Acosta et al., *The Underlying event in hard interactions at the Tevatron anti-p p collider*, Phys. Rev. D **70** (2004) 072002, `arXiv:hep-ex/0404004`.

[29] CDF Collaboration, T. Aaltonen et al., *Studying the Underlying Event in Drell-Yan and High Transverse Momentum Jet Production at the Tevatron*, Phys. Rev. D **82** (2010) 034001, `arXiv:1003.3146`.

[30] ATLAS Collaboration, *Measurement of underlying event characteristics using charged particles in pp collisions at $\sqrt{s} = 900$ GeV and 7 TeV with the ATLAS detector*, Phys. Rev. D **83** (2011) 112001, `arXiv:1012.0791`.

[31] ALICE Collaboration, B. Abelev et al., *Underlying Event measurements in pp collisions at $\sqrt{s}$ = 0.9 and 7 TeV with the ALICE experiment at the LHC*, JHEP **1207** (2012) 116, `arXiv:1112.2082 [hep-ex]`.

[32] CMS Collaboration, *Measurement of the underlying event activity at the LHC with $\sqrt{s}$ =7 TeV and comparison with $\sqrt{s}$ =0.9 TeV*, JHEP **09** (2011) 109, `arXiv:1107.0330`.

[33] ATLAS Collaboration, *Measurements of underlying-event properties using neutral and charged particles in pp collisions at $\sqrt{s}$ = 900 GeV and $\sqrt{s}$ = 7 TeV with the ATLAS detector at the LHC*, Eur. Phys. J. C **71** (2011) 1636, `arXiv:1103.1816`.

[34] CMS Collaboration, *Measurement of energy flow at large pseudorapidities in pp collisions at $\sqrt{s}$ =0.9 and 7 TeV*, JHEP **11** (2011) 148, `arXiv:1110.0211`.

[35] ATLAS Collaboration Collaboration, G. Aad et al., *Improved luminosity determination in pp collisions at sqrt(s) = 7 TeV using the ATLAS detector at the LHC*, `arXiv:1302.4393 [hep-ex]`.

[36] R. Field, *Min-Bias and the Underlying Event at the LHC*, Acta Phys.Polon. **B42** (2011) 2631–2656, `arXiv:1110.5530 [hep-ph]`.

[37] R. Brune and F. Rademakers, *ROOT — an object orientated data analysis framework*, Nucl. Inst. Meth. in Phys. Res. **A389** (1997) 81–86.

[38] W. Lampl, S. Laplace, D. Lelas, P. Loch, H. Ma, et al., *Calorimeter clustering algorithms: Description and performance*, ATL-LARG-PUB-2008-002 (2008) . `http://inspirehep.net/record/807147`.

[39] E. Abat et al., *Study of the response of the ATLAS central calorimeter to pions of energies from 3 to 9 GeV*, Nucl. Instrum. Meth. A **607** (2009) 372.

[40] P. Adragna et al., *Testbeam studies of production modules of the ATLAS tile calorimeter*, Nucl. Instrum. Meth. A **606** (2009) 362.

[41] M. Aharrouche et al., *Measurement of the response of the ATLAS liquid argon barrel calorimeter to electrons at the 2004 combined test-beam*, Nucl. Instrum. Meth. A **614** (2010) 400.

[42] J. Archambault et al., *Energy calibration of the ATLAS liquid argon forward calorimeter*, JINST **3** (2008) P02002.

[43] ATLAS Collaboration, G. Aad et al., *Measurements of the pseudorapidity dependence of the total transverse energy in proton-proton collisions at $\sqrt{s} = 7$ TeV with ATLAS*, JHEP **1211** (2012) 033, `arXiv:1208.6256 [hep-ex]`.

[44] A. Hocker and V. Kartvelishvili, *SVD approach to data unfolding*, Nucl.Instrum.Meth. **A372** (1996) 469–481, `arXiv:hep-ph/9509307 [hep-ph]`.

[45] B. Malaescu, *An Iterative, Dynamically Stabilized(IDS) Method of Data Unfolding*, `arXiv:1106.3107 [physics.data-an]`.

[46] J. W. Monk and C. Oropeza-Barrera, *The HBOM Method for Unfolding Detector Effects*, Nucl.Instrum.Meth. **A701** (2013) 17–24, `arXiv:1111.4896 [hep-ex]`.

[47] G. D'Agostini, *A Multidimensional unfolding method based on Bayes theorem*, Nucl. Instrum. Meth. A **362** (1995) 487.

[48] B. Wynne, *Imagiro: An Implementation of Bayesian iterative unfolding for high energy physics*, `arXiv:1203.4981 [physics.data-an]`.

[49] ATLAS Collaboration, *Charged particle multiplicities in p p interactions at $\sqrt{s}$ = 0.9 and 7 TeV in a diffractive limited phase-space measured with the ATLAS detector at the LHC and new PYTHIA6 tune*, .

[50] ATLAS Collaboration, *Single hadron response measurement and calorimeter jet energy scale uncertainty with the ATLAS detector at the LHC*, `arXiv:1203.1302 [hep-ex]`.

[51] J. Pinfold et al., *Evaluation of the Local Hadronic Calibration with Combined Beam-Test Data for the Endcap and Forward Calorimeters of ATLAS in the Pseudorapidity Region* $2.5 < |\eta| < 4.0$, Nucl. Instrum. Meth. A **693** (2012) 74.

[52] ATLAS Collaboration, G. Aad et al., *Electron performance measurements with the ATLAS detector using the 2010 LHC proton-proton collision data*, Eur.Phys.J. **C72** (2012) 1909, `arXiv:1110.3174 [hep-ex]`.

[53] ATLAS Collaboration, G. Aad et al., *Jet energy measurement with the ATLAS detector in proton-proton collisions at $\sqrt{s} = 7$ TeV*, `arXiv:1112.6426 [hep-ex]`.

[54] ATLAS Collaboration, *Measurement of dijet production with a jet veto in pp collisions at sqrt(s) = 7 TeV using the ATLAS detector*, `arXiv:1112.6426v1 [hep-ex]`.

[55] *The Durham HepData Project*, IPPP (2013) . `http://hepdata.cedar.ac.uk/pdf/pdf3.html`.

[56] ATLAS Collaboration, *New ATLAS event generator tunes to 2010 data*, ATL-PHYS-PUB-2011-00 (2011) . `http://inspirehep.net/record/1196773`.

[57] G. Lykasov et al., *Forward heavy flavour production in p-p collisions at LHC and intrinsic quark components in proton*, EPL **99** (2012) , `arXiv:1205.1131v2 [hep-ph]`.

[58] Particle Data Group Collaboration, J. Beringer et al., *The Review of Particle Physics*, Phys. Rev. **D86** (2012) .

[59] OPAL Collaboration, M. Akrawy et al., *Measurement of the Z^0 Mass and Width with the OPAL Detector at LEP*, Phys.Lett. **B231** (1989) 530.

[60] J. M. Campbell et al., *Hard interactions for quarks and gluons: a primer for LHC physics*, Reports on Progress in Physics **70:89** (2007) , `arXiv:0611148 [hep-ph]`.

[61] ATLAS Collaboration Collaboration, G. Aad et al., *Search for new phenomena with the monojet and missing transverse momentum signature using the ATLAS detector in* $\sqrt{s} = 7$ *TeV proton-proton collisions*, Phys.Lett. **B705** (2011) 294–312, `arXiv:1106.5327 [hep-ex]`.

[62] ATLAS Collaboration, *Performance of the ATLAS transverse energy triggers with initial LHC runs at* $\sqrt{s} = 7$ *TeV*, ATLAS-CONF-2011-072 (2011) . `http://inspirehep.net/record/1204110`.

[63] J. Alwall, P. Demin, S. de Visscher, R. Frederix, M. Herquet, et al., *MadGraph/MadEvent v4: The New Web Generation*, JHEP **0709** (2007) 028, `arXiv:0706.2334 [hep-ph]`.

[64] ATLAS Collaboration, *Muon reconstruction efficiency in reprocessed 2010 LHC proton-proton collision data recorded with the ATLAS detector*, . `http://inspirehep.net/record/1204119`.

[65] ATLAS Collaboration, *Performance of the ATLAS Inner Detector Track and Vertex Reconstruction in the High Pile-Up LHC Environment*, ATLAS-CONF-2012-042 (2012) . `http://inspirehep.net/record/1204277`.

[66] ATLAS Collaboration, J. Masik, *Performance of the ATLAS Inner Detector Trigger algorithms in pp collisions at 7TeV*, ATL-DAQ-PROC-2011-025 (2011) . `http://inspirehep.net/record/1196822`.

[67] ATLAS Collaboration, *Muon Reconstruction Performance*, ATLAS-CONF-2010-064 (2010) . `http://inspirehep.net/record/1204024`.